TECHNISCHE UNIVERSITÄT MÜNCHEN

Max-Planck-Institut für Biochemie
Abteilung Molekulare Strukturbiologie

Automated three-dimensional electron microscopy data acquisition for high-throughput applications of frozen hydrated biological samples

Andreas W. Korinek, M.Sc.

Vollständiger Abdruck der von der Fakultät für Chemie
der Technischen Universität München
zur Erlangung des akademischen Grades eines

Doktors der Naturwissenschaften (Dr. rer. nat.)

genehmigten Dissertation.

Vorsitzender:	Univ.-Prof. Dr. Michael Sattler
Prüfer der Dissertation:	
	1. Hon.-Prof. Dr. Wolfgang Baumeister
	2. Univ.-Prof. Dr. Sevil Weinkauf

Die Dissertation wurde am 28.4.2010 bei der Technischen Universität München
eingereicht und durch die Fakultät für Chemie am 14.6.2010 angenommen.

A common mistake people make when trying to design something completely foolproof is to underestimate the ingenuity of complete fools.

Douglas Adams (1952 – 2001), “Mostly Harmless”

Parts of this work have been published in the following articles:

TOM^2 acquisition – A versatile acquisition software designed for automated high-throughput EM applications. A. Korinek, F. Beck, G. Pfeifer, S. Nickell, W. Baumeister, J. M. Plitzko. *J Struct Biol.* submitted.

Insights into the molecular architecture of the 26S proteasome. S. Nickell, F. Beck, S. H. Scheres, A. Korinek, F. Förster, K. Lasker, O. Mihalache, N. Sun, I. Nagy, A. Sali, J. M. Plitzko, J. M. Carazo, M. Mann, W. Baumeister. *Proc Natl Acad Sci U S A.* **2009**;106(29):11943-7.

Automated cryoelectron microscopy of "single particles" applied to the 26S proteasome. S. Nickell, F. Beck, A. Korinek, O. Mihalache, W. Baumeister, J. M. Plitzko. *FEBS Lett.* **2007**;581(15):2751-6.

Structural analysis of the 26S proteasome by cryoelectron tomography. S. Nickell, O. Mihalache, F. Beck, R. Hegerl, A. Korinek, W. Baumeister. *Biochem Biophys Res Commun.* **2007**;353(1):115-20.

Contents

1 Introduction **11**

1.1 Sample Preparation 12
1.2 Resolution-Limiting Factors 14
1.3 Cellular Biology 16
1.4 Visual Proteomics 17
1.5 Single-Particle Approaches 18
1.6 Instrumental Advances towards Automation 20
1.7 Software Developments for Automated Acquisition 22
1.8 Aims of this Work 23

2 Materials & Methods **25**

2.1 The Electron Microscope: Parts and Function 25
2.1.1 Magnification 27
2.1.2 Illumination Control 27
2.1.3 Stage 30
2.1.4 Image Beam Shift 30
2.1.5 Focus 32
2.1.6 Objective Lens Rotation Center 34
2.1.7 Lens Astigmatism 34
2.1.8 Energy Filtering 35
2.2 Software Architecture 36
2.2.1 Fundamental Design of the TOM^2 Software 36
2.2.2 Design of the Hardware Abstraction Layer 37
2.3 Algorithms for Performing Microscope Adjustments 41
2.3.1 Detector Corrections 41
2.3.2 Measuring Shifts Between Images 45
2.3.3 Coordinate System Transformation 49
2.3.4 Beam Size Calibration 52
2.3.5 Automated Beam Centering 54

2.3.6 Automated Alignment of Objective Lens Rotation Center 55
2.3.7 Auto Focusing 56
2.3.8 Auto Eucentric Height 60
2.3.9 Auto Stigmation 60
2.3.10 Energy Filter Tuning 61
2.3.11 Electron Dose Calculation 64
2.4 Construction of a Specimen Map 65
2.5 Organization of the Acquisition Scheme 67
2.6 Acquisition Schemes 70
2.6.1 Single-Particle Acquisition 70
2.6.2 Tomography 74
2.6.3 Batch Tomography 77
2.6.4 Correlative Microscopy 78

3 Results & Discussion **81**
3.1 Benchmark of the Titan Krios Prototype 81
3.1.1 Auto Focusing Accuracy 83
3.1.2 Stage Drift 87
3.1.3 Contamination Buildup Rate 88
3.1.4 Data Acquisition 89
3.2 Use Cases for the TOM^2 Software 94
3.2.1 Single-Particle Acquisition of Tripeptidyl Peptidase II 94
3.2.2 Tomography of *Spiroplasma citri* 98
3.2.3 Batch Tomography of *Escherichia coli* Mini Cells 104
3.2.4 Batch Tomography of *Eisenia foetida* Sperm Cells 107

4 Conclusions and Outlook **111**

5 Acknowledgments **115**

6 Abbreviations **117**

List of Figures

2.1.1 Optical path of an electron microscope. 26
2.1.2 Defocus variations caused by non-parallel illumination. 29
2.1.3 Magnification variations caused by non-parallel illumination. 29
2.1.4 The image beam shift system 31
2.1.5 CTF at different defocus values. 33
2.2.1 Software layer organization. 38
2.2.2 Hierarchy of hardware driver classes. 40
2.3.1 Dark and gain correction of a micrograph without a sample. 43
2.3.2 Dark and gain references of Eagle 4k CCD camera. 44
2.3.3 Example of key point detection using the SIFT algorithm. 47
2.3.4 Stage coordinate system to CCD coordinate system calibration. 50
2.3.5 Beam shift coordinate system to CCD coordinate system calibration. . 51
2.3.6 Beam Size versus intensity plot. 53
2.3.7 Automated beam detection. 54
2.3.8 Flow diagram of beam centering algorithm. 55
2.3.9 Auto-focusing calibration routine. 58
2.3.10 Flow diagram of the auto-focusing algorithm. 59
2.3.11 Centering of energy-selective aperture position. 63
2.4.1 GUI for generating a map of a EM grid. 66
2.5.1 Illustration of hierarchical acquisition scheme. 68
2.6.1 State group for single-particle acquisition. 72
2.6.2 Selection of specimen areas suitable for single-particle acquisition. . . . 73
2.6.3 State group for tomography. 75
2.6.4 Measurement of tracking error depending on distance from tracking. . 76
2.6.5 Placement of sample positions for batch tomography. 77

3.1.1 3-D model of 26S proteasome. 82
3.1.2 Auto focusing accuracy. 86
3.1.3 Comparison of stage drift. 87

3.1.4 Comparison of contamination rates. 89
3.1.5 Using the tracking algorithm algorithm to center QuantiFoil holes. . . 91
3.1.6 FSC of the final 20S proteasome model. 92
3.1.7 Isosurface representation of the 20S proteasome. 93
3.2.1 Example micrograph showing TPPII complexes. 95
3.2.2 FSC of the final TPPII model. 97
3.2.3 3-D reconstruction of the TPPII complex. 97
3.2.4 Overview of two tomography positions for *S. citri*. 100
3.2.5 Overview of two tomography positions for *S. citri*. 101
3.2.6 Stage Tracking during a tilt series. 102
3.2.7 Distribution of ribosomes in *S. citri* cell. 103
3.2.8 Gallery of *E. coli* mini cell tomogram. 106
3.2.9 Overview of a *E. foetida* sperm cell. 107
3.2.10 Tomograms of a *E. foetida* sperm cell. 109

List of Tables

2.6.1 Single-particle acquisition speed at different electron microscopes 74

3.1.1 Refinement parameters of the 20S proteasome data set 92
3.2.1 Refinement parameters of the TPPII data set 96

Abstract

Three-dimensional cryo-electron microscopy in life sciences has become a powerful tool for structural studies. However, structural investigations of frozen hydrated samples require the acquisition of numerous micrographs under strict low-dose conditions. Acquisition of a tilt series for cellular tomography typically requires 50 to 200 images, recorded in a highly systematic manner. "Single-particle" analysis, a powerful tool to determine the three-dimensional structure of large macromolecular complexes such as the 26S proteasome, is even more challenging [Nickell *et al.*, 2009]. Usually, acquisition of thousands of high-quality micrographs is necessary to yield in the end a three-dimensional high-resolution structure.

Recording of large amounts of high-quality data with the transmission electron microscope in a solely manual fashion is sometimes impossible, demanding, and definitely only possible with a highly trained expert. During acquisition one has to screen and assess the specimen at different positions. To keep the optical and imaging conditions constant for each sample position a number of preliminary steps such as focusing, beam centering or adjusting the z-height of the stage have to be carried out. These tasks are best performed with the help of automated procedures, especially if one aims for better statistics and high-throughput applications. The ultimate goal is the continuous recording of large data sets within days or even weeks on "low-maintenance" microscope systems such as the Tecnai Polara G2 or the Titan Krios (FEI Company, Eindhoven, The Netherlands).

TOM^2 is a software package that provides an interface between the human operator and the electron microscope. Complex workflows are translated into microscope operations and designated tasks (see above) are executed in a methodical and completely unsupervised fashion. Based on the ideas of the original TOM toolbox [Nickell *et al.*, 2005], the software uses object-oriented programming techniques implemented in MATLAB (The MathWorks, Natick, USA). Real-world objects such as the microscope and its accessories (e.g., camera, energy filter, etc.), micrographs and parts of the acquisition scheme are designed as self-sufficient modules (objects). Each object consists of properties and methods making it an independent "machine" that can interact with other objects. The whole programming can be seen as a collection of objects with defined

relationships acting in a highly concerted fashion. The separation between the graphical user interface (GUI) and the underlying microscope-dependent control functions allows a fairly easy adaption of the software to new or different microscope systems. Currently TOM^2 supports Tecnai and Titan series microscopes equipped with different types of CCD cameras, e.g., TVIPS, Gatan and FEI Eagle.

The novel acquisition approach of TOM^2 subdivides the acquisition into a set of different hierarchical tasks. Instead of a predetermined acquisition scheme, TOM^2 allows the user to design his own acquisition protocol by providing simple tools and intuitive GUIs to build up and execute new experiments with the electron microscope. These protocols can be shared and reused by all scientists collaborating on a project, ensuring consistent imaging parameters for all recorded data.

In this work, the new concept of the TOM^2 software package was designed and implemented and its versatility is illustrated based on examples from single-particle investigations and tomography.

1 Introduction

Transmission electron microscopy can be applied to various scientific problems in different fields of science. It is utilized, e.g., in quality control during semiconductor production and as a quantitative imaging tool in material science [Zhang, 1998]. In medicine and pathology, the transmission electron microscope (TEM) is routinely used for virus detection and their identification [Goldsmith and Miller, 2009]. TEM in life-science research comprises three different fields: electron crystallography of membrane proteins, cellular tomography, and structural investigations of macromolecular complexes using single particle techniques.

The electron microscope is based on the same principles as the light microscope. However, the light microscope is limited by diffraction as described by Abbe's law of resolution. For a periodic structure the diffraction limited resolution d is

$$d = 0.5\frac{\lambda}{\mathrm{NA}}, \tag{1.0.1}$$

where λ is the wavelength of monochromatic light, or shortest of mixed wavelengths, and NA is the limiting numerical aperture of the objective or condenser lens. For visible light ($\lambda = 400\,\mathrm{nm}$) the resolution limit of an optical microscope is approximately 200 nm. High energy ($E = 300\,\mathrm{keV}$) electrons have a much smaller wavelength ($\lambda = 1.97\,\mathrm{pm}$), and thus the theoretical resolution limit of a TEM is in the sub-angstrom range and only limited by the electron optical lens aberrations.

Samples are prepared on small metal discs (3 mm diameter, and typically made out of copper or gold with a thin supporting layer of amorphous carbon) called "specimen grids" or EM grids which can be transferred to the holder and stage in the microscope column.

However, using electrons instead of photons introduces different instrumental challenges. Electrons are scattered or absorbed by air molecules, so the optical path of an electron microscope needs to be evacuated. Biological samples consist of 70 % to 80 % liquid water, and thus introducing these samples into a high vacuum will induce immediate evaporation of the liquid due to its vapor pressure. To image biological samples in a TEM the water in the sample has to be either removed, substituted or solidified. Ad-

hering to these three principles three methods of sample preparation exist: heavy-metal staining, plastic embedding, and vitrification.

1.1 Sample Preparation

The first method uses heavy metal salts such as osmium tetroxide, ammonium molybdate, or uranium acetate to negatively stain the sample on the grid [Palade, 1952]. The stain will cover all areas with no sample with a thin salt layer. After drying the specimen, excess stain is washed away leaving unstained areas as "footprints" of the protein complexes on the grid. The negative staining method is often used to prepare samples of purified and isolated macromolecular protein complexes ("single particles"). However, its main disadvantage is the introduction of staining artifacts: The resolution is limited by the stain's grain size ($\approx 2\,\mathrm{nm}$), and furthermore the protein complexes are exposed to non-native conditions during staining, which leads to flattening and deformations of their 3-D structure.

The second method replaces the solvent in the sample with a resin that has a much higher vapor pressure than solvent [Richardson *et al.*, 1960]. This technique is often used to prepare thin cellular sections. The resulting plastic sections are very durable and can be imaged at room temperature over long periods of time. However, during exposure with increasing electron dose, the resin tends to shrink, distorting the overall cellular structure and thus introducing artifacts. Therefore, samples have to be pre-irradiated and afterwards can be used continuously; however the deformation and structural alterations will remain.

The third method preserves the sample in its native solvent by rapid freezing in liquid ethane [Dubochet *et al.*, 1988]. Rapid freezing turns the liquid water into low-density amorphous ice that is comparable to glass. While preserving the native structures, the resulting frozen-hydrated specimen will exhibit a very low contrast in the micrographs because the elastic scattering cross-sections of proteins and amorphous ice are very similar. Additionally, the specimen is extremely sensitive to electron radiation allowing only minimal electron doses during acquisition to minimize radiation damage. Moreover, the sample has to be kept at liquid nitrogen temperature at all times during transfer, handling and imaging requires specialized equipment to manipulate and investigate the specimen.

Another important parameter to take into consideration during specimen preparation is the thickness of the sample. The TEM imaging process generates a two-dimensional projection of a three-dimensional specimen. In the resulting micrograph all features at the same lateral position are superimposed making it difficult to distinguish them. There

are only two possibilities to bypass this problem: either one reduces the specimen thickness or one applies tomographic methods. To disentangle the three-dimensional structure of the specimen, typically, tomographic methods are used which image the specimen under different tilt angles. A three-dimensional volume can then be reconstructed *in silico* assigning each sample feature a certain z height. In any case, even with an acceleration voltage of 300 kV, the specimen thickness should not exceed 500 nm since the projected thickness during tilting will increase considerably, and since inelastic and multiple scattering events will increase with specimen thickness, further reducing the signal-to-noise ratio (SNR) of the micrographs.

Sample thickness is a limitation because of the interaction of the electrons with the specimen. When electrons pass through the sample, they interact with sample atoms by being either scattered elastically or inelastically. Elastic scattering is wanted, since it is the main contrast forming mechanism, in an electron micrograph. The elastically scattered electrons will exhibit a weak phase shift but have the same energy as unscattered electrons and are being collected on the detector to form the image. However, deposition of energy in the sample material leads to ionization and thus to radiation damage of the sample [Glaeser and Hobbs, 1975; Glaeser and Taylor, 1978; Glaeser and Downing, 1992]. Ionization is a result of inelastically scattered electrons, which lose energy during their interaction with sample atoms. Inelastically scattered electrons and multiply scattered electrons have lower energy and are undesirable for image formation since they are out of "focus" and contribute to a chromatic "blur" in an electron micrograph. However, they can be filtered out after interaction with the sample using an energy filter (see section 2.1.8).

The mean free path of the elastically scattered electrons depends on the acceleration voltage and the material of the sample and is typically in the range of 100 to 1000 nm. Higher accelerating voltages lead to an increase of the mean free path and thus allow investigations of ever thicker samples. The acceleration voltage should hence be adjusted so that the electrons are being scattered not more than once when passing through the specimen. The likelihood of an interaction between an electron and the atoms in the sample can be expressed through the scattering cross-section. The cross-section is dependent on the acceleration voltage, overly high acceleration voltages cause a small scattering cross-section and thus will result in not enough image contrast. On the other end, overly low acceleration voltages cause excessive inelastic interaction of the beam with the sample and thus will prematurely damage the sample. Acceleration voltages in the range of 200 kV to 300 kV present a good compromise and are typically used.

The actual thickness of a frozen-hydrated specimen depends on the dimensions of the objects constituting the sample material and on the blotting time (removal of ex-

cess liquid) during specimen preparation. Plunge-frozen specimens of purified protein complexes, for example, are sufficiently thin (usually 100 nm to 200 nm) and can be imaged for single-particle analysis without additional thinning. Plunge-frozen specimens of prokaryotic cells have usually a thickness of less than 1 µm and can be imaged in a tilt series acquisition directly. Frozen-hydrated samples of eukaryotic cells are much thicker and need to be thinned down prior to imaging, which can be done either by mechanical sectioning or by other micro-machining methods [Rigort *et al.*, 2010].

To preserve the structure of living cells, the formation of ice crystals during freezing has to be avoided, since they could potentially damage the sample. Therefore, freezing has to occur rapidly at a rate of 10^4 to 10^5 $^\circ\mathrm{C\,s^{-1}}$ [Bozzola and Russell, 1999]. The freezing rate decreases rapidly with increasing specimen thickness. Therefore, samples with a thickness of less than approximately 10 µm are suitable for plunge freezing, while samples with a thickness of up to 200 µm need to be vitrified using high-pressure freezing techniques [Studer *et al.*, 1989]. Thinning of the specimen is afterwards performed by mechanical cryo-sectioning using a cryo-ultramicrotome [Gruska *et al.*, 2008] or by thinning a small area of the specimen by focused ion beam milling [Rigort *et al.*, 2010].

1.2 Resolution-Limiting Factors

As already stated, the theoretical resolution limit of a TEM at 300 kV is less than 1 Å. This limit however is only derived from the wavelength of the electrons and does not take into account other resolution-limiting factors. These additional factors will be discussed here.

The resolution of the final image is mainly dependent on the microscope's imaging system and the detecting device which records the image. The resolving power of the microscope optics is limited by the spatial and temporal coherence of the beam (mainly defined by the properties of the electron gun, see section 2.1) and the amount of aberrations being introduced to the beam while it passes through the lenses. These optical influences are described by the contrast transfer function (CTF) and an envelope function that describes the dampening of high frequency information. The effect of the CTF to an electron micrograph is explained in detail in section 2.1.5.

The detector plays an important role in acquiring high-resolution micrographs. The resolution of the detector is dependent on its sensitivity and spatial frequency response. Additionally, the SNR of the recorded micrographs influences the resolution [Rose, 1948]. The SNR is defined as the ratio of a signal power to the noise power corrupting the signal. A ratio higher than 1 indicates more signal than noise. A typical micrograph recorded for single-particle investigations has a SNR of approximately 0.05 to 0.1 [Baxter *et al.*,

2009], while a projection recorded during a tilt series has an even lower SNR because the applied dose is considerably lower (see section 1.3). The noise in a micrograph is mainly generated in the detector and consists of an additive part that is independent of illumination and a multiplicative part that is proportional to the exposure time of the detecting device (either photographic film or digital cameras). The SNR can be increased by adding more signal and thus more electrons to a micrograph. However, with increasing electron dose, the likelihood of specimen damage increases which in turn decreases the resolution and makes image analysis meaningless [Glaeser and Hobbs, 1975; Isaacson *et al.*, 1977; Glaeser and Taylor, 1978; Chiu *et al.*, 1986; Chiu, 1986; Henderson *et al.*, 1990]. Hence, the resolution obtainable from a specimen is directly proportional to the total applicable dose and its radiation sensitivity.

A potential way to increase the SNR is to minimize the detector noise and at the same time increase its sensitivity. The detective quantum efficiency (DQE) is a property of the detector describing how efficient incoming electrons can be detected [Weickenmeier *et al.*, 1995; Ruijter, 1995], this property can also be expressed in a conversion factor. Commonly used detectors are charge-coupled devices (CCDs) [Krivanek and Mooney, 1993]; they convert the electrons into photons using a scintillator and convert the photons back using a CCD chip [Janesick, 2001]. Because of this intermediate conversion of the electrons to photons and back to electrons, the DQE is usually low [Ishizuka, 1993]. The same principle is used in complementary metal-oxide semiconductor (CMOS) detectors with a slightly higher DQE [Faruqi and Henderson, 2007; McMullan *et al.*, 2009b]. The best way to minimize detector noise however is the use of a direct electron detection device, which avoids any conversion and thus should have an almost ideal DQE similar to or at least that of photographic film [McMullan *et al.*, 2009a]. These direct detection devices, however, have a limited life span, since the high-energy electrons damage will the sensor over time. Therefore, the application of these devices is still limited.

Another resolution-limiting factor of the detecting device is its spatial frequency response. It is defined as the contrast at a given spatial frequency and characterized using the modulation transfer function (MTF). High spatial frequencies correspond to high-resolution information, so the detector should be as sensitive to these high frequencies as possible. A perfect detector counts an incoming electron (point source) with a signal in exactly one of the detector pixel elements while the neighboring pixel elements register no signal (point response). However, in any real-world detector the point source is spread out which results in a typical point-spread function, it's Fourier transform represents the MTF.

The sensitivity and frequency response of a CCD detector is mainly dependent on the thickness of its scintillator, typically made up of a phosphor alloy. For a thin scintillator,

few photons are created by an incoming electron, generating a signal in a small area of the CCD chip and thus providing a good frequency response, but at the expense of a low sensitivity and high noise. In a thicker scintillator, many photons are generated from an electron, causing high sensitivity of the detector and low noise in the micrograph, but at the expense of a deteriorated localization of the signal on the CCD chip. Depending on the application and the amount of electrons the specimen can tolerate, the thickness of the scintillator should be selected to balance sensitivity and frequency response.

An important step to efficiently use the total dose that a frozen-hydrated specimen can endure before being destroyed is to limit the exposure of the area of interest. Using a low-dose acquisition scheme [Dierksen *et al.*, 1992; Koster *et al.*, 1992; Braunfeld *et al.*, 1994], all necessary tuning steps that precede the recording of a micrograph are executed at a lateral position adjacent to this exposure area. This way the total dose can be spent entirely on the recording of micrographs of the area of interest, and no dose is "wasted" for additional tuning steps. Moreover, if the structure to be imaged can be found on the specimen in many identical copies, such as isolated and purified macromolecular complexes, the SNR can be increased by averaging many identical copies in the same orientation as typically done in single-particle investigations (see section 1.5). This will decrease the randomly distributed noise while enhancing the constant structure information. However, to average data from different micrographs, their characteristics need to be of consistent "quality". This means that micrographs should be acquired with consistent imaging parameters such as defocus, dose, etc., at best in an automated fashion (see section 2.6).

1.3 Cellular Biology

In cellular biology the TEM is used to visualize cells and cellular organelles [Lucic *et al.*, 2005]. These pleomorphic objects are unique, so no two cells have an identical structure, although they share common building blocks such as ribosomes, membranes, nuclear pore complexes, and the actin cytoskeleton [McEwen and Marko, 1999; 2001; Medalia *et al.*, 2002; Beck *et al.*, 2004]. Therefore, one object needs to be imaged from different projection angles so that a three-dimensional reconstruction can be calculated using techniques such as weighted back-projection [Radon, 1917; Frank, 1992] or simultaneous iterative reconstruction techniques (SIRTs) [Gilbert, 1972].

Electron tomography of a biological sample was first described by Hart and Hoppe [Hart, 1968; Hoppe, 1969]. During tilt series acquisition the object is tilted and two-dimensional projections are recorded. Typically a tilt range of maximal $-65°$ to $65°$ is accessible. Higher tilts (above $70°$) are not feasible because the specimen holder will

eventually block the electron beam at a given point due to its slab geometry.

The total dose that can be spent on the sample is divided over the whole tilt series [Hegerl and Hoppe, 1976; McEwen *et al.*, 1995]. Thus a total dose of $50\,e^-/Å^2$ spent over 100 images results in single projections with a dose of only $0.5\,e^-/Å^2$, decreasing the SNR in the final micrographs considerably and thus require higher defoci to increase the contrast conditions (see section 2.1.5). The resolution of the reconstruction is also dependent on the tilt increment [Crowther *et al.*, 1970]. While a smaller tilt increment will result in more projections, it will considerably decrease the dose per projection, and thus the SNR. However, one cannot infinitely decrease the dose per image, since it is dependent on the detector response.

Due to the limited tilt range the reconstruction of the tilt series will have a directional distortion and thus a degradation of resolution in this direction because of missing projections. In Fourier space, this missing information can be observed as a "missing wedge". The typical experimental setup of the specimen holder can only tilt the specimen in one single axis, making it impossible to acquire projections of the object from all directions, thus some information cannot be obtained. However, using a special dual-axis or rotatable specimen holder, some of the missing information can be recorded by acquisition of two single-axis tilt series with 90° rotation (dual-axis tomography) [Mastronarde, 1997]. This reduces the missing wedge (33 % missing information) to a missing pyramid (11 % missing information) [Iancu *et al.*, 2005; Arslan *et al.*, 2006], but requires novel alignment and reconstruction algorithms [Tong *et al.*, 2006].

1.4 Visual Proteomics

The approach of visual proteomics aims to generate a molecular atlas of the macromolecular complexes of the cell [Nickell *et al.*, 2006; Leis *et al.*, 2009] and study the interactions of proteins which co-localize forming "molecular factories". To investigate the co-localization and distribution of protein complexes by TEM methods, two sets of data need to be obtained. The first data set consists of tomograms of cells with high-enough resolution to detect and identify macromolecular complexes in the cytoplasm. Using the techniques described in section 1.3, it is possible to acquire cellular tomograms with a resolution in the range of 4 to 6 nm. This resolution is sufficient to detect quaternary structures of protein complexes inside of the cell. The second data set that needs to be obtained is a library of 3-D structures of macromolecular complexes. These structures then form a template library that can be used to apply template matching techniques *in silico* [Frangakis *et al.*, 2002] and hence generate information about distribution and

interactions of molecular machines inside of tomographic volumes of entire cells.

The templates can be obtained, e.g., from x-ray crystal structures which usually contain high-resolution structural information. However, there are only few structures of large macromolecular complexes available, since large protein assemblies are metastable, fragile, and prone to disassociation and thus difficult to crystallize. Furthermore, the high-salt conditions during crystallization tend to deform the complexes, making their appearance look different from native cellular conditions.

The cytoplasm of a cell is densely packed with "material" (molecular crowding). Therefore, protein complexes are not found in an isolated environment but are observed in close contact with their neighbors. Molecular crowding thus aggravates the detection and the differentiation of macromolecular complexes inside the cytoplasm [Grünewald *et al.*, 2003]. Moreover, to effectively detect complexes inside cells, i.e., their native environment, their respective templates should resemble their native structure as closely as possible. Electron microscopic methods, e.g., single-particle analysis, are used to generate suitable templates, which will be described in the following.

1.5 Single-Particle Approaches

As previously stated, electron microscopy can be an alternative to generate structures of large macromolecular complexes. To use these structures as templates in visual proteomics studies, one aims for a resolution between 15 to 30 Å. Higher resolution is not necessary because the cellular tomograms where the complexes are to be detected typically have a resolution in this range and the templates need to be filtered to the resolution of the respective tomographic volume. However, when using single-particle analysis as a stand-alone tool to investigate the structure of protein complexes, one aims for resolutions better than 10 Å to identify tertiary and secondary structures of the protein chain. Two techniques are available to generate these structures: the first technique uses tomographic methods to image *in vitro* isolated and purified complexes [Nickell *et al.*, 2007b] or extracts these complexes from cellular tomograms [Ortiz *et al.*, 2006]. The resolution of these individual macromolecules is quite low due to the low SNR of the tomograms. However, since all complexes are identical copies, it is possible to align and average them to increase the SNR and obtain a reasonable resolution of less than 45 Å [Nickell *et al.*, 2007b]. To generate a 3-D structure at this resolution, a couple of hundred complexes are needed, which in turn requires the acquisition of dozens of tomograms with limited field of view (FOV) because of "small-area" detectors. To acquire that many tomograms in a timely manner, automated procedures are therefore necessary. Serial tilt series acquisition (batch tomography) is a high-throughput technique to acquire

automatically multiple tomograms at different specimen positions, preferably with minimal user supervision. For all tomograms, every step such as focusing, tracking, beam centering, etc., need to succeed unsupervised, which requires robust and fault-tolerant algorithms that work under low-dose conditions. Therefore, the development of reliable batch tomography is a complex and challenging endeavor (described in detail in section 2.6.3).

The second technique, known as "single particle analysis" [Frank *et al.*, 1986; Radermacher, 1988; Frank *et al.*, 1996], aims to reconstruct a high-resolution three-dimensional structure from 2-D projections and a low-resolution starting model [van Heel *et al.*, 2000; Ruprecht and Nield, 2001; Steven and Belnap, 2005; Zhou, 2008; Jonic and Vénien-Bryan, 2009]. The 2-D projections are extracted from micrographs of isolated and purified complexes. The dose does not need to be fractionated over many micrographs, as mandatory for tomographic acquisitions, which allows higher SNR within a single 2-D projection. The individual particles need to be first detected and "boxed out", forming a stack of randomly oriented views of their 3-D structure. Assuming that the complexes are identical copies, the projection angle of each view can be determined by comparing it to projections of an initial 3-D model. This model can be created from a tomographic reconstruction as described previously or a low-pass filtered simple geometric body such as a cylinder can be used. Then an improved model is generated by back-projecting the views into a 3-D volume. Running this process iteratively one can obtain a refined model of the protein complex. The SNR and resolution of this model can be increased by averaging more views into the structure. Since the SNR is proportional to the square root of the number of particles, one typically needs to average 10 000 to 100 000 particles, or even more, to attain a high-resolution structure.

The assumption that the protein complex has an invariant structure is often not valid. Protein complexes are labile and sometimes metastable, and are moreover subject to structural changes during their working cycle. Thus, generating a single 3D model for a protein complex is usually not sufficient. To create snapshots of the complex in its different functional states multiple models need to be generated [Carazo *et al.*, 1989], e.g., by classification methods such as maximum likelihood classification [Scheres *et al.*, 2007; 2008]. This in turn requires even more views of the protein complex, so hundreds of thousand up to millions of projections of the complex are required [Konevega *et al.*, 2007; Nickell *et al.*, 2009].

Assuming a few dozens particle views on each micrograph, it is necessary to acquire up to tens of thousands of micrographs for a single-particle reconstruction. These micrographs need to be of constant quality and should be recorded at distinct and unchanged imaging parameters such as defocus or dose. Manual recording is tedious, takes a long

time, and furthermore it needs an experienced expert. This raises the need for automated procedures to acquire large data sets in a high-throughput fashion as fast and efficiently as possible (see section 2.6.1).

1.6 Instrumental Advances towards Automation

Automated electron microscopy is based on a number of enabling technologies. The assessment and development of these technologies took place over the last two decades. A brief overview of the key innovations leading to automation will be given in the following.

In automated microscopy the human operator is replaced by a software logic that performs the same preparation and acquisition steps at the microscope. Depending on the level of automation, either the operator is assisted by the computer program or the software is in total control of the acquisition process with no human supervision.

A fundamental requirement for any acquisition software is the possibility to control the microscope direclty via a computer. Therefore, the microscope has to be equipped with an interface where hardware parameters can be sent and received. Microscopes equipped with this interface are, e.g., Philips' CM series and FEI's Tecnai series (FEI Company, Eindhoven, The Netherlands), the latter further optimized for computer control. With the advent of computer-controlled microscopes it also became possible to implement so-called low-dose acquisition operations; the ability of the microscope to store specific "states" for focusing, tracking and acquisition (e.g., during a tilt series). The operator was now able to switch between these optical states with the push of a single button while several parameters in the electron optics were changed (e.g., magnification, illumination conditions, image and beam shift parameters). As an example the "beam blanker" was introduced blocking the beam before it reaches the sample in cases where no micrograph is acquired. In this way the exposure of the sample with electrons can be controlled and minimized.

Switching between these states in a reproducible manner demanded greater stability and reproducibility of the optical lenses and coils of the microscope. Whenever the current in an electromagnetic coil system is changed or switched off and on, the electromagnetic field inside of the lens changes slightly due to well-known hysteresis effects. This implies that the electron-optical conditions usually differ after changing states, or that they only reach their approximate original positions with a long delay. Therefore instrumental improvements to increase the stability of the lenses and increase their reproducibility were necessary. To date, most microscopes have incorporated means to minimize the hysteresis of the lenses (see section 2.1).

The specimen holders used for automated acquisition also need to comply to strict

specifications in terms of stability at liquid nitrogen temperature. To minimize resolution-limiting motion blur in the acquired micrographs, the holder drift needs to be less than $2\,\text{Å}\,\text{s}^{-1}$. Furthermore, the stage's precision of movement needs to be within a limit of a few hundred nanometers in order to accurately center the features of interest. Additionally, to allow for dual-axis tomography the specimen needs to be rotated preferably inside of the microscope column. Modern stages and holder systems such as the one implemented in the Titan system (FEI Company, Eindhoven, The Netherlands) allow precise manipulation of the specimen position under vacuum and liquid nitrogen temperature. Once moved, the sample drift is within below $1\,\text{Å}\,\text{s}^{-1}$ within less than 1 min (see section 3.1.2), and the typical lateral stage accuracy is in the range of 300 nm to 500 nm (see section 3.2.4).

Another essential requirement towards automated microscopy was the introduction of detectors that were able to record micrographs and transfer them digitally to the control computer for storage and evaluation, e.g., during tuning operations. Before the introduction of CCD cameras [Krivanek and Mooney, 1993], micrographs were typically recorded using photographic film which had to be developed and digitized manually. Tuning and alignment steps such as focusing were done manually either on fluorescent screens or TV camera systems. Using digital detectors, micrographs can meanwhile be recorded automatically and are available in digitized form within seconds. The first generation of these detectors had a limited sensitivity and FOV. However, modern cameras such as the FC816 CMOS camera (TVIPS GmbH, Gauting, Germany) have overcome some limitations and are almost equivalent to photographic film.

Specimen preparation and handling has also improved substantially over the last decade. A big advantage of TEM in biology is the low amount of protein or cellular material needed. Theoretically, to collect millions of particles, only few nanograms of material are necessary. Thus, structural investigations of protein complexes with low abundance can be performed without the need of large-scale purification methods as would be necessary for x-ray crystallography. Moreover, using only tens to hundreds of cells, a wealth of data can be collected to investigate their cellular structure. Therefore, in theory, one single specimen grid of good quality would be sufficient to perform a complete research project. However, during imaging of the specimen, sample material is evaporated by the electron beam. This vapor is mainly being intercepted and deposited on the cryo-shields which will protect the sample from ice contamination. Nevertheless, a small amount of vapor however will directly deposit on the specimen surface forming a continously growing layer of ice contamination. Due to this contamination buildup over time, the maximum time a specimen can be used for an acquisition is in the range of one to four days [Cheng *et al.*, 2006] and highly dependent on the utilized equip-

ment (see section 3.1.3). Therefore, a number of specimen grids (typically 10–50) need to be prepared with reproducible quality in terms of thickness, particle concentration, and distribution. It goes without saying that in order to validate the scientific findings with one sample, the results need to be cross-checked for reproducibility using multiple specimens.

Only a consistent imaging quality over all micrographs of all specimens makes it possible to obtain high-quality 3-D structures of the sample. Besides manual specimen preparation such as plunge-freezing, which is often unreliable in terms of quality, specimen-preparation robotic systems have been developed, such as the VitroBot (FEI Company, Eindhoven, The Netherlands). These systems are able to prepare vitrified specimen grids under environmentally controlled conditions yielding in the end a consistent specimen quality [Iancu *et al.*, 2006].

Automated sample screening and acquisition is assisted by automated loading of specimen grids into the microscope. As an example, the Titan Krios AutoLoader is capable of storing up to twelve frozen-hydrated grids for extended periods of time at cryo-conditions and allows an unsupervised and automated transfer into the specimen holder of the electron microscope.

1.7 Software Developments for Automated Acquisition

Automated acquisition of dose-sensitive frozen-hydrated specimens became possible with the invention of low-dose acquisition schemes. These schemes define "states" for distinct microscope settings and acquisition tasks. They thus control and minimize potential beam damage to the sample [Dierksen *et al.*, 1992; Koster *et al.*, 1992; Braunfeld *et al.*, 1994]. To minimize electron dose on the acquisition area the states are placed adjacent to each other using the image-beam shift system [Koster *et al.*, 1992]. One can summarize the concepts of low-dose acquisition and semi-automation mentioned above as first-generation data collection approaches [Koster *et al.*, 1989], which enabled scientists to acquire tilt series of frozen-hydrated specimens under low-dose conditions. Taking into account the limited processing power of computers at the time, these programs offered only rudimentary user interfaces and had to keep tuning algorithms simple to keep acquisition times reasonable.

Based on the concept of low-dose acquisition, which is still being used in modern acquisition algorithms, the "second-generation" acquisition programs were developed. Some of these software packages are available as script toolboxes that provide the user with the tools necessary to build their own acquisition program tailored to their needs [Shi *et al.*, 2008; Nickell *et al.*, 2005; Suloway *et al.*, 2005]. Other approaches de-

liver a more sophisticated user interface that can also be used by non-experts. Altogether they provide a higher level of automation during acquisition but are mostly limited to one specific acquisition scheme, such as tomography [Braunfeld *et al.*, 1994; Kisseberth *et al.*, 1997; Rath *et al.*, 1997; Mastronarde, 2005], batch tomography [Suloway *et al.*, 2009], electron crystallography [Oostergetel *et al.*, 1998; Cheng *et al.*, 2007], single particle acquisition [Carragher *et al.*, 2000; Zhang *et al.*, 2001; Stagg *et al.*, 2006; Zhang *et al.*, 2009] or random conical tilt acquisition [Zheng *et al.*, 2007a; 2007b]. It is worth to mention that a number of commercial developments exist such as FEI Tomography Explore3D (FEI Company, Eindhoven, The Netherlands), 3D Tomography-Acquisition Software (Gatan Inc., Pleasanton, CA, USA) or EMMenu (TVIPS GmbH, Gauting, Germany). However, while these packages offer an easy-to-use interface for novice and advanced users, their acquisition schemes are more rigid. Nonetheless these commercial packages have helped to establish the electron microscope as a valuable tool for investigations in cellular and structural biology.

Some acquisition software packages have been adopted to perform multiple acquisition tasks such as LEGINON [Suloway *et al.*, 2005] or the TOM Toolbox [Nickell *et al.*, 2007b]. However, until now, no single acquisition package exists that provides a broad flexibility to accommodate for most acquisition schemes, such as tomography and single particle acquisition or variations therein.

Since automated acquisition is being increasingly used, there is also a growing need to organize the acquired large data sets. New developments aim to incorporate post-processing steps to evaluate the data on-line during and directly after acquisition. LEGINON is the first software to also incorporate a book-keeping algorithm that feeds a database system and thus facilitates image processing [Lander *et al.*, 2009].

1.8 Aims of this Work

The use of TEM in structural biology has been established in the last decade. Nevertheless, using an electron microscope is still a complex and demanding task. An expert user is required to prepare and handle the delicate specimens and use the existing acquisition software in order to collect data sets in a systematic and controlled way. Especially if high-resolution structural information is needed, the acquisition is demanding and becomes time consuming since really large data sets (up to several terra bytes) are required.

The existing software packages assist the user in recording micrographs and are well-suited for specific tasks such as tomography or single particle acquisition. However, while they relief the user from performing complex tuning steps manually, they also limit him in terms of functionality. For example, a software package that was designed for acquiring

tomograms is not well suited for the acquisition of single particle data. Therefore, one would either have to modify the existing software (assuming the source code is available) or switch to another software package which would be better-suited for the specific task. Moreover, not all packages can be used in conjunction with all microscopes, therefore the choice of software packages may depend on the instrumental platform being used. The latter presents a disadvantage since changing software packages involves re-training of the user, since all packages provide a different user interface.

The aim of this work was to design and implement a new acquisition software, called TOM^2 , using the concept of low-dose acquisition and automated tuning algorithms. The algorithms from different packages (e.g., auto focusing, automated beam centering, etc.) were evaluated, optimized, and implemented in a common framework. The algorithms were equipped with fail-safe triggers to handle situations during acquisition where an auto function is not able to tune the optics as intended. In such cases the original optics settings are restored and acquisition can resume.

The number of input parameters were minimized to make it easier for the user to quickly utilize these methods without the need to have deep knowledge about the algorithms used to perform the specified task.

TOM^2 was not designed with any specific acquisition task in mind. Instead, the goal was to develop a software where the user could design custom acquisition schemes. The acquisition schemes that are being used today, such as tomography, were analyzed and dissected into a hierarchical system of reusable building blocks. By rearranging a fixed set of these building blocks, the user is now able to design and modify existing acquisition schemes. Moreover, one is able to invent and develop novel acquisition approaches. Using GUIs there is no need to use programming or macro scripting languages. Therefore the software can be used without inside knowledge of its internal programming.

TOM^2 uses a hardware abstraction layer (HAL) to separate the GUI from the code that communicates with the microscope hardware. This enables TOM^2 to be used on different microscope setups, independent from make and model.

In the following, the parts of an electron microscope and their function are introduced. Then, the design principles of TOM^2 are explained and the automated tuning algorithms are described. On the basis of these algorithms, the hierarchical acquisition scheme is documented and example acquisition schemes for tomography and single particle acquisition are shown. The performance of the Titan Krios prototype microscope is evaluated and compared with the performance of a Tecnai "Polara" microcope using a benchmark test that was performed using TOM^2 . The application of TOM^2 is demonstrated using some examples of cellular and structural biology applications. Finally, future extensions of the software and possible usage scenarios are discussed.

2 Materials & Methods

2.1 The Electron Microscope: Parts and Function

The TEM, first developed by Ernst Ruska [Ruska, 1987], is based on the same optical principles as a light microscope; instead of light and glass lenses, electrons and electromagnetic lenses are used with the advantage that their focal length is variable by changing their electrical current. To control the collimation of the beam, retractable and fixed apertures are additionally introduced in various positions within the microscope column.

The electrons are generated and accelerated with the electron gun using either a thermionic element (Tungsten or LaB_6 crystal) or a Tungsten single crystal in <111> orientation as a field emission gun (FEG). The latter produces a highly coherent, intense beam and thus is normally favored for high-resolution imaging. Underneath the extraction anode of the FEG is a small electrostatic lens, the gun lens. This lens is used to form the first cross-over after the gun in relation to the first beam-defining aperture. A "strong" gun lens is used when small, intense and low-aberrated electron probes are needed (e.g., diffraction and scanning), while a "weak" gun lens is used when large beam diameters are important and thus higher total beam currents are needed (TEM imaging, low dose).

An evenly, parallel illuminated beam is formed by the condenser system. Typically a two-condenser system is used; while condenser 1 (C1) controls the spot size of the beam; condenser 2 (C2) controls the size of the beam (intensity), however the "integrated" intensity stays constant for a given spot size. The Titan Krios microscope has a three-condenser system. The condenser 3 (C3) allows the convergence angle of the beam to be adjusted independently of the C2 lens setting.

After passing the specimen, the image is magnified and focused by the objective lens. The projection system consists of a set of lenses and is used to further magnify the image of the specimen and to project it onto the detecting device. The projection system can also be used to obtain a magnified diffraction pattern of the specimen, which is used for example in diffraction applications, e.g., electron crystallography.

Alignment of the beam is vital since the beam has to pass through the lens centers in

order to minimize aberrations. The beam can be moved and tilted at specific points of the microscope column to pass through the lens centers using different sets of deflection coils. The microscope is equipped with three sets of double deflection coils: gun, beam (above the objective lens) and the image deflection coils (below the objective). The coils are able to perform an independent shift and tilt allowing precise directional orientation of the electron beam. Figure 2.1.1 illustrates the optical path of the electron microscope and the position of the aforementioned lenses and coils. In the following the capabilities and limitations of the imaging system are discussed with regards to low-dose imaging of biological specimens.

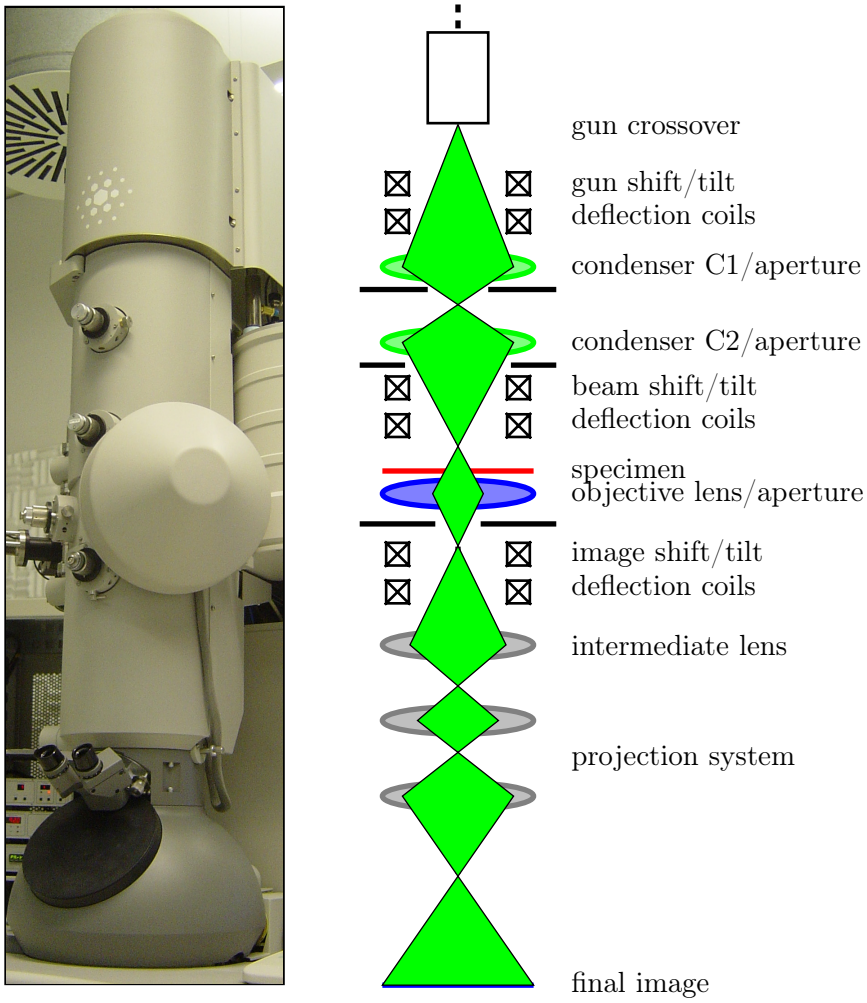

Figure 2.1.1: Optical path of an electron microscope. Depicted is a two-condenser system (Tecnai F30 "Polara", FEI Company, Eindhoven, The Netherlands).

2.1.1 Magnification

The magnification of the microscope is determined by a global lens current setting affecting all lenses at the same time. A list of lens currents are stored for different magnifications and provided by the microscope. Each entry in this list (lens series) can be accessed using a "magnification index". Changing this index sets the assigned lens currents and thus changes the magnification. This means that the magnification can be set only in discrete predefined steps and not arbitrarily. Therefore, the magnification index is the basis of the imaging parameters. To increase the optical stability, e.g., after switching the magnification, and to avoid large hysteresis effects within the electromagnetic lenses, one can use double-coiled lenses, as implemented in the Titan Krios microscope. In this setup, one coil is working at a constant current, while the second coil is adjustable in very fine increments.

2.1.2 Illumination Control

For dose-sensitive samples such as vitreous biological specimens it is of utmost importance that the beam only illuminates the specimen during the acquisition of a micrograph. During the rest of the time the beam should be blanked in order to avoid unnecessary damage. Blanking of the beam is achieved by switching the gun tilt coils to a setting where the beam is deflected away from the sample, as opposed to a setting where the beam is centered in respect to the whole projection system.

To acquire a micrograph that is neither over- nor underexposed, the illumination on the detector and thus the sample has to be controlled. Since the detector has a certain counting range for detecting electrons, the counts on every pixel of the detector must be in this counting range to avoid over- or underexposure. The detector integrates the signal of the incoming electrons over time; therefore, the mean counts in every pixel can be controlled by adjusting the detector readout time. This readout time must be set in a range where stage drift is minimized and smearing effects due to overly short exposure times are avoided.

The brightness of the illumination system needs to be adjusted in order to allow an optimal exposure time. The strength of the C1 lens is changed by changing the spot size. Spot sizes are reflected in a list of indexed settings (for FEI microscopes, spot sizes of 1-12 are available) where smaller numbers correspond to smaller beam areas and result in a brighter spot. Depending on the acquisition task, different spot sizes are used. For single particle acquisition, where the total dose is used to record only one or two micrographs at one sample position, a small spot size (usually 3) is used to decrease exposure times and lessen the influence of drift. For tomography, where the total dose is

fractionated over approximately 60 or more images, higher spot sizes (6–8) are typically used to "dim the illumination" and allow acquisition of numerous low-dose micrographs.

The beam size on the sample is also an important factor for illumination. Changing the strength of the C2 lens (so-called "intensity" on Tecnai or "illumination area" on Titan microscopes) controls the spreading of the beam while the integrated intensity remains constant. For TEM imaging the size of the beam has to be larger than the FOV of the detecting device, so the minimum beam diameter is determined by the detector array. The diagonal size of the detector array defines a beam size of 1.0 FOV. Usually, beam sizes of 1.1 to 2 FOV are being used. In summary, the interplay between the condenser lens system together with the detector exposure time allows a precise control of the applied electron dose. The dose is defined as the absorbed radiation energy per specimen area per time, the SI unit is "gray". One gray is the absorption of one joule of energy, in the form of ionizing radiation, by one kilogram of matter. In electron microscopy the dose is measured in electrons per area per second.

The interplay of the C1 and C2 lens system also determines the beam convergence angle. For optimal illumination of the sample the ray bundle of the electron beam should be parallel. Non-parallel illumination (such as in convergent or divergent ray bundles) causes non-isoplanatism (invariances over the field of view) and thus local defocus and magnification variations in the micrographs [Fan *et al.*, 1995]. Defocus variations are caused because the outer parts of the illuminated area of the specimen are imaged by outer parts of the objective lens. The spherical aberration of the objective lens causes an increasing focusing strength at the outer parts of the objective (see figure 2.1.2). Magnification variations are caused when a diverging beam in combination with a non-planar or tilted specimen is used. Specimen regions that have less distance to the objective lens center will be projected with lower magnification than regions that are further away from the objective lens center (see figure 2.1.3). Especially for tomography, this change in magnification of a feature over the tilt series can severely limit resolution, especially when using a detector with a large FOV.

When using a two-condenser system such as implemented in the Tecnai series microscope, the beam convergence angle is highly dependent on the beam size, so that only one beam size setting will produce a perfect parallel beam. Divergence from this condenser setting will always lead to slightly convergent or divergent illumination conditions. The Titan microscope has a three condenser system, which allows control of the beam convergence angle at the specimen for varying beam diameters, thus guaranteeing parallel illumination at all times, provided that the condenser system is well aligned.

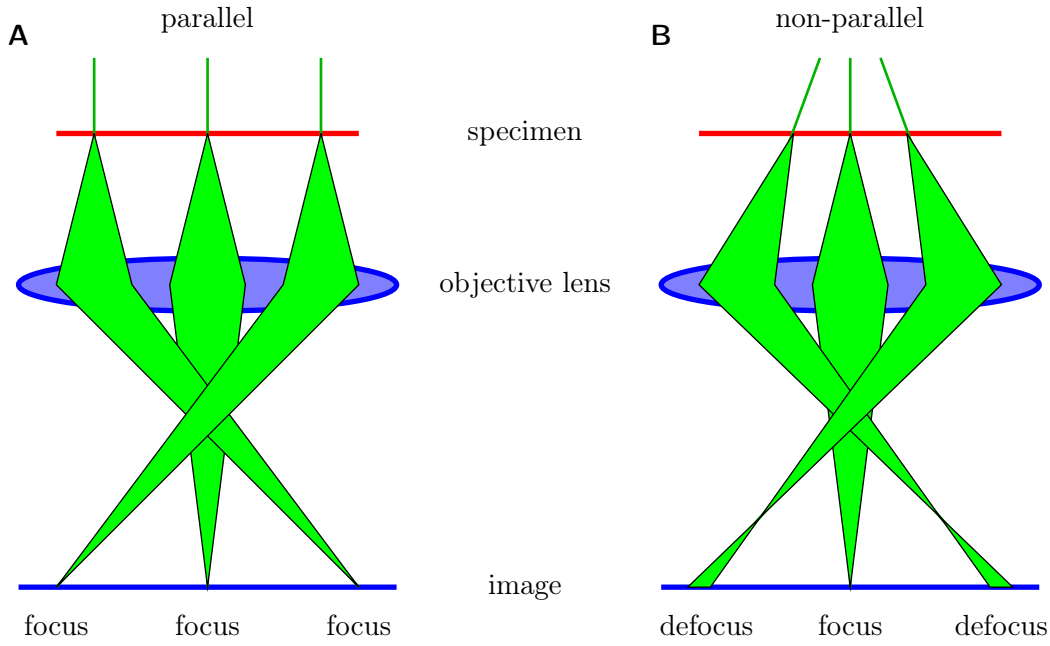

Figure 2.1.2: (A) Parallel illumination will produce a focused image of the specimen. (B) Variations of defocus caused by non-parallel illumination conditions. The spherical aberration of the objective lens causes variations of defocus in the micrograph if the electron beam is not parallel on the sample.

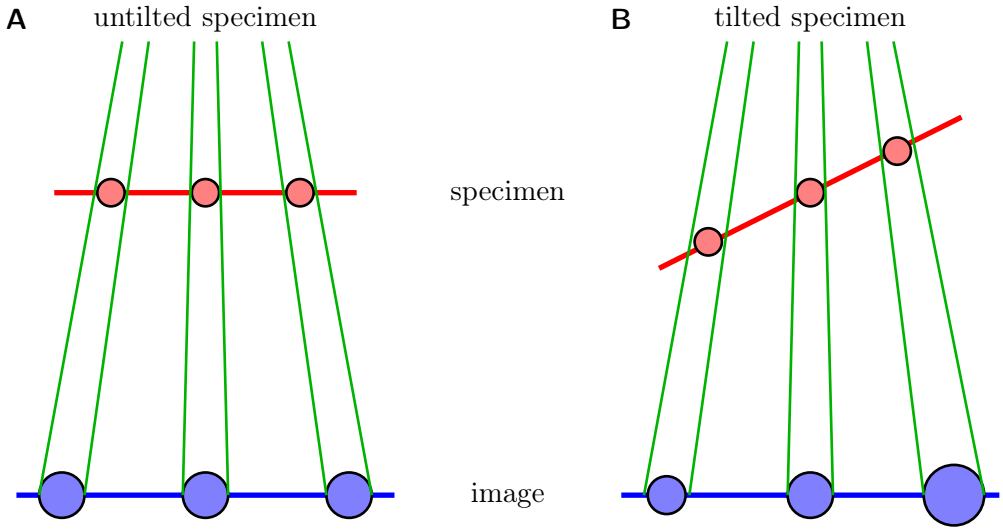

Figure 2.1.3: Variations of magnifications caused by non-parallel illumination conditions. (A) Non-parallel illumination of an untilted sample produces no local changes in magnification. (B) When a specimen is tilted in a non-parallel beam, objects closer to the objective lens are less magnified than features further away from the objective lens.

2.1.3 Stage

The specimen stage is located between the objective pole pieces of the microscope. The stage allows movement of the specimen under cryo-conditions in four degrees of freedom on Tecnai microscopes (x, y, z, α tilt), and five degrees of freedom on Titan Krios microscopes (x, y, z, α tilt, β tilt). These movements are realized mechanically by step motors or piezo motors. Since the stage mechanics have a certain play (so called backlash) the movements are only accurate in a range of a few hundred nanometers (typically 300 to 500 nm) see section 3.2.4). When dealing with a FOV in the range of 800 to 1000 nm, it is clear that this movement must be as accurate as possible, or iteratively refined. Additionally, once the stage has been stopped at a new position, the specimen continues to drift for some time due to its mass inertia. Since such drift limits the attainable resolution of a micrograph, high-resolution imaging requires that the acquisition be paused until the stage has settled and the drift is below a certain threshold (e.g., $1\,\text{Å}\,\text{s}^{-1}$). Depending on the stage and the amount of movement, this pause can last up to a few minutes.

The α-tilting mechanism of the stage is constructed to allow for tilting without large apparent movements of the area of interest. Eucentric-tilting is achieved by bringing the area of interest to the same z height as the α-tilt axis of the stage. This z height is called the eucentric height, and it serves as a reference height inside of the microscope for all alignments. However, due to mechanical inaccuracies and backlash effects, the area of interest will slightly move out of the FOV during tilting, even if the eucentric height was adjusted. In order to keep the area of interest centered during acquisition of a tomogram, this stage movement needs to be compensated. One approach is to assume that the specimen holder movement is reproducible and to determine a holder tilt calibration, recording the stage lateral movement in relation to the tilt angle. Another approach uses an area next to the area of interest to measure lateral movements during acquisition and correct them on-the-fly. This approach can also account for sudden lateral movements and is thus more robust but also more time consuming since additional micrographs need to be recorded during tilt-series acquisition. See section 3.2.2 for a detailed analysis of the stage behavior during acquisition.

2.1.4 Image Beam Shift

Centering a feature of interest using the stage is hampered by its mechanical accuracy and is often insufficient, especially at higher magnifications. Moreover, due to drift the acquisition has to be paused after each movement; which will increase the acquisition time and decrease the number of obtainable micrographs per given time frame. An

alternative method changing a sample position is done by repositioning the beam using the beam shift coils; in this case the specimen stage remains fixed. However, a beam shift induces an image shift and vice versa, i.e., moving the beam induces a movement of the image shift coils. To account for this cross-interference one has to adjust both coils at the same time. This concerted movement allows the beam / image to stay centered and be imaged onto the detector system. Most modern microscopes allow parallel movements of the image and beam shift coils; but such movement needs to be precisely calibrated (see figure 2.1.4).

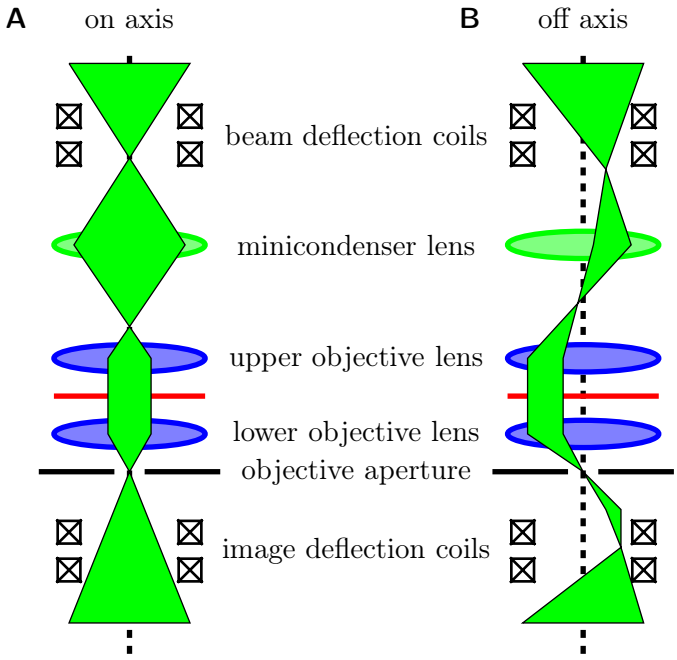

Figure 2.1.4: The image beam shift system. (A) Without applied image-beam shift the beam passes through the lens centers. (B) The beam path can be changed using the beam shift coils to illuminate a different sample area. Using the image shift coils the beam is readjusted after passing the specimen so that the detector is again illuminated evenly. Note that using this technique the beam does not pass the lens centers anymore introducing aberrations, so shifts should be limited to avoid large distortions of the image. The maximum range of the coils is $\pm$ 10 µm.

Changing coils or lens settings and stabilization only requires a few seconds, which allows for fast repositioning of the beam, circumventing the need for tedious and time consuming stage movements. However, the extent of movement is limited by the range of the beam and image shift coils. The typical image beam shift range at a magnification of $\approx 50\,000\times$ is $\pm$ 10 µm. Large movements of the beam will result in the beam traversing the objective lenses off-center, thus introducing additional aberrations to the beam.

This in turn will reduce the beam coherence and hence the overall resolution of the micrograph. Advantageously, the precision of the movement is in the range of a few nanometers, so two orders of magnitude better than that of the stage.

2.1.5 Focus

In transmission electron microscopy, focusing is essential in order to control contrast and frequency content of the recorded micrographs. Biological objects such as protein complexes are mainly built from light-weight atoms (e.g., H, O, C, and N) giving rise to very low elastic cross sections and thus a very weak contrast due to their small scattering efficiency. Furthermore the density of protein complexes is in the range of $1.4\,\mathrm{g\,cm^{-3}}$ [Fischer *et al.*, 2004] whereas the density of amorphous ice is $0.94\,\mathrm{g\,cm^{-3}}$. This small difference will result in a weak contrast, making the molecules almost invisible in their ice matrix. To enhance the inherent contrast in low-dose images, one has to increase the phase difference between scattered and unscattered or differently scattered rays, which is typically achieved by defocusing.

The resolution attainable from a micrograph depends on the contrast given by the SNR and the distribution of recorded frequencies. The latter depends on the phase shift of the object's exit wave. Briefly the CTF describes the contrast formation as

$$H(\omega) = -2 \cdot e^{-2B\omega^2} \left[(1-F) \cdot \sin W(\omega) + F \cdot \cos W(\omega)\right] + S(\omega)\,, \tag{2.1.1}$$

where $e^{-2B\omega^2}$ is a dampening factor accounting for various resolution limiting factors [Saad *et al.*, 2001; Glaeser and Downing, 1992], $\sin W(\omega)$ and $\cos W(\omega)$ are the contributions due to phase and amplitude contrast respectively, F is the contribution of amplitude contrast to the image [Wade, 1992; Reimer, 1984] and $S(\omega)$ is an additive noise term [Sander *et al.*, 2003].

Samples comprised of heavy and densely packed atoms such as negatively stained samples or crystalline inorganic material are not sensitive to radiation damage, and thus a high dose can be spent yielding a high SNR and, due to their high atomic numbers, large phase shift. In this case, the signal in recorded micrographs comes mainly from amplitude contrast. Since the normalized amplitude CTF is near 1 at low frequencies, one can adjust the defocus close to zero and still have sufficient contrast. The focus value that provides maximal frequency response is called the Scherzer focus [Scherzer, 1949] and is defined as

$$\Delta f_{Sch} = -1.2 \cdot \sqrt{C_s \cdot \lambda} \tag{2.1.2}$$

where λ is the wavelength of the electrons and C_s is the sperical aberration coefficient, an

instrument-dependent parameter. For an acceleration voltage of 300 kV and $C_s = 2\,\text{mm}$, $\lambda = 1.97\,\text{pm}$, the Scherzer focus is $\Delta f_{Sch} = -75\,\text{nm}$, represented in the first zero-crossing of the CTF. By chosing such a focus value, one creates a wide band containing low spatial frequencies, transferred with similar phase and thus maximizing the micrograph's information content.

As stated above, since biological samples are very sensitive to radiation damage, the micrographs are recorded under low-dose conditions and thus have a very low SNR. Under these conditions, the objects can be considered "weak phase objects" with a rather small exit wave phase shift. The amplitude contrast is contributing only 7 % to the final image contrast [Wade, 1992], resulting in noisy and low-contrast micrographs. In order to increase the contrast, the defocus Δf can be adjusted by changing the excitation of the objective lens at the expense of attenuating the higher frequency information and limiting the attainable resolution, as shown in figure 2.1.5. Hence, the defocus value has to be chosen carefully to balance the requirements of high contrast and maximum obtainable high-frequency information.

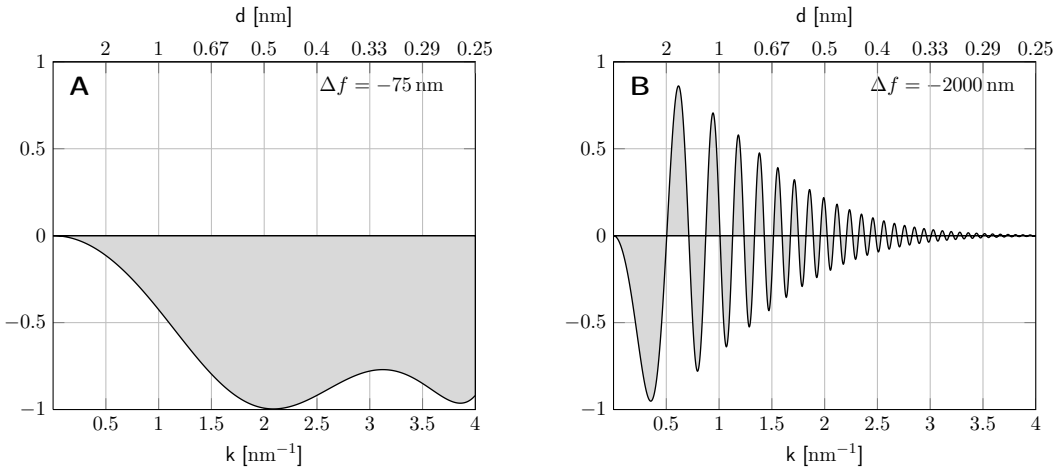

Figure 2.1.5: CTF at different defocus. (FEI Tecnai F30 "Polara" microcope: $V = 300\,\text{keV}$, $C_s = 2.0\,\text{mm}$, $C_c = 2.0\,\text{mm}$, $\Delta E = 0.7\,\text{eV}$) (A) When using a small defocus (Scherzer focus, $\Delta f = -75\,\text{nm}$) the high frequency information is obtained with high intensity, but the image contrast is low because of the low amplitude of the CTF. (B) Increasing the defocus value to $\Delta f = -2000\,\text{nm}$ also increases the amplitude of the low frequency information resulting in acceptable image contrast but degrading the high frequency information in the image because of fast oscillations of the CTF and also because of the dampening effect of the envelope function.

Another option to increase the phase shift of the objects' exit wave is the use of devices such as phase plates [Nagayama and Danev, 2009]. Thin film phase plates

(Zernike type) consist of a continuous amorphous carbon film with a small central hole which will be placed in the back focal plane of the objective lens. The zero-order beam passes through the central hole while electrons scattered at the thin carbon film are phase-shifted by $-\pi/2$, depending on the film's thickness. At Scherzer focus, this phase shift increases frequency response at low frequencies and thus increasing contrast in the recorded micrograph.

For thick specimens the depth of focus is smaller than the thickness of the sample, in this case a focal series can be acquired if the sample can take the necessary amount of dose (for example plastic sections) and the exit wave can be reconstructed from this focal series [Han *et al.*, 1997].

To determine the focus precisely, a common method is to acquire a pair of micrographs with different beam tilts and measure the induced image shift [Koster *et al.*, 1989; Koster and de Ruijter, 1992]. To tilt the beam, the beam deflection coils are being used. For details about this method, see section 2.3.7.

2.1.6 Objective Lens Rotation Center

As previously stated, the objective electron lens focuses and magnifies the image of the specimen. Adjustment of the strength of the lens will result in a slight image rotation (less than 1° per 1 µm change in defocus). Furthermore, the image slightly shifts if the electron beam does not travel through the exact center of the lens and along the optical axis of the microscope. To minimize aberrations and image shifts, which will move the feature of interest out of the FOV, the beam has to be moved and tilted so that it passes through the objective lens' center. If the rotation center is set correctly, the electrons travel in spiral trajectories around the optical axis, thus a beam tilt will not induce and image shift. In all other cases will travel and rotate about a position off-axis when the settings of the objective lens are changed and result in image shifts during beam tilting.

The objective lens rotation center is especially important since the accuracy of the defocus measurement (see section 2.3.7) relies on the fact that no beam tilt induced image shift occurs when the image is exactly in focus. However, the rotation center will slightly drift over time due to lens current instabilities and needs to be refined periodically.

2.1.7 Lens Astigmatism

The electromagnetic electron lenses are not built perfectly and therefore their electromagnetic field is not perfectly round. These lens imperfections cause a loss of rotational symmetry of the beam. In one direction the lens will therefore focus more strongly than

in the perpendicular direction, causing an asymmetry which is called stigmatism. This defect is corrected by a stigmator, a tunable quadrupole coil system that is used to introduce slight variations in the magnetic field of the lens and thus helps to compensate these imperfections. The microscope is equipped with three sets of stigmators, the condenser stigmator, the objective stigmator and the diffraction stigmator. The first is used to obtain a circular beam. The second is used to correct axial astigmatism that is closely related to defocus. Axial astigmatism can be seen in the power spectral density (PSD) as an azimuthal variation in amount of defocus and introduces directional elongation of image features. This type of astigmatism is exacerbated by electrostatic charging of the objective aperture or the sample caused by nonconducting layers, such as ice contamination on the sample or "dirt" on the aperture rim. The third stigmator is used to correct astigmatism in the diffraction pattern and the low-magnification image.

The stigmators should only be used to tune the stigmation of the electron beam by slightly varying its shape and tuning the microscope alignments.

Since the amount of astigmatism tends to change over time due to the aforementioned charging effects and lens instabilities, it needs to be refined periodically, especially when using a high magnification (above 50 000 ×) and low defocus values (below 4 µm) where the amount of astigmatism is clearly visible.

2.1.8 Energy Filtering

Inelastic and multiple scattering events become more frequent with increasing object thickness, limiting the contrast in the acquired micrographs. The inelastic mean free path of electrons in vitrified ice is dependent on their acceleration voltage and is in the range of 200 nm for voltages of 120 keV and 350 nm for voltages of 300 keV [Grimm *et al.*, 1996b; Feja and Aebi, 1999]. Inelastically scattered electrons have lost kinetic energy through scattering events (they are thus "chromatic") and contribute to a blur in the final image, because they are out of focus [Cosslett, 1969].

Energy filters are available as in-column [Rose and Plies, 1974; Tsuno, 2004] or post-column [Krivanek *et al.*, 1995] versions. They are spectrometers capable of selecting and separating electrons according to their kinetic energy. To increase contrast in the micrographs, zero-loss filtering is used, i.e., only electrons that have a kinetic energy close to the primary energy are allowed to pass the filter [Schröder *et al.*, 1990; Langmore and Smith, 1992; Grimm *et al.*, 1996a]. Zero-loss filtering is achieved by introducing a slit aperture after the magnetic prism which separates electrons of different energies. While the additional optics of the energy filter are fairly stable over time, the position of the slit aperture might vary and has to be re-aligned periodically. Since inelastically scattered

electrons add random noise to the image, energy filtering can also increase the SNR of the micrographs.

Another application of the energy filter is the spatial detection and identification of chemical elements in the specimen [Leapman *et al.*, 2004; Aronova *et al.*, 2007]. To detect the chemical composition of a sample, the energy filter slit is tuned to only collect images of inelastically scattered electrons that have excited core level electrons of specific atoms (ionization edges). However, these inelastically scattered electrons make up only a small fraction of the beam (<1 %), thus to collect enough of them to create an image, the total dose on the sample needs to be very high, potentially damaging a frozen-hydrated sample. Therefore this technique can only be applied to inorganic samples or dose-tolerant biological samples such as sections of plastic embedded specimens.

2.2 Software Architecture

2.2.1 Fundamental Design of the TOM^2 Software

TOM^2 is based on the ideas of the TOM toolbox [Nickell *et al.*, 2005], a collection of functions for the acquisition and analysis of tomographic data [Nickell *et al.*, 2007b] written in MATLAB. The latter is a fourth generation programming language that serves as a rapid development tool.

Initially TOM was designed only for tomography tasks, such as the automated recording of a tilt series, alignment and reconstruction, and the analysis of the resulting tomographic volumes. However, the acquisition part was later modified to additionally acquire single particle micrographs. In this initial setup, images were recorded after moving the stage over selected grid areas in a meandering fashion. At each stage position, the sample thickness was measured using a highly binned micrograph with a very short exposure time to minimize potential beam damage to the sample. If the measured mean counts of this micrograph were found to be in a suitable user-supplied range for acquisition, a focal pair of micrographs was recorded. This was followed by an auto focus routine which corrected the defocus for acquisition at the next sample position [Nickell *et al.*, 2007a]. The acquisition scheme itself was not modifiable, only microscope parameters such as magnifications, spot size, and exposure times could be adjusted to adapt the acquisition to the specific sample conditions.

This TOM toolbox acquisition part was programmed specifically for the Polara G2 microscope with limited adaptability to other hardware systems. It heavily relied on the functions (e.g. auto focus, auto eucentric height, image beam shift, etc.) that were provided by FEI's commercial scripting interface and tomography software, and Gatan's

Digital Micrograph which addressed the detector and energy filter interface.

TOM^2 is a complete redesign of the acquisition framework to overcome the limitations of the TOM toolbox mentioned above. TOM^2 is designed in a completely object oriented way. Real-world objects such as the microscope and its accessories, micrographs and parts of the acquisition scheme (e.g. the stage) were created as self-sufficient modules (objects). Each object acts like an independent "machine", containing all the information and methods needed to manipulate its own data structure. The whole program can be viewed as a collection of interacting objects, with defined relationships acting in a highly concerted fashion. This way, even a complex algorithm such as an acquisition software can be implemented with low amounts of source code, compared to the design patterns used to program the TOM toolbox. This is reflected in the fact that TOM^2 consists of about 30 000 lines of code.

To operate the microscope and perform complex acquisition tasks, a variety of low-level commands need to be sent to the hardware systems and the corresponding return messages need to be interpreted. These low level commands represent basic hardware operations such as moving the stage or changing the excitation currents of the different lens systems. Many hardware parameters are inter-weaved, i.e., changing one parameter will affect a range of other related hardware properties (e.g. changing the beam shift deflection coils will affect the image shift deflection coils). The acquisition needs to be reliable and fault-tolerant to acquire micrographs unsupervised for an extended period of time, and thus robust. This can only be ensured by tightly controlling all hardware parameters and reacting to changes on a global scale. Therefore, these individual hardware commands need to be controlled by interacting objects which resolve this interplay of hardware commands ideally in an unsupervised and automated fashion. The objects of TOM^2 take over the low-level control of the microscope and thus make it easier for the user and the software programmer to perform complex high-level microscope operations. For example, auto focusing can be performed while keeping the stage in the correct z height or an area of the grid can be scanned in a systematic way producing an overview map of the sample.

2.2.2 Design of the Hardware Abstraction Layer

An important requirement for the design of TOM^2 was the ability to run the software with minor modifications on as many different microscope platforms as possible. Although there are many different hardware components available from different vendors, the general operation principle and underlying properties of the hardware component can be considered constant. For example, a microscope can be equipped with different

types of imaging devices that record micrographs, such as CCD cameras, CMOS cameras or direct electron detection devices. The different vendors for these imaging devices (FEI, TVIPS, Gatan, Olympus-SIS) deliver different software development kits (SDKs) for their detectors. The exact hardware commands to control the cameras are vendor specific, however they all share the same purpose: to read out an image as an array of pixels with a defined exposure time, specified readout area and binning mode.

In TOM^2 the hardware abstraction layer (HAL) is a collection of objects and is designed to separate the functions responsible for getting and setting parameters to and from the microscope hardware from the rest of the higher level functions (see figure 2.2.1).

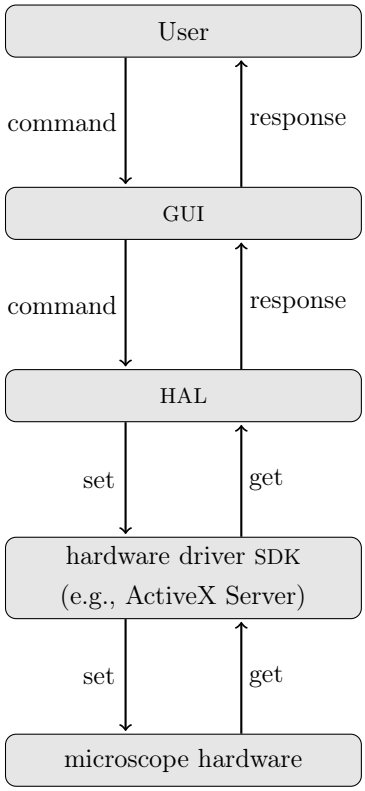

Figure 2.2.1: Software layer organization. User commands are input at the GUI level and translated into general hardware commands. These general hardware commands are used as input into the hardware abstraction layer (HAL) where the general commands are translated into hardware commands for the specific hardware at hand. The other direction translates the specific hardware responses into general responses that are hardware independent. Using this scheme the user is able to input commands into the GUI in a hardware independent manner without the need to get accustomed to the acquisition setup for every specific microscope. All higher level functions and GUIs can be used with any supported hardware in the exact same way.

To organize the different hardware commands, the components of a microscope were determined and for each a hardware class (e.g., energy filter, optics, stage, gun, etc.) was defined. This class defines all common properties that all members of the class share, e.g., for detectors such properties are the readout area, exposure time, and the binning factor. The commands to control each specific hardware component (e.g., TVIPS detectors or Gatan detectors) was then implemented in a subclass, that inherits all properties and methods from the hardware class. This way the common control elements that all components of the same hardware type share, are bundled in the hardware

class and need not be reimplemented in each subclass. Code duplication is avoided and therefore it is possible to rapidly develop a driver object for a new piece of hardware. For example the implementation of the TEAM stage (a high precision piezoelectric stage for material science applications) [Dahmen, 2007] was programmed in a matter of one hour. The implementation of other cameras accessed using the TIA toolkit (FEI Company, Eindhoven, The Netherlands) was finished and tested in under an hour with less than 50 lines of new code written.

Figure 2.2.2 shows different hardware classes and their subclasses implemented in TOM^2 . The individual hardware objects are grouped together into a composite microscope object. This object coordinates the parts of the microscope, executes auto functions and provides a convenient way to communicate with the microscope.

All hardware driver objects are inherited from a master hardware object which implements a cache for parameters. Using this cache, only changing hardware parameters such as defocus or intensity are sent to the microscope, while constant parameters such as magnification or spot size are sent only once. This avoids repeated setting of the same parameter values and thus saving execution time and minimizing potential communication errors with the microscope hardware.

In TOM^2 new hardware can be implemented using an SDK written in the C or C++ programming language; also .NET and ActiveX connections to the hardware driver can be established. Alternatively, network connections are supported. Network traffic is handled in TOM^2 using MATLAB's "Instrument Control Toolbox". These network connections have the advantage of being able to communicate with hardware that is not directly attached to the computer where TOM^2 is executed. Thus TOM^2 can be installed on a computer with better hardware specifications than typically supported by the microscope's hardware provider. As a proof of principle a front end for FEI Tecnai and Titan microscopes was programmed in Microsoft VisualBasic accepting hardware commands on a network port and translating them into ActiveX commands and vice versa. Using this front end, TOM^2 can be executed on any computer running Microsoft Windows, Linux or OS X from any location as long as it can communicate over the network with the microscope computer. This enables remote microscopy applications and can accelerate the acquisition process by running TOM^2 on a 64-bit multi-core workstation with a large memory. Furthermore, this setup allows to process data and execute auto functions faster, and hence yield more data in less processing time, a prerequisite for high-throughput applications. The commands transmitted and received over the network are small (only a few characters per command) requiring not an especially fast connection. Transferring of micrographs over a network connection is also possible but needs a different VisualBasic front end for each camera type. Since micrographs can

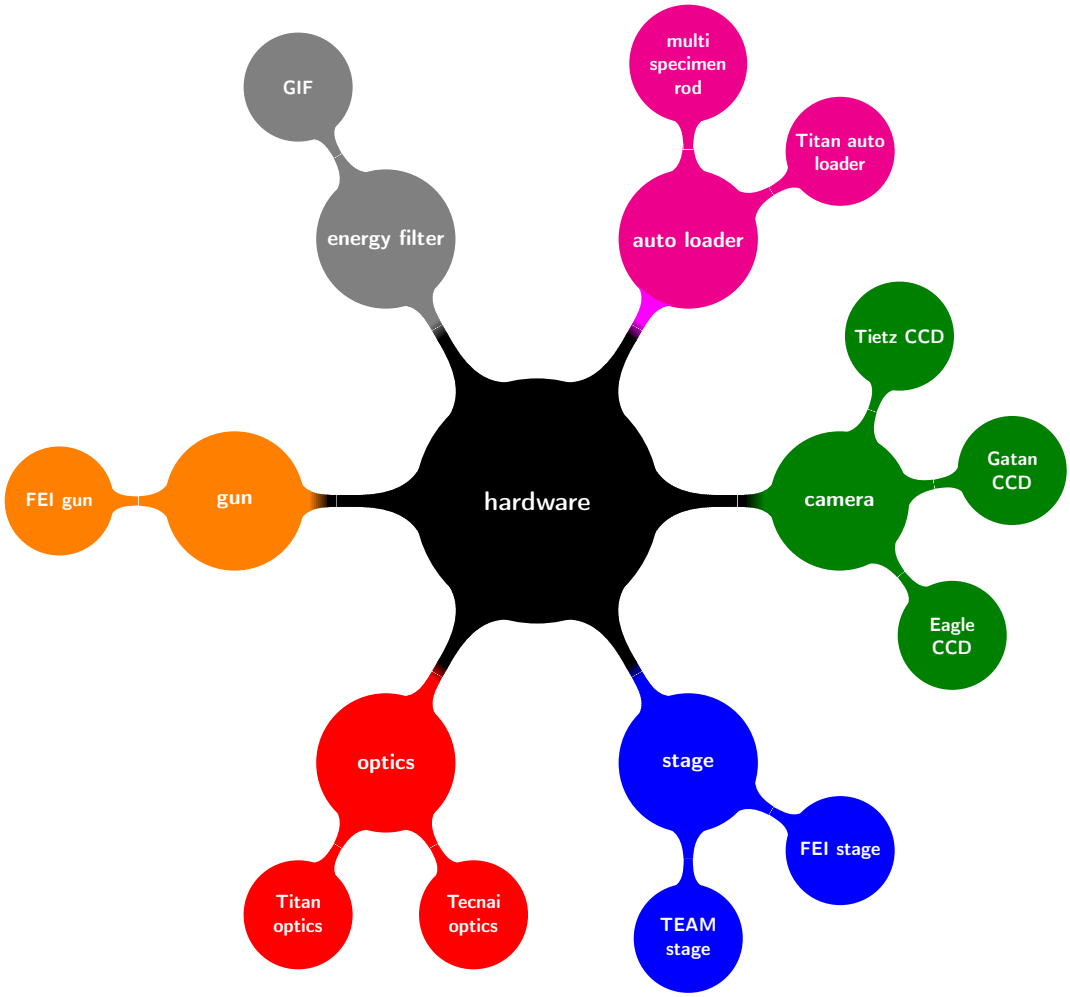

Figure 2.2.2: Hierarchy of hardware driver classes. The central hardware class implements only the methods and properties that are shared by all hardware components. The individual hardware classes (e.g., gun, stage, optics) inherit from this central hardware class, adding methods and properties for the type of device (e.g., the stage class adds x y z position properties which is shared by all types of stages). The hardware control commands are implemented in the hardware subclasses (e.g., TEAM stage, FEI stage) which add the necessary control commands to address the specific hardware. By applying this hierarchical sorting scheme to the source code of TOM^2, the implementation of new hardware can be done by only creating a new subclass under the appropriate hardware class and adding the necessary control commands.

be large (a 4096×4096 pixel micrograph has a size of 32 MB and a 8192×8192 pixel micrograph has a size of 128 MB), it is advisable to use a fast network connection (e.g., GigaBit Ethernet).

2.3 Algorithms for Performing Microscope Adjustments

The following sections describe functions that are capable of adjusting essential microscope parameters in an automated way without the need of any user interaction. The functions translate units from convenient coordinate systems into coordinate systems of the microscope's subsystems such as the image and beam shift system or the stage. These "actions" or "auto functions" are being used during automated acquisition to tune the microscope and acquire micrographs of constant image quality at the user-specified positions of the specimen. All auto functions need to be calibrated first in order to convert their input parameters (typically vectors) into meaningful output parameters. Therefore a calibration step is included in all of the automated procedures; this pre-calibration is performed in a simple and user-frienly way that should require only minimal user knowledge.

The separate actions (e.g., auto focus) are used together with the states to design an acquisition scheme that defines the acquisition strategy for the specific investigation at hand. By measuring and adjusting microscope parameters in an analytical and robust way, they can even outperform the human operator when calibrated properly. Since these functions rely on assumptions and physical models of the microscope optics, they can only function reliably when the optical alignment has been done carefully, they cannot account for misalignments of the microscope's optics.

2.3.1 Detector Corrections

Micrographs acquired using a CCD camera suffer from two distinct sets of artifacts. Artifacts in this case refers to the intrinsic properties of the detection device, which could be addressed as the "personality" of the detector. The first set of artifacts arises from the readout electronics of the camera and is independent of the illumination. The second set stems from the image of the fiber optical stack and the structure of the scintillator array. Latter are dependent on illumination conditions, specifically the number of electrons reaching the scintillator. In order to get an undistorted image of the specimen, both sets of these artifacts have to be corrected in all micrographs as described previously [Dierksen *et al.*, 1992; Ishizuka, 1993].

To correct for illumination independent artifacts the micrograph has to be subtracted

by a dark-reference image which is acquired using the same camera readout parameters but in the absence of the electron beam. The correction of illumination-dependent artifacts requires a dark-corrected gain-reference image with the same mean counts as the recorded, dark-subtracted micrograph. Figure 2.3.1 visualizes the effect of dark and gain correction on a micrograph acquired using an FEI Eagle 4k CCD camera without a sample. Figure 2.3.2 shows the dark-reference and gain-reference images that were used for correction.

Correction of the micrograph is carried out according to

$$i_c\,(x,y) = \frac{i_u\,(x,y) - d\,(x,y)}{g\,(x,y)} \tag{2.3.1}$$

where i_u and i_c are the uncorrected and corrected micrographs respectively, d is the dark reference and g is the gain reference.

To facilitate acquisition of dark and gain references, TOM^2 acquires these reference images with varying exposure times for all binning factors. Other software packages assume a linear dynamic behavior of the CCD camera, and extrapolate from only one gain and dark reference. However, CCD cameras from different providers often do not show a perfect linear dynamic behavior over their entire dynamic range. Therefore, in contrast, TOM^2 assumes a piecewise linear behavior and thus enhances the correction for detector dependent alterations and variations in the recorded micrographs.

Another source of interfering features in micrographs are "hot pixels" caused by electrons or x-ray quanta hitting the CCD detector. "Hot pixels" are generated when a high-energy electron is not absorbed by the fiber-optics stack that protects the CCD array and directly hits a CCD pixel. The result is a high-count value in the respective pixel that will show up as a white dot in the resulting micrograph. These events occur randomly and have therefore to be detected and corrected for each micrograph. Dierksen et al [Dierksen *et al.*, 1992] propose correction methods for "hot pixels" which also affect the rest of the micrograph such as median filtering. TOM^2 corrects only the "hot pixels", while the unaffected pixels in the micrograph remain unchanged. TOM^2 defines hot pixels as

$$i_h\,(x,y) > \bar{i} + 10\;\sigma_i \tag{2.3.2}$$

where $\bar{i}$ and σ_i is the mean and standard deviation of the micrograph respectively. These pixels are replaced by the mean of the nine nearest neighbors, thus do not influence the correlation between images and image normalizations, and avoids a degradation of image resolution.

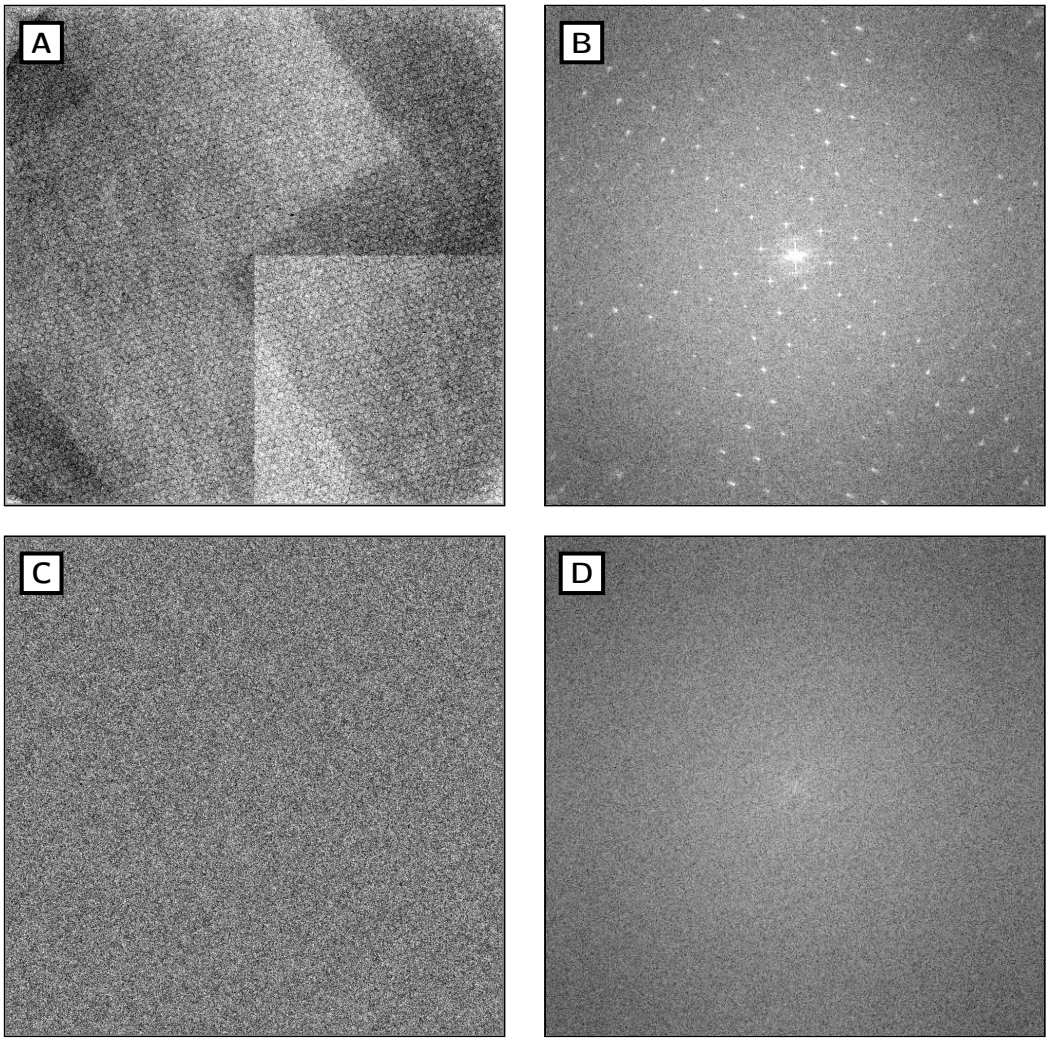

Figure 2.3.1: Dark and gain correction of a micrograph without a sample, acquired using an FEI Eagle 4k CCD camera; pixel size 15 µm. (A) The uncorrected micrograph shows a hexagonal pattern from the structure of the fiber-optics stack, local contrast variations due to varying scintillator thickness, and the noise from the readout electronics. The CCD chip of this detector is comprised of four 2k×2k chips which are combined into a larger array, since these four chips have a slightly different sensitivity due to manufacturing variations, the micrograph's quadrants show slightly different contrast. (B) These artifacts show a strong diffraction pattern in the PSD of the micrograph and would distort the imaged objects in the sample if not corrected. (C) After dark and gain correction, the micrograph contains only random noise; there are no distinct frequencies arising from the artifacts visible in the PSD (D) anymore. When imaging a sample, only the signal generated by the objects in the sample will now be contained in the recorded micrograph.

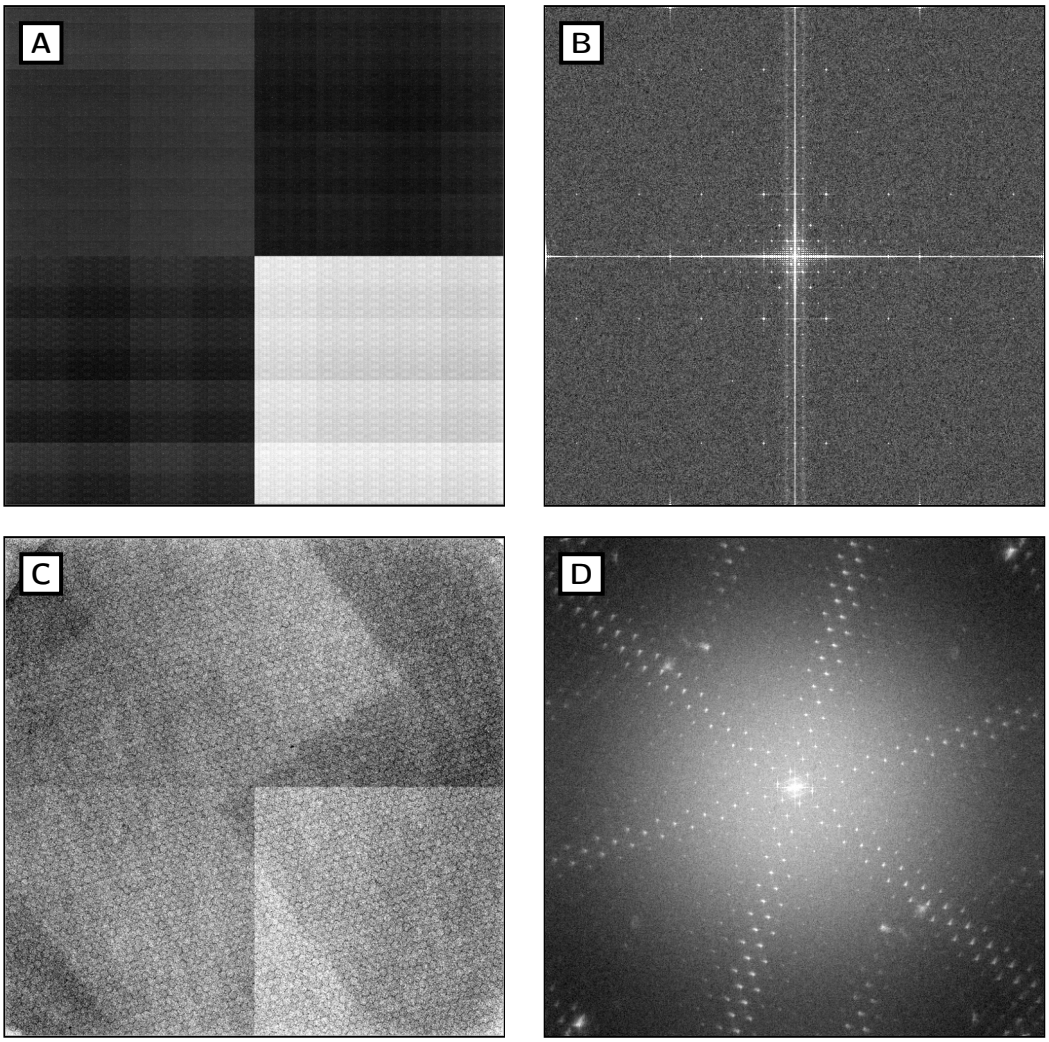

Figure 2.3.2: Dark and gain references of Eagle 4k CCD camera. (A) The dark reference shows few strong features in the PSD (B) from the readout amplifier electronics. (C) The gain reference shows a strong hexagonal pattern arising from the fiber optics stack besides four quadrants of different sensitivity (4-port readout). (D) The hexagonal pattern is also clearly visible in the power spectrum.

2.3.2 Measuring Shifts Between Images

Correlation-Based

In general, the calibration of specific microscope functions and the execution of auto functions involves recording a micrograph before and after a microscope parameter change and a subsequent comparison of the images. The determination of an image displacement, either caused by electron optical changes or by mechanical stage inaccuracies, will be described.

The image recorded after changing the electron optics or the stage position (target image) will exhibit a shift of imaged features with respect to the image recorded before applying the change (template image). This shift needs to be detected in an automated and unsupervised fashion, so that auto functions that utilize the resulting image shift to tune electron optical parameters can be executed unsupervised.

Assuming no magnification change and rotation between the images, the simplest way to compare two images is based on cross-correlation methods. The normalized cross-correlation function (CCF) between the discretely sampled image i and the template t is defined as a convolution in real space

$$\mathrm{CCF}\,(i,t) = \frac{(i\,(x,y) - \bar{i})\,(t\,(x,y) - \bar{t})}{\sigma_i \sigma_t}, \tag{2.3.3}$$

where $\bar{i}$, $\bar{t}$ are the mean and σ_i, σ_t are the standard deviation values of the image and the template respectively; x and y denote the individual pixels of the target and template. The maximum of the resulting two-dimensional correlation function denotes the shift between template and target.

For computational efficiency, the convolution theorem states that the cross-correlation function can be expressed as multiplication in Fourier space [Arfken, 1985]

$$\mathrm{CCF}\,(i,t) = (\mathcal{F}\{i\})^* \cdot \mathcal{F}\{t\}, \tag{2.3.4}$$

where $(\mathcal{F}\{i\})^*$ is the complex conjugate Fourier transform of the target, and $\mathcal{F}\{t\}$ is the Fourier transform of the template.

The normalized CCF uses all available features in the images to calculate their differences. Constant features, such as the detector artifacts decribed in section 2.3.1, will lead to a strong auto correlation peak and could hinder the detection of the maximum of the correlation function. To avoid a potential misinterpretation one has to ensure that only specimen related features will be considered by the CCF. Detector artifacts due to CCD camera readout need to be removed first. Other influences, like contrast variations,

are taken into account by normalizing the CCF (see equation 2.3.3). However, another potential source for a misinterpreted correlation could come from the edge of the electron beam. Especially if a FEG is used, the Fresnel fringes are visible if the beam is condensed [Fukushima *et al.*, 1974], which will show up as low frequencies in the Fourier transform of an image. The subsequent correlation will be dominated by these features and lead to erroneous detection of the shift between the images. For cross-correlation based methods it is required to keep the beam centered and "large enough", .ie., spread over the entire detector array, to avoid such influences. However, this requirement cannot always be guaranteed. To increase the success rate of correlation-based auto functions, the mutual correlation function (MCF) [van Heel *et al.*, 1992] is used. The MCF is defined as:

$$\mathrm{MCF}\,(i,t) = \frac{(\mathcal{F}\{i\})^* \cdot \mathcal{F}\{t\}}{\sqrt{|(\mathcal{F}\{i\})^* \cdot \mathcal{F}\{t\}|}}. \tag{2.3.5}$$

This correlation function weighs the features according to their frequency in Fourier space; higher frequencies are enhanced while low frequencies contribute less to the correlation function. This increases the precision of the correlation function even if the beam edge should be present. It also facilitates the determination of the shift for samples showing periodic structures (e.g., a cross-grating), where the CCF shows more than one maximum. Using the MCF with such samples will dampen the adverse effects of periodic features and thus improves the confidence of the shift detection. Since no disadvantages were observed when using the MCF over the CCF, the former is used as the default correlation function in TOM^2 .

Feature-Based

The correlation-based methods detect an image shift between a pair of micrographs assuming no rotation, mirroring, warping, skewing, or magnification changes between different micrographs. The shift is measured globally from different image features contributing to the correlation. When image rotations and magnification changes are present, one must sample different rotations and scaling factors to find the correct alignment of the images. Alternatively, a local correlation algorithm can be used. However, sampling or local correlation is computationally expensive and thus slows down the acquisition process, and is thus considered undesirable.

Feature-based methods such as the scale-invariant feature transform (SIFT) algorithm [Lowe, 2004] or its successor, speeded up [sic] robust features (SURF) [Bay *et al.*, 2008], do not use correlation methods. Instead, they extract unique descriptors (so called "key points") from the images and use these to match descriptor pairs from both images.

Matching can be done by various methods, such as euclidean distance [Lowe, 2004], random sample consensus (RANSAC) [Fischler and Bolles, 1981], or principal component analysis (PCA) [Ke and Sukthankar, 2004]. The detected key point pairs can then be used to calculate a transformation matrix that describes not only their displacement, but also the rotation, shift, scaling and mirroring between these images [Goshtasby, 1988]. Even warping and perspective transformation can be calculated using piecewise linear transformation if a sufficient amount of descriptor pairs have been matched [Goshtasby, 1986]. The time needed to compute the descriptors and match them is in the order of a few seconds for micrographs, e.g., of size 1024×1024 pixels. Larger micrographs can be binned to this size prior to processing, which results in a speed-up with no significant loss of precision. Figure 2.3.3 shows a sample keypoint detection of two low-dose micrographs acquired with the Titan Krios at different magnifications.

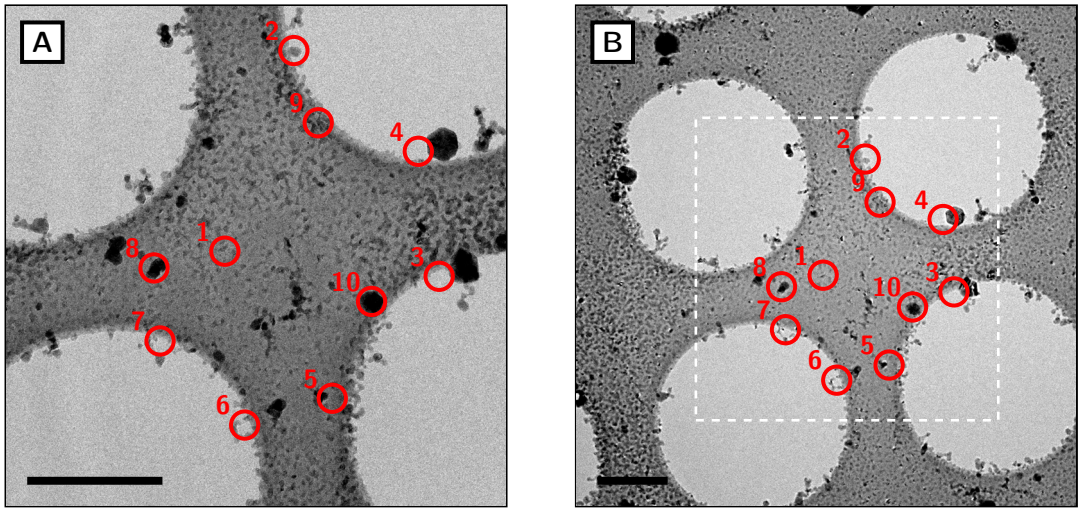

Figure 2.3.3: Example of key point detection using the SIFT algorithm for micrographs recorded at different magnifications. (A) Micrograph recorded at 11 000 × magnification. (B) Micrograph recorded at 6500 × magnification. The two micrographs showing a quantifoil grid recorded under low-dose conditions (exposure time $t_e = 0.2\,\mathrm{s}$, defocus $\Delta f = -4\,\mu\mathrm{m}$). Key point pairs are labeled with the same number in both micrographs. 18 key point pairs could be found satisfying the confidence criterion; for clarity, 10 key points are shown in the illustration. Note that all key points in micrograph (B) are distributed over the FOV (A) (white dashed rectangle). Scale bar is 1 µm in both images.

The SIFT algorithm is implemented in TOM^2 using the VLfeat library [Vedaldi and Fulkerson, 2008]. This image-registration method facilitates the comparison and registration of EM and light-microscopy maps for use in correlative microscopy applications.

Additionally, SIFT can be exploited for tracking purposes. The SIFT algorithm can even outperform correlation-based techniques, especially for samples where unique small features are present in a matrix of empty space, which shows up as noise in the correlation image and thus can aggravate peak detection. On the other hand, correlation-based techniques perform better on samples with few distinct unique features or extremely low contrast and low SNR.

Feature-based methods can also be used if the pair of micrographs were recorded under largely different tilt angles, for example used in tilt-pair reconstruction [Yoshioka *et al.*, 2007]. Perspective correction in combination with SIFT can be used to successfully match image pairs with different viewing angle [Morel and G.Yu, 2009], which will be explained in the following.

Perspective Correction

To detect an image shift between two images that were recorded at different tilt angles, one has to include distortions of features perpendicular to the tilt axis due to their different projection directions. Features that are not situated on the tilt axis are compressed with increasing tilt angle perpendicular to the tilt axis. This originates from the fact that the features will be projected from different viewing angles; the higher the tilt angle, the more predominant is this directional compression within the micrographs.

Comparing images taken at high tilt angles, e.g., more than 40°, even with a small difference in tilt angle of 5°, will result in large deviations and thus an unreliable detection of the image shift. Therefore, a perspective correction is necessary for accurate determination of the image shift. During correlation, TOM^2 stretches the template image along the direction of the tilt axis by a factor

$$f = \frac{\cos \alpha_t}{\cos \alpha_i} \tag{2.3.6}$$

where α_t and α_i are the specimen tilt angles of the template and image respectively [Guckenberger, 1982]. The image i_u is transformed into the stretched image i_c using

$$i_c = M_t \cdot M_r \cdot M_s \cdot M_r^{-1} \cdot M_t^{-1} \cdot i_u \tag{2.3.7}$$

where M_t is the translation matrix

$$M_t = \begin{pmatrix} 1 & 0 & 0 \\ 0 & 1 & 0 \\ \frac{-d}{2} & \frac{-d}{2} & 1 \end{pmatrix} \tag{2.3.8}$$

with d the size of the image. The rotation matrix M_r of the tilt axis rotation angle α_r is

$$M_r = \begin{pmatrix} \cos\alpha_r & -\sin\alpha_r & 0 \\ \sin\alpha_r & \cos\alpha_r & 0 \\ 0 & 0 & 1 \end{pmatrix}, \tag{2.3.9}$$

and the stretch matrix is

$$M_t = \begin{pmatrix} 1 & 0 & 0 \\ 0 & f & 0 \\ 0 & 0 & 1 \end{pmatrix}. \tag{2.3.10}$$

Using this correction, image pairs from different tilt angles can be compared and their shift can be determined. Even shift differences between a pair of micrographs recorded at 0° and 60° are still processed with reasonable accuracy (error below 50 nm for a magnification of 27 500 ×).

2.3.3 Coordinate System Transformation

Many high-level microscope operations such as mapping or centering of a feature require a translation of CCD coordinates into microscope coordinates. Microscope coordinate systems are defined by, e.g., the stage, the image shift or beam shift coordinate systems. They use different physical units and are rotated with respect to the CCD coordinate system. To transform a vector between two coordinate systems, the properties of both coordinate systems with respect to another need to be determined and calibrated. Calibrations are performed in a similar manner to methods described elsewhere [Koster *et al.*, 1992].

Stage and Image Shift to CCD Calibration

To transform a vector from CCD coordinates into stage coordinates the relation

$$\vec{v}_{CCD} = M \cdot \vec{v}_{stage} \tag{2.3.11}$$

is used. $\vec{v}_{CCD}$ and $\vec{v}_{stage}$ are 2×1 vectors in the respective coordinate systems, M is a 2×2 matrix whose elements need to be calibrated. Thus equation 2.3.11 can be expressed as

$$\begin{pmatrix} x_{CCD} \\ y_{CCD} \end{pmatrix} = \begin{pmatrix} a_1 & b_1 \\ a_2 & b_2 \end{pmatrix} \cdot \begin{pmatrix} x_{stage} \\ y_{stage} \end{pmatrix}. \tag{2.3.12}$$

To solve this system of linear equations a two step algorithm is used. In the first step only the stage x coordinate is changed an the resulting change in CCD coordinates is

measured. The coefficients a_1 and a_2 are determined from:

$$a_1 = \frac{x_{CCD}}{x_{stage}}, \qquad a_2 = \frac{y_{CCD}}{x_{stage}}. \tag{2.3.13}$$

The coefficients b_1 and b_2 are determined by measuring a stage y change and observing the image shift in the acquired images.

$$b_1 = \frac{x_{CCD}}{y_{stage}}, \qquad b_2 = \frac{y_{CCD}}{y_{stage}}. \tag{2.3.14}$$

Calibration has to be done at each magnification since vector length and rotations in the imaging might change between magnifications (see section 2.1.1). Figure 2.3.4 shows the images necessary to determine the essential coefficients of the transformation matrix.

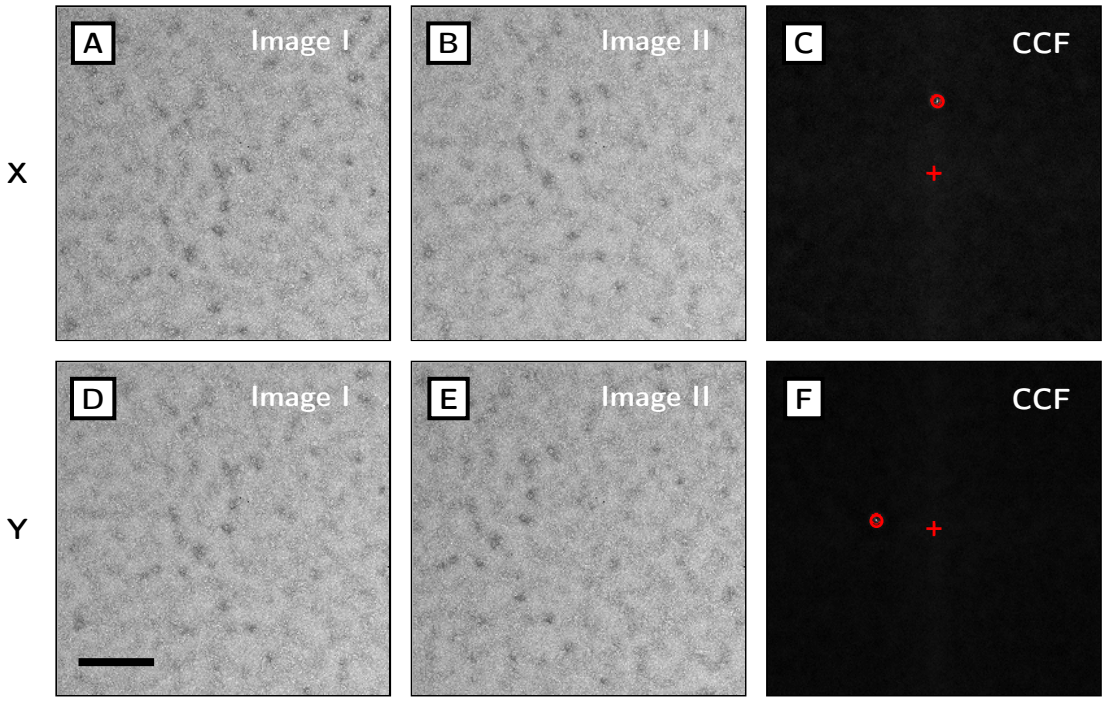

Figure 2.3.4: Stage coordinate system to CCD coordinate system calibration. A sample position is imaged before (A) and after (B) an induced stage shifted in x direction, the shift vector is determined from the CCF or MCF (C). The same procedure is performed using the y direction (D), (E) and (F). Both vectors should have the same length, however, due to imprecisions in the mechanics of the stage, the vector lengths can vary in both directions, but should display an angle of 90°. As long as the difference ratio of length between both vectors is constant for all movements, it does not hamper the correct calibration. Scale bar is 200 nm.

Once the transformation matrix M is determined, the vector in the stage coordinate

system can be calculated as

$$\vec{v}_{stage} = M^{-1} \cdot \vec{v}_{CCD} \tag{2.3.15}$$

where M^{-1} is the inverted transformation matrix M. The image shift to CCD calibration is done in a similar manner.

Image Beam Shift Calibration

When changing the image shift electron-optically, e.g., to center an image feature, the beam has to be re-centered as well (see section 2.1.4). Figure 2.3.5 illustrates the automated beam shift to CCD system calibration.

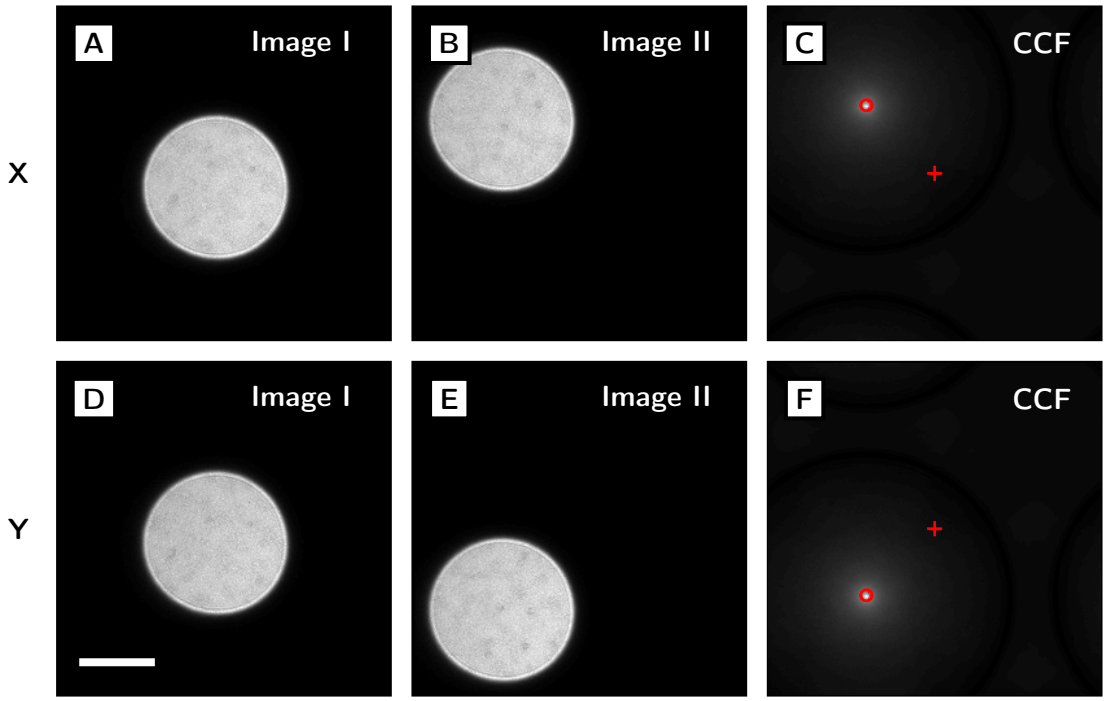

Figure 2.3.5: Beam shift coordinate system to CCD coordinate system calibration. The beam is condensed so that it is smaller than the FOV imaged, therefore it is possible to image the position of the beam while changing the beam shift coil settings. A beam position is imaged before (A) and after (B) an induced beam shift in x direction, the shift vector is determined from the CCF or MCF (C). The same procedure is performed using the y direction (D), (E) and (F). To avoid damage of the CCD sensor from overexposure, a very small exposure time is used and the beam is not fully condensed to a dot, but to a circle of size 0.3 FOV. CCF or MCF can be used to detect the position of the beam. Scale bar is 200 nm

To transform a vector from image-shift coordinates into beam-shift coordinates, the

following equation is used:

$$\vec{v}_{beam} = M_{ib} \cdot \vec{v}_{image}. \tag{2.3.16}$$

It is possible to apply the same algorithm as described in section 2.3.3, but measurement of the movement of the beam shift in relation to the image shift system cannot be performed by directly measuring shifts on the CCD detector. Therefore, the image-shift system and the beam-shift system are calibrated in relation to the CCD system.

The transformation matrix from the image shift into the beam shift system is defined as

$$M_{ib} = M_b^{-1} \cdot M_i \tag{2.3.17}$$

where M_b^{-1} is the inverted transformation matrix of the beam shift to CCD system and M_i is the transformation matrix of the image shift to CCD system.

2.3.4 Beam Size Calibration

The physical size of the electron beam is an important parameter during setup and acquisition. If the beam is too large, the dose in the FOV is too low and, furthermore, a large area will be exposed to electron radiation. If the beam is too small, the edge of the beam will be in the FOV; in addition, the CCD camera might be overexposed or even damaged. Commercial programs do not provide a parameter to adjust the beam size to a physically meaningful value; instead, the condenser C2 setting (intensity parameter) can be used to change the size of the beam (see section 2.1.2). The value of this "intensity" parameter is linear-dependent on the physical size of the beam as shown in figure 2.3.6. Thus, calibration for each spot size permits direct setting of the physical size of the beam in units of FOV.

Calibration of this linear relationship between beam size and intensity value is done by imaging the beam condensed to a medium-sized spot on the CCD detector. To provide a convenient way of determining the beam size for different microscope settings, the beam edge must be detected automatically. This is achieved by recording an image and applying the Canny edge detection algorithm [Canny, 1986] to find the beam edge in the image. The longest extracted edge is chosen as the most probable candidate for the beam edge and is used to fit a circle using a Gauss-Newton least squares algorithm [Gander *et al.*, 1994] (see figure 2.3.7). The normed residuals of the circle fit are

$$r_N = \frac{\sum_{n=1}^{M} \sqrt{x_c(n)^2 + y_c(n)^2} - \sqrt{x_f(n)^2 + y_f(n)^2}}{R_f}, \tag{2.3.18}$$

where x_c and y_c are the detected circle coordinate points and x_f and y_f are the fitted circle coordinate points, while R_f is the radius of the fitted circle. If the residuals are below a threshold value (0.3), the fit is accepted and the center and radius of the beam is calculated and plotted against the readout C2 "intensity" parameter value.

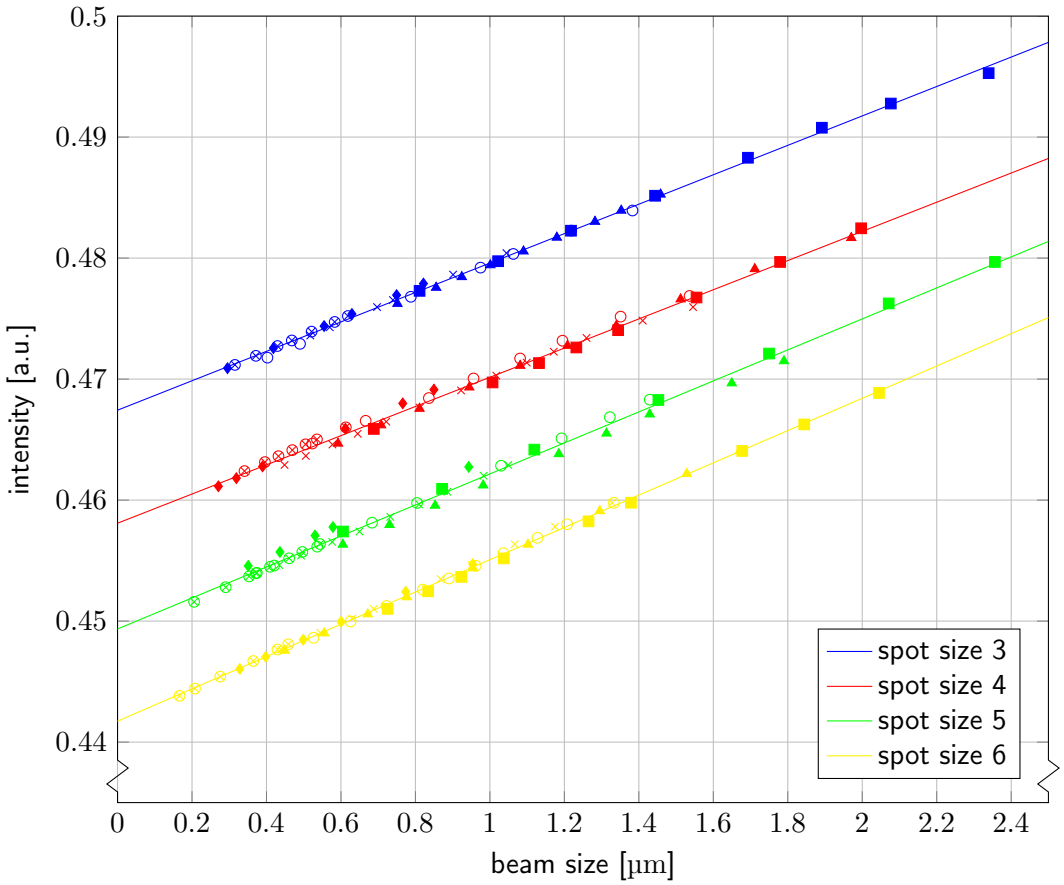

Figure 2.3.6: Beam Size versus intensity plot for different spot sizes and magnifications (Magnification at the fluorescence screen: 84 000 × (⊗), 68 000 × (⋄), 54 000 × (×), 36 000 × (○), 29 500 × (△), 24 500 × (□), acquired with FEI Tecnai F30 "Polara" microscope. The beam size has a linear relationship to the illumination settings, which are defined by C1 (condenser 1, spot size setting) and C2 (condenser 2, "intensity" setting). Different spot sizes result in different linear relations. Note that the same linear relationship between beam size and intensity holds true for different magnifications.

It is not necessary to have the beam exactly centered on the CCD camera. It is sufficient to image part of the beam, so that even calibrations of beam sizes larger than the FOV are possible. However, for precise beam fitting, more than one quarter of the beam edge should be visible; otherwise, the curvature of the beam is too low to reliably fit its size and center position.

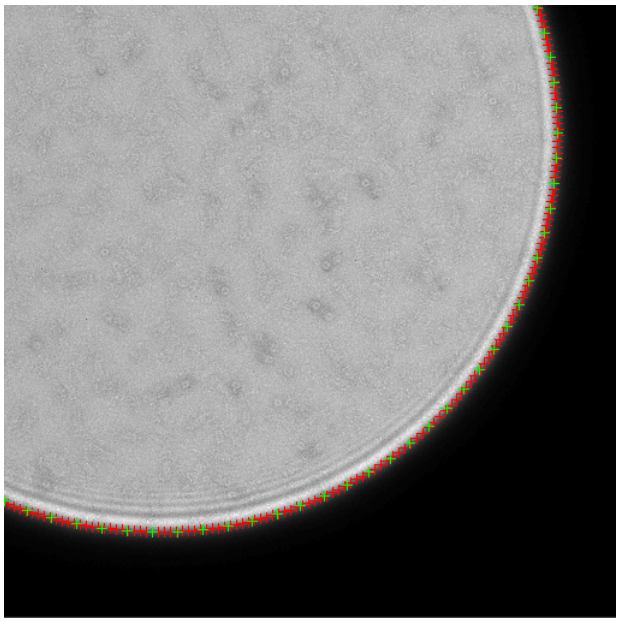

Figure 2.3.7: Example of automated beam detection. The edge of the electron beam is imaged on the CCD camera, the beam edge is extracted from the CCD image as a series of coordinate points (red markers) and a circle is fitted to these coordinate points (green markers) (see text for details). Once the beam edge is detected, this algorithm can also be used to center the beam on the detector (see section 2.3.5).

Once the beam size is calibrated for a certain magnification and spot size, the user can define the beam size in units of CCD FOV, so that a beam of size 1 FOV encloses exactly the CCD detector area if centered properly.

2.3.5 Automated Beam Centering

Centering of the electron beam on the CCD detector is critical to guarante homogeneous and constant illumination conditions during the acquisition of micrographs. It can be done manually using the beam shift coils; however, these coils are also accessible via the driver software of the microscope, enabling automation of the centering procedure. The edge of the beam can be detected using the same algorithm as described in the previous section, and as a bonus the center of the beam is determined. A flow diagram of the beam centering algorithm is depicted in figure 2.3.8.

The difference vector of center of the beam to the center of the CCD is calculated and transformed into beam shift coordinates. The resulting beam shift correction vector is applied. If the beam detection fails, the beam is shifted so ensure that some part of the beam edge is visible in the image. The procedure is then repeated until a beam edge is found. False beam-edge detection may lead to a positioning of the beam outside of the FOV. In this case, the illuminated area would be outside of the FOV, resulting in the recording of dark images. Therefore, to increase robustness and to ensure accurate beam centering, the algorithm tests if the beam is illuminating the FOV after centering. To test illumination, an additional image is acquired and the mean counts are calculated

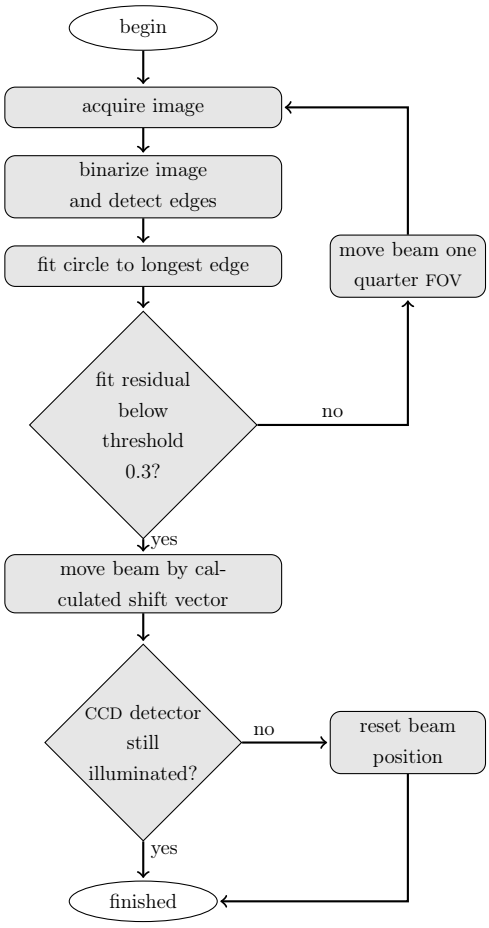

Figure 2.3.8: Flow diagram of beam centering algorithm. The fitting is repeated a maximum of four times with different beam positions in order to detect the beam edge. If no edge is detected and fitted to a circle successfully, the beam is reset to its original position to avoid false beam positioning.

and compared to the mean counts of the original micrograph. Only if the mean counts are in the same range the result is accepted, otherwise the beam is reset to its previous position. This safety check insures that the beam is not set to some false position where it cannot be recovered anymore.

2.3.6 Automated Alignment of Objective Lens Rotation Center

The center of rotation of the objective lens is an important parameter that needs to be adjusted carefully (see section 2.1.6). Misalignment of the rotation center leads to image shifts and off-axis rotations during focus changes. Thus, the autofocusing algorithm described in section 2.3.7 depends on the correct adjustment of the rotation center. The rotation center is adjusted by changing the beam tilt angles in x and y direction using the beam tilt coils.

Changing of the rotation center is possible via the microscope driver, and thus an automatic rotation center alignment routine can be created. The algorithm is based on

the idea introduced in Koster and de Ruijter [Koster and de Ruijter, 1992]. The aim is to set the rotation center in such a way that the measured image shift is minimized between two micrographs acquired at different defocus values. The rotation center consists of a set of two parameters in two directions x and y which create a coordinate system. To map this rotation center coordinate system to the CCD coordinate system a similar approach is used as described in section 2.3.3:

$$\vec{v}_{rc} = M_{rc}^{-1} \cdot \vec{v}_{CCD}. \tag{2.3.19}$$

Calibration of the transformation matrix

$$M_{rc} = \begin{pmatrix} a_1 & b_1 \\ a_2 & b_2 \end{pmatrix} \tag{2.3.20}$$

is done as follows: first a pair of micrographs with a set of defocus values d_1 and d_2 is acquired at one rotation center setting, and the resulting image shift vector is measured. Then, another pair of micrographs is recorded at a different rotation center setting resulting in a changed beam angle in direction x with resulting vector $\vec{r}_x$. From the difference vector $\vec{x}$ the elements a_1 and a_2 are determined using the x and y components of the vector $\vec{x}$.

$$a_1 = \frac{\vec{x}_x}{\vec{r}_x}, \qquad a_2 = \frac{\vec{x}_y}{\vec{r}_x}. \tag{2.3.21}$$

The coefficients b_1 and b_2 are determined using the analog procedure for a change of beam angle in direction y with resulting vector $\vec{r}_y$:

$$b_1 = \frac{\vec{y}_x}{\vec{r}_y}, \qquad b_2 = \frac{\vec{y}_y}{\vec{r}_y} \tag{2.3.22}$$

The auto rotation-center function records a set of micrographs at two defoci d_1 and d_2. Since the transformation matrix is independent of the absolute defocus [Koster and de Ruijter, 1992] the actual values of d_1 and d_2 can be arbitrary, only the difference $(d_1 - d_2)$ must be the same as used during the calibration. Typical values for $(d_1 - d_2)$ are 4 to 8 µm. Tuning is done iteratively to compensate for non-linearities in the rotation-center coordinate system. Typically, two iterations yield a rotation center alignment with an accuracy of 1 mrad in both directions.

2.3.7 Auto Focusing

The auto-focus algorithm is based on the well-established beam-tilt method [Koster *et al.*, 1989; Koster and de Ruijter, 1992]. This algorithm exploits the linear relationship

between defocus and the amount of beam-tilt-induced image shift between a pair of micrographs recorded with and without an additional beam tilt. Figure 2.3.9 shows the pre-calibration step to determine the zero-defocus position and the utilized calibration algorithm. To enable meaningful auto focusing, i.e., such that adjusted defocus values will correspond approximately to the "real defocus" of the recorded micrograph, the software needs a reference point. Typically, this reference point is the 0 µm defocus position (Gauss defocus). Manual adjustment of this reference point is limited in the accuracy and will vary depending on the skills of the user (typically off by 1 to 2 µm). Therefore, a pre-calibration step was added to the automation scheme to determine the 0 µm defocus position. Pre-calibration is done by asking the user to roughly focus the image and then scanning a defocus range for the exact zero defocus. At each position, the image shift is measured by acquiring a pair of micrographs using different beam tilts. The 0 µm defocus position is determined by interpolating the position where the image shift is 0.

After the zero defocus has been determined, the calibration routine starts. The auto focusing algorithm is depicted in figure 2.3.10. Calibration is done by acquiring a pair of micrographs, detecting the beam-tilt-induced image shift and relating that to the defocus of the image. The nominal defocus read from the microscope can be off by a few hundred nanometers from the true defocus of the image even after the precalibration procedure has been performed. To increase the accuracy of the auto focusing routine, one can utilize the well-known CTF-fitting procedure [Mallick *et al.*, 2005] which is implemented in TOM^2, provided that the Thon rings (visualization of the CTF [Thon, 1971]) are visible in the PSD. To see these Thon rings, the magnification of the micrograph needs to be high ($> 30\,000\times$). Additionally, the image contrast needs to be sufficient, this requires a carbon-containing sample imaged at high dose ($>50\,e^-/Å^2$) using a detector with an MTF that allows the recording of high frequencies. The defocus value is determined by locating the zero-crossings of the CTF. These zero-crossings are located between the Thon rings, therefore the defocus needs to be set in a range such that 3–5 Thon rings are visible in the PSD.

To further increase the accuracy of the auto focus on tilted specimens, Ziese et al propose a stretching of the images according to the defocus gradient [Ziese *et al.*, 2003]. However, the correction is less than 1 % for high magnifications which are normally used for cryo-electron tomography ($>20\,000\times$). Thus, implementation of this correction has been omitted.

The calibration routine depends on the correct setting of the rotation center (see section 2.3.6) and the eucentric height (see section 2.3.8), which has to be performed prior to running the auto focus calibration.

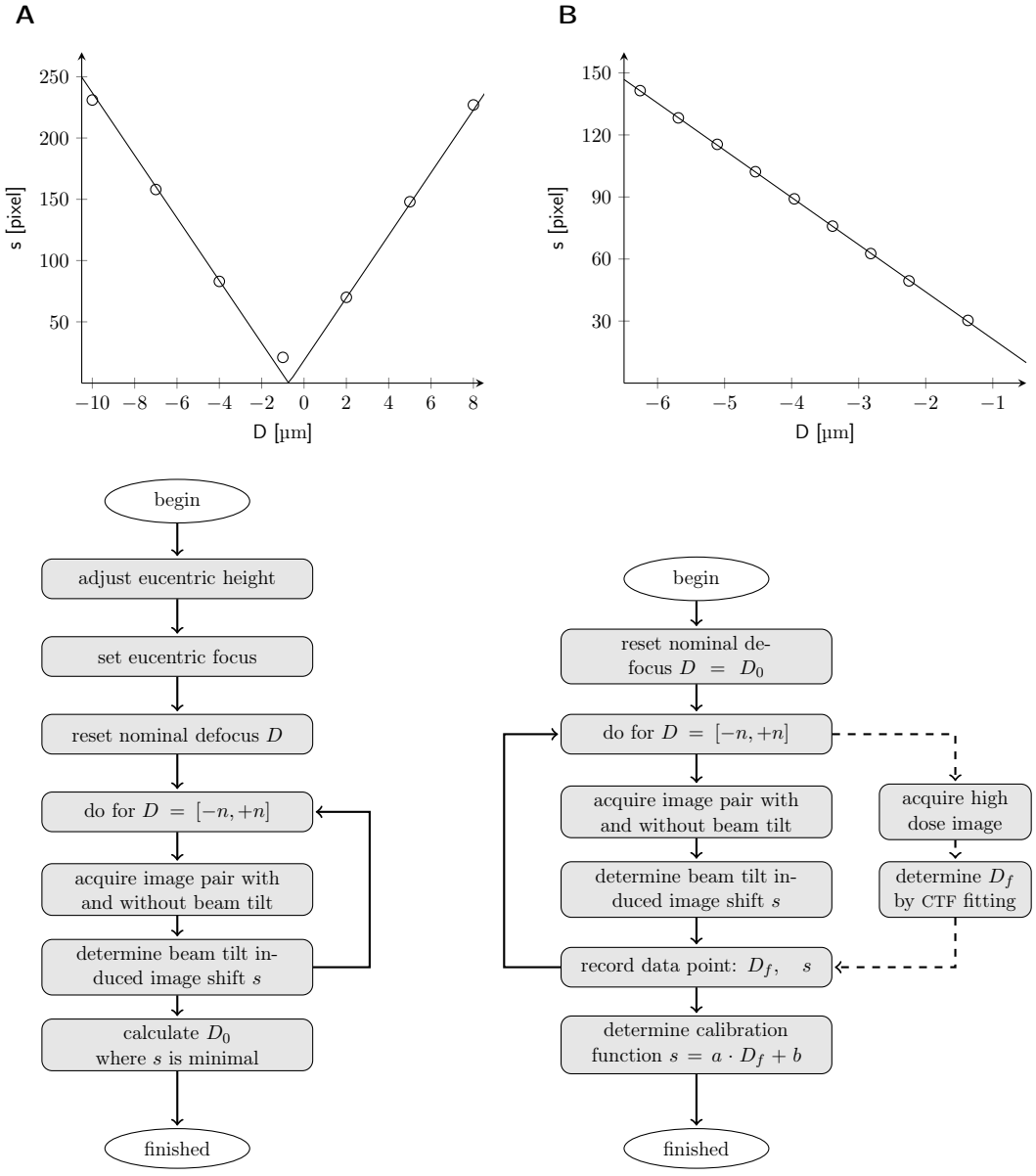

Figure 2.3.9: Auto-focusing calibration routine. The calibration is performed in two parts. (A) A pre-calibration to determine the 0 µm defocus position, (B) the main calibration algorithm based on the beam-tilt induced image-shift method. The calibration measures the image shift for various defocus values and generates a linear calibration function. If optional CTF fitting is enabled a high-dose image is recorded to determine the exact defocus for each image shift, otherwise, the nominal defocus is read from the microscope.

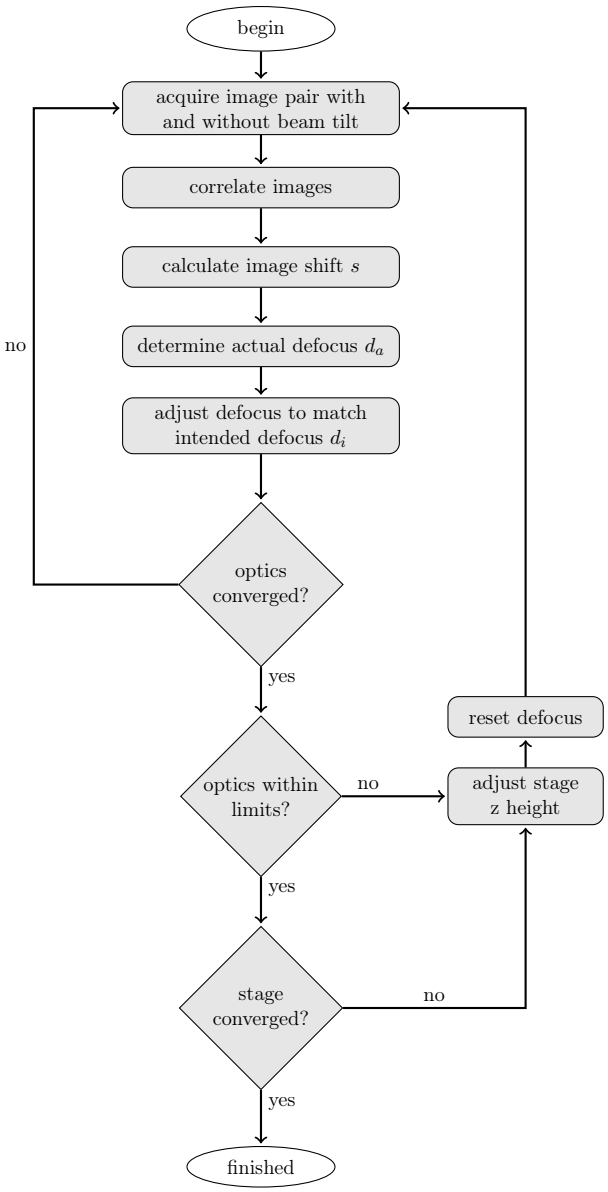

Figure 2.3.10: Flow diagram of the auto-focusing algorithm. A pair of micrographs is recorded at the current imaging settings with and without beam tilt (using the same amount of beam tilt as used for the calibration, usually 4 to 8 mrad depending on the magnification and utilized objective aperture). The actual defocus is determined by measuring the beam-tilt-induced image shift using the predetermined linear calibration function. The optics are changed to match the intended defocus (supplied by the user) and the procedure is repeated until the change of defocus converges. If the focus change is larger than a threshold value (supplied by the user; default 2 µm), the stage can be used to compensate for large changes.

When moving large distances, as for example done in single particle investigations, the focus changes can be large (in the range of 20 µm to 50 µm) due to the topology of the specimen grid [Nickell *et al.*, 2007a]. However, changing the defocus value by large amounts will cause a movement of the beam and might induce a loss of parallel illumination conditions. Therefore, large focus changes are accomplished by stage movement in z direction. This way one permits the electron optics to remain stable: within a fixed interval (typically -2 µm to 2 µm) the objective lens is used for focusing, while larger focus changes outside of this interval are compensated by stage height changes. This procedure is not applicable if the stage is additionally tilted because the stage has to stay in eucentric height to keep the same feature in the FOV while tilting.

2.3.8 Auto Eucentric Height

The eucentric height is the z-height stage position where the effect of tilting induces minimal changes to the x and y position of the sample. In other words, when the sample is at the eucentric height and the stage is tilted, the lateral sample movement is minimal. Therefore, for a successful tilt series experiment, the sample has to be placed at the position of its eucentric height.

Positioning at eucentric height can be done automatically using a similar algorithm to that described in section 2.3.7. The only difference to the auto-focus method is that instead of the beam tilt, a stage tilt is induced for eucentric height. For calibration, the stage-tilt-induced image shift is measured and a linear calibration function is determined relating the stage z-height to lateral movements. After calibration, the auto eucentric height function can be executed and will measure the image shift at the current stage z-height and change the z-height accordingly to match the eucentric height. To increase precision, this process is repeated iteratively until the sample is at the eucentric height.

If the sample is far away from eucentric height, the induced image shift can be quite large. Therefore, the magnification should be set to a low-to-medium value to increase the FOV in order to detect the image shift. Magnifications used for detecting z height offsets of up to 20 µm are in the range of 3000 × to 10 000 ×.

2.3.9 Auto Stigmation

For high-resolution TEM imaging it is important to periodically adjust the objective astigmatism of the image. This astigmatism is induced by misalignment of the objective aperture and residual contamination. Koster et al. describe a method to defocus and stigmate the image by tilting the beam and solving an overdetermined system of linear equations using a least-squares approach [Koster *et al.*, 1992]. This method is based

on the fact that astigmatism introduces a directional defocus variation. This defocus variation can be measured by tilting the beam in two perpendicular directions and determining the beam-tilt-induced image shift (analog to the auto-focusing procedure). However, this procedure is limited in accuracy and cannot stigmate the beam with high precision. The error of the directional defocus determination is in the range of 50 to 200 nm for magnifications between 50 000 × to 100 000 ×, and applied beam tilts of 4 to 8 mrad. Nevertheless, this method is computationally less demanding, easy to calibrate, and applicable even if the images have a low SNR, like in low-dose applications.

Astigmatism can also be observed in the PSD. With no astigmatism present, the Thon rings are perfectly circular. If astigmatism is introduced, the directional variation of defocus will bend them into ellipses. Hence, we have implemented an algorithm where the PSD of an image containing carbon is calculated, and the amount of astigmatism is determined by fitting ellipses to the Thon rings. The stigmator coil strength is then adjusted iteratively by changing the coil current of one of the four coils in a stepwise fashion. The decision of which coil needs to be adjusted is derived from a calibration step that measures the effect of each coil strength change in the direction of the ellipse principal axes. After changing the coil current another image is acquired and the process is repeated until the Thon rings are circular. This method has the advantage to be very precise compared to the beam-tilt method, usually less than 1 % astigmatism can be achieved within 5 to 10 iterations. However, this algorithm can only succeed if Thon rings are visible in the PSD; which is only the case if the SNR is high enough (typically the algorithm needs to be executed on images showing carbon support film). Furthermore, to see Thon rings the magnification needs larger than 100 000 ×, and the defocus needs to be larger than 1 µm. The larger the magnification, the smaller the defocus needs to be set in order to see the effect of objective astigmatism. For magnifications larger than 300 000 ×, defocus values of < 500 nm will suffice.

2.3.10 Energy Filter Tuning

The energy filter provides many tuning options to generate a distortion-free image on the detector. The vendor's software can be used for most tuning tasks such as tuning of achromaticity, isochromaticity, and correction of geometric distortions. These parameters are relatively stable over time so tuning is only required before the acquisition is started and can be still valid after days. However, one parameter of the energy filter that needs to be tuned more often is the position of the energy-selective aperture. The position of the zero-loss peak is directly related to the stability of the high-tension system of the utilized microscope. Thus, small changes in the electron-volt region will

result in a slight movement of the zero-loss peak. An additional movement can be caused by large defocus changes, therefore the energy-selective aperture of the energy filter needs to be readjusted after larger defocus changes ($> 5\,\mu m$) caused by auto focusing. For zero-loss imaging, typically an energy-selective slit of 20 to 30 eV is used, thus movements of the zero-loss peak make a re-centering of this aperture mandatory. The algorithm implemented in TOM^2 acquires energy-filtered images and measures the mean counts while scanning a range of energy-selective aperture positions (up to $\pm$ 100 eV. If illumination has been found, the program samples various energy-selective aperture positions distributed around the detected position ($\pm$ 30 eV), constructing a relation between energy-selective aperture positions and image counts. Figure 2.3.11 depicts the algorithm and resulting data for the energy-selective aperture position centering.

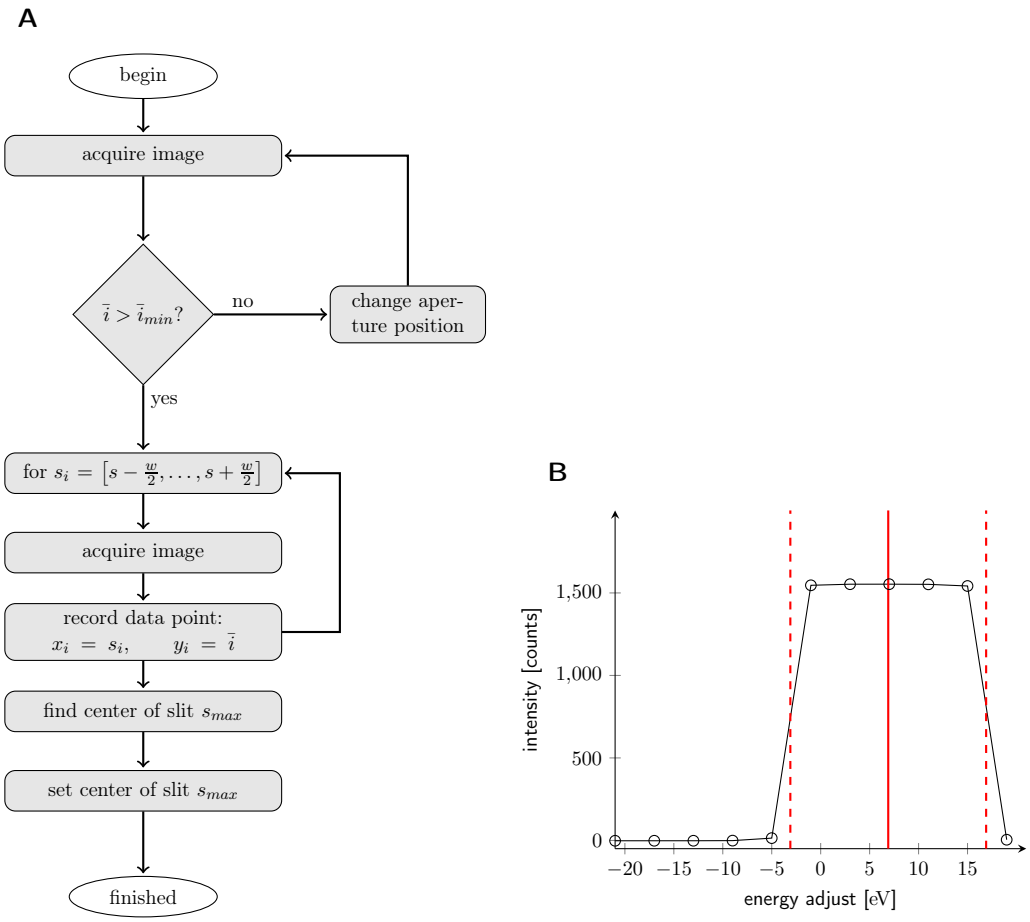

Figure 2.3.11: Centering of the energy-selective aperture position. (A) The centering algorithm consists of two parts. The first part searches for ilumination by acquiring multiple images using different energy-selective aperture positions and comparing the mean counts of these images $\bar{i}$ to a minimal count value $\bar{i}_{min}$. If the counts are too low the position of the slit is changed and the procedure is repeated until an image with mean counts larger than $\bar{i}_{min}$ is found. In the second part the software scans a range of energies (w is the aperture width) by adjusting the aperture position and acquiring images around the previously found position. (B) The mean counts of these images are recorded. The black circles denote mean count values of the different images, the solid red line marks the center of the slit position (6.9 eV), the dashed red lines mark the edges of the energy-selective aperture (20 eV).

2.3.11 Electron Dose Calculation

Radiation damage to the sample is one of the main limiting factors in EM of frozen-hydrated specimens. For low-dose applications the dose on the sample needs to be kept below empirical thresholds; e.g., a total dose of $100\,\mathrm{e}^-/\mathrm{Å}^2$ is an upper limit for tomography of frozen-hydrated specimens [Frank, 1992]. Therefore, it is important to have a dose estimate for the given imaging conditions. The dose is typically defined as the absorption of one Joule of ionizing radiation by one kilogram of matter ($1\,\mathrm{Gy} = 1\,\mathrm{m}^2{\cdot}\mathrm{s}^{-2}$). In electron microscopy, the dose is defined as the deposited energy per area and its unit is $\mathrm{e}^-/\mathrm{Å}^2$. TOM[2] offers the possibility of calibrating and estimating the dose that will be used during the recording of a micrograph. The dose is dependent on the illumination conditions, beam current, exposure time, and illuminated area. Thus, a calibration has to account for beam size, spot size, and exposure time. Calibration is performed by acquiring an image without a sample and measuring the mean counts. A calibration factor is calculated using

$$F = \frac{\bar{i} \cdot \pi r_b^2}{f_c \cdot t_e \cdot s^2} \tag{2.3.23}$$

where $\bar{i}$ are the mean counts of the image, πr_b^2 is the area of the beam with beam radius r_b, f_c is the conversion factor of the CCD camera, s is the object pixel size, and t_e is the exposure time of the micrograph. The calibration factor F indicates how many electrons pass the sample per area and per exposure time and is normalized with respect to the size of the electron beam. The conversion factor of the camera states how many counts will be generated for every electron that reaches the detector (as described in section 1.2). It can be determined using a Faraday cup [Ishizuka, 1993]. To estimate the conversion factor without a Faraday cup, one can measure the electrical current with the fluorescence screen of the microscope (provided that the fluorescence screen has been calibrated properly)

$$f_c = \frac{\bar{i} \cdot \pi r_b^2}{s^2 \cdot t_e \cdot C \cdot I_s}, \tag{2.3.24}$$

where I_s is the electrical current measured at the fluorescence screen and C is the Coulomb constant ($6.242 \times 10^{18}\,\mathrm{e}^-$). For the acquisition setup one can manually define an intended dose which should then be used for the recording of a micrograph, and the software will calculate the necessary exposure time

$$t_e = \frac{d \cdot \pi r_b^2}{F} \tag{2.3.25}$$

where d is the intended dose. Alternatively, the dose can be calculated for a given exposure time.

2.4 Construction of a Specimen Map

In order to qualitatively asses the specimen, identify, and select areas for acquisition, it is important to have an overview of the entire specimen. The lowest magnification that can be set on an electron microscope (typically $\approx 200\times$, object pixel size of ≈ 50 to 200 nm, depending on the post-magnification and binning factor of the detector) will only show a small part of the grid (typically an area of $80 \times 80\,\mu m$), due to the limited detector size. Therefore it is necessary to acquire a number of image tiles at different stage positions and construct a map of the entire grid from these image tiles (or at least the central region that is accessible by the stage). Typically a range of $\pm$ 700 µm is covered by this method, yielding a FOV of $\approx 1.5\,mm^2$.

The mapping algorithm acquires images as tiles which are set up in a regular $n \times m$ matrix of stage coordinates (usually a 10×10 map is used to cover the central area of the specimen at a magnification of $280\times$). At each coordinate, a micrograph is acquired and saved to a pre-specified directory on the hard drive. Additionally, the location of the image tile and its covered area are stored in a database using the R*-tree format [Guttman, 1984; Beckmann *et al.*, 1990]. To construct an image of the entire grid from the individual image tiles, the stage position of each tile is converted into the CCD coordinate system (see section 2.3.3). The image tiles are then placed in a larger image according to their CCD coordinate, forming the overview image. On microscopes equipped with a FEI AutoLoader, up to twelve specimens can be mapped consecutively in an unsupervised fashion, and all maps can later be qualitatively assessed quickly.

Once the recording of the map is completed, the user can view the map in the GUI depicted in figure 2.4.1. For closer inspection of details in the map, the view can be zoomed and re-centered arbitrarily. The GUI mimics the behavior of the Google Earth software (Google Inc., Mountain View, CA, USA). A map generated from 10×10 image tiles of 2048×2048 pixels will allocate approximately 640 MB storage. To speed up the interactive handling of the map, only the data from currently visible tiles are loaded. Furthermore, the tiles are resampled to the resolution of the viewing screen in order to further reduce the amount of data. This makes real-time navigation possible, zooming into the map will dynamically reveal more details of a small area of the grid, as more pixels from the relevant image tiles are displayed.

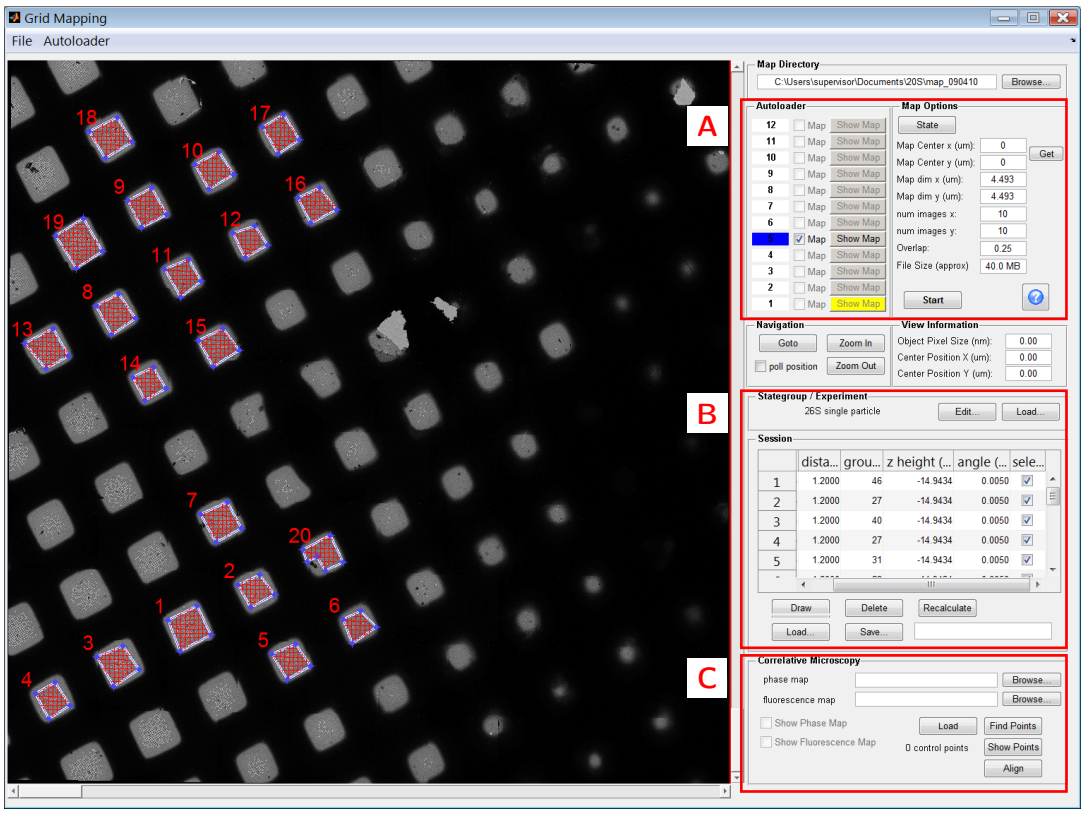

Figure 2.4.1: GUI for generating a map of a specimen grid. (A) The map can be zoomed and repositioned arbitrarily, areas can be selected for later acquisition (blue polygons with red crosses, see section 2.6.1 for details). Using the FEI AutoLoader, up to twelve grids can be mapped consecutively. (B) The generated maps can be used to navigate to certain specimen positions for a later in-depth investigation at higher magnification. (C) Additionally, a cryo-fluorescent map of the grid can be loaded and registered to the TEM map (see section 2.6.4).

2.5 Organization of the Acquisition Scheme

The acquisition process for applications such as tomography and single-particle investigations can be generalized by dividing the complete process into smaller subprocesses and then partitioning these into even smaller tasks. We analyzed different acquisition schemes (single-particle acquisition, tomography, batch tomography, random-conical tilt acquisition, etc.) and developed a model of a general acquisition scheme with four levels of hierarchy. Figure 2.5.1 illustrates the hierarchical ordering of the acquisition objects.

In an acquisition scheme, usually multiple sample positions are imaged. For tomography applications, the stage has to be tilted at each position to acquire 2-D projections of the same sample at different tilt angles. For single-particle applications, usually only one projection or a focal series of several sample positions is recorded without tilting the stage. However, at each tilt angle or specimen position, a number of preparation steps are executed before the recording of one or multiple micrographs.

The object representing the lowest level of hierarchy is called the *state*. A state represents one set of microscope parameters such as spot size, magnification, defocus, and CCD exposure time. Any number of states can exist in an acquisition scheme; typically, three to twenty states are needed. The role of each state is defined by an "action" which will be executed during the acquisition. This action is linked with an auto function, such as auto focus, auto eucentric height, center beam, or the acquisition of a micrograph. When auto functions are executed to adjust microscope parameters, the other states in the acquisition scheme need to be updated with the values of the changed parameters. For example, when the auto focusing algorithm adjusts the defocus value by a certain amount, the acquisition states need to shift their defocus values by the same amount to record a micrograph with the new defocus value. Changes in the microscope parameters need to be calculated differentially from the previously tuned parameters, e.g., if the focus changes by 1 µm, all states need to change their focus value by 1 µm. Thus, to propagate parameter adjustments, a messaging system between states has been implemented; auto functions can generate a notification event that will be received by event handles of the respective states.

The next level in this hierarchy is the *state group*. The state group links a number of states into a logical order, so that more complex tasks can be automated, e.g., adjusting the eucentric height, auto focusing, followed by the acquisition of a micrograph. In a state group, usually some preparation states (such as auto functions described in 2.3) will precede one or more states that acquire a micrograph. Low-dose acquisition schemes require that the preparation states are located in a position close, but different than, the acquisition position. Therefore, each state in a state group is given a specific location

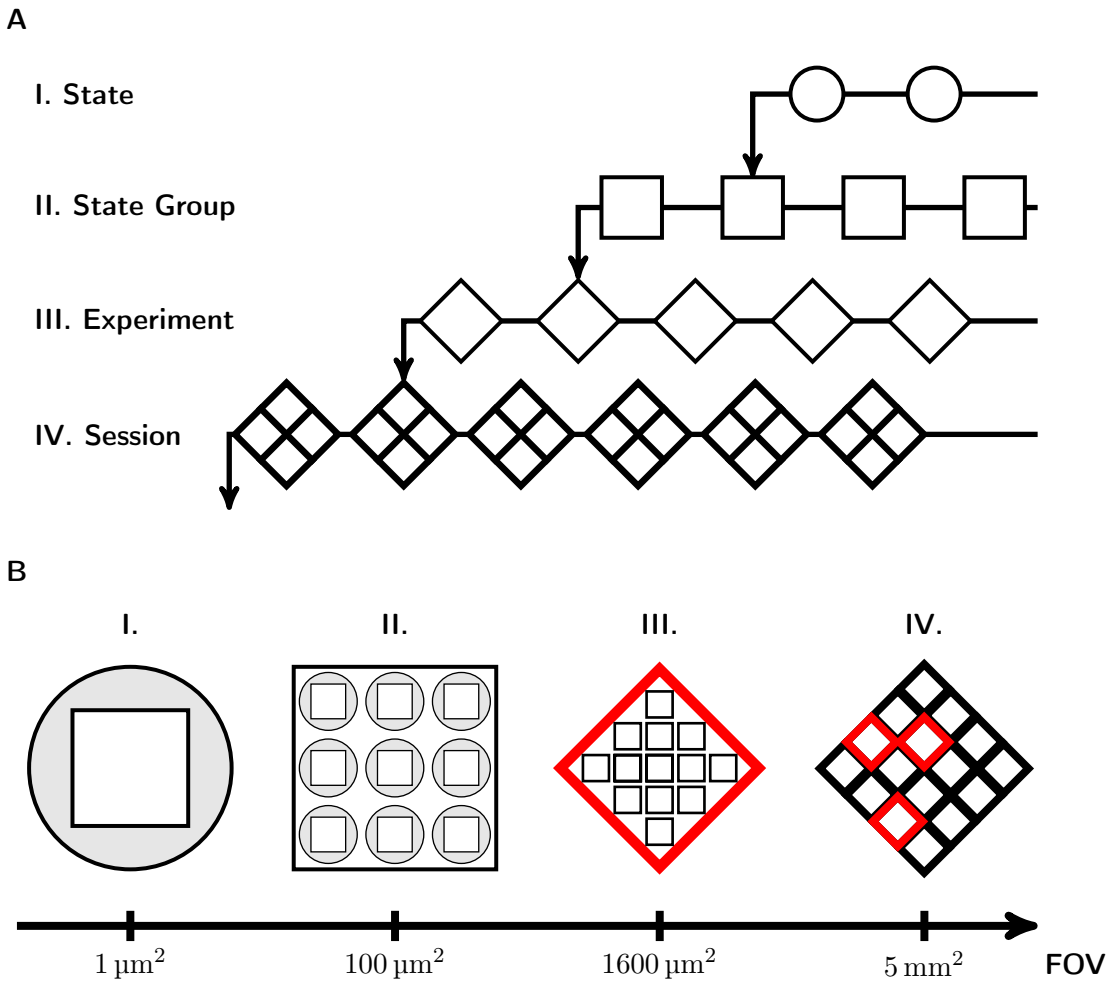

Figure 2.5.1: Illustration of hierarchical acquisition scheme. (A) The acquisition scheme can be represented as a tree of elements. (I) The state represents a set of microscope parameters (e.g., magnification, spot size, defocus, etc.) with an "action" (e.g., acquire, auto focus, tracking, etc.) (II) The state group defines a low-dose acquisition layout using the image beam shift system to place the individual states. (III) The experiment places state groups at various tilt angles or lateral specimen positions for acquisition of a tilt series or a single-particle set of micrographs. (IV) The session bundles experiments and executes them sequentially, a session can span over multiple grids using the FEI "AutoLoader". (B) Representation of the individual elements of the acquisition scheme from small to large FOV. (I) A state, represented as a detector FOV with illuminated area. (II) s state group, represented as a set of nine states at adjacent positions, (III) an experiment, represented as a set of state groups positioned to cover the area of a grid mesh, (IV) a session, represented as a set of experiments covering multiple areas in different grid meshes.

that will be set using the image beam shift system (see also figures 2.6.1 and 2.6.3 for illustrations of state groups for single-particle acquisition and tomography applications). Using the optics system to switch between state positions (instead of using the stage) allows high-precision movements and minimizes waiting times between single recordings. However, the image beam shift system can only be used for movements in a range of $\pm$ 10 µm (see also section 2.1.4), which limits the lateral extent of the area accessible within a state group to 400 µm^2. Such large areas are in principle not needed, since state groups can be bundled in an experiment object (see below).

During the automated acquisition, a larger area or different locations of the specimen are typically used. To change the sample position to a different specimen area, stage movements are needed which can cover a range of $\pm$ 1000 µm. To execute a complete state group at different stage positions, an object called *experiment* is defined. The experiment object moves the stage to assigned sets of x,y,z, and α-tilt coordinates and then executes the state group. Sample positions can be defined manually as a set of coordinates. However, during single-particle acquisition, typically a larger area (e.g., one grid mesh) is imaged in a regular fashion. I.e., the stage coordinates can be generated by defining a regular $n \times m$ grid with one center x, y coordinate. Additionally, a set of regularly spaced coordinates can be generated inside a user-supplied polygon area, that defines, e.g., one specimen grid mesh.

Since not all states in a state group may need to be executed at each sample position, the experiment also defines a "firing table", which specifies which state in the state group should be executed at the current set of stage coordinates.

The highest level in an acquisition scheme is called the *session*. This element bundles experiment objects, placed on one or more sample grids, into one object. The session moves to the first set of coordinates defined in each experiment object. However, due to mechanical imprecisions caused by the stage, the feature of interest that was centered when the experiment coordinates were defined, might not be exactly centered when the stage coordinates are recalled. To re-center the feature of interest in an automated fashion, a user provided image, recorded at medium magnification, can be used as a template for to correct for eventual lateral displacements. A session can be interactively defined with an overview map of the whole grid. The map is recorded and visualized as described in the previous section 2.4.

2.6 Acquisition Schemes

2.6.1 Single-Particle Acquisition

The design of an acquisition scheme follows a "bottom-up" approach starting at defined states for adjusting microscope parameters and states for recording micrographs. The states are then combined into a state group, and their relative positions are defined. Afterwards, an overview map of the specimen is created and experiments are built by placing polygonal regions on the map that are automatically filled with positions where a state group should be executed. Finally, the experiments are bundled into a session which is then saved to a file. This file contains the entire acquisition scheme and can be loaded into the "experiment player" GUI, which allows to execute the acquisition scheme in an automated and unsupervised fashion.

The first step in the design process is the definition of a state group comprising multiple states. For single particle acquisition, the state group design can vary greatly in the number of acquisition states, mostly depending on the type of specimen grid used (different carbon support films, e.g., QuantiFoil, lacey carbon film).

The state group contains one or more states to record micrographs, preceded by states that tune the microscope optics to compensate for potential changes in electron optics, changes in sample position, etc. Figure 2.6.1 illustrates a state group for single-particle acquisition. Since the acquisition is unsupervised, it is not guaranteed that after changing the sample position this new position is suitable for acquisition. For example, the new location might have been placed on an area where the sample is too thick or the metal support of the grid is in the FOV blocking the beam. In this case, the current position should be dismissed and the stage should be moved to the next position. Therefore, the first state in the state group evaluates the specimen thickness and electron transparency at the current position. This is done by recording and evaluating a micrograph: the position is excluded if the mean counts of this micrograph are outside a predefined range. In this case, the remaining parts of the state group are not executed and the next position is evaluated immediately.

Between different sample locations, the sample z height and thus the focus of the image can change notably. As previously mentioned, this is due to the heterogeneous sample topology, where changes of up to 100 µm can occur (see section 2.3.7). Therefore, auto focusing is mandatory and has to be done at each sample position prior to image acquisition. However, changing the defocus by adjusting the objective lens will result in beam movements, especially if changes larger than 10 µm have to be compensated. An off-centered beam will additionally introduce astigmatism (since the position of the

objective aperture is aligned in respect to the beam), and thus large changes should be therefore avoided. The software provides additionally the possibility to compensate large z-height changes by first adjusting the z-height position followed by a refinement step using the objective lens system.

Although microscope optical stability over time has improved with nowadays available instruments, the optical alignment will still deteriorate over long periods of time (typically several hours). However, for the acquisition in single-particle analysis, a very high and constant image quality is mandatory, and thus the alignment of the microscope has to be periodically tuned during the acquisition. For example, the beam center, rotation center, astigmatism and energy filter slit position have to be readjusted using appropriate auto functions. Once all tuning states have been completed successfully, the micrograph(s) can be recorded.

In order to generate a high-resolution 3-D model of the protein complex from the data set, micrographs with different defoci are typically acquired. By combining "particles" that were recorded using various defocus values, the frequency gaps in the individual images (caused by oscillations of the CTF) can be filled with the information obtained from other images (the phase shift induced by defocus changes will position the gaps at different frequencies) after flipping the CTF so that all frequencies have a positive algebraic sign ("phase-flipping") and no destructive interference can occur by mixing frequencies with positive and negative algebraic sign (see figure 2.1.5), resulting in a more even frequency distribution in the 3-D model [Schiske, 1968; 2002]. This method is only applicable if the CTF can be determined by a fit to the Thon rings in the PSD, which is usually the case for commonly-used magnification and dose. Typically, individual micrographs are recorded with different optical parameters (for example 8 micrographs per sample position using 8 different defocus values, see figure 2.6.1).

As stated above, the state group defines how the acquisition should be executed at one sample position. In single-particle investigations, a large number of micrographs are needed; depending on the particle distribution, up to several tens of thousands of images (see section 1.5). These micrographs are collected from one or more specimen grids by placing many (hundreds or thousands) state groups at different sample positions. Typically, the user defines these positions by identifying suitable areas of the specimen and placing experiment objects containing up to a hundred state groups in these areas (see previous section 2.5). To quantitatively asses a whole specimen grid, a map of the specimen grid is generated ("mapping"). Then, areas suitable for acquisition (containing a thin continuous ice layer with evenly distributed protein complexes) are selected by the user and the state group positions are automatically calculated to cover the entire area (see figure 2.6.2). If the microscope is equipped with an automatic specimen grid

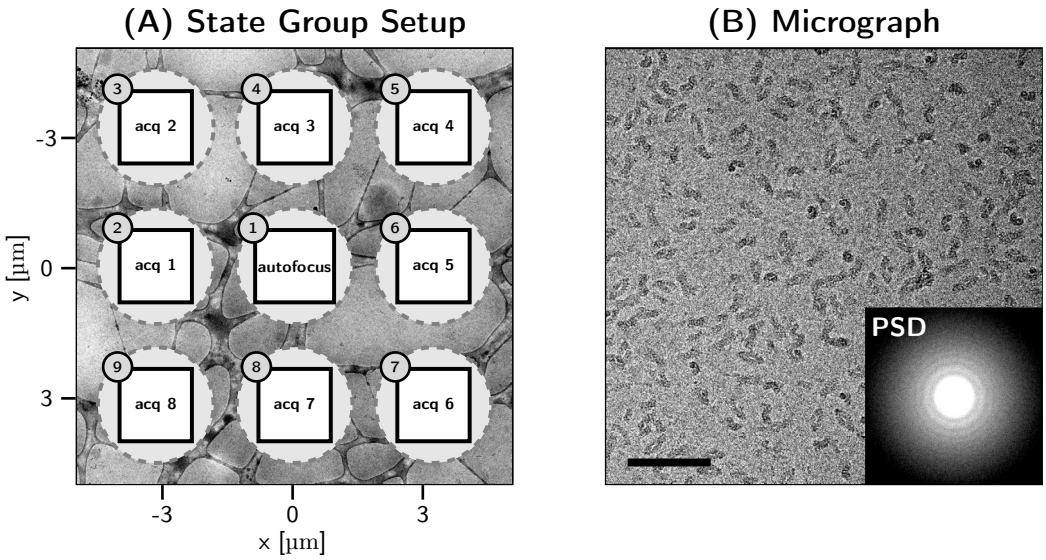

Figure 2.6.1: (a) State group for single-particle acquisition. The CCD area of each state is depicted as a square, the radius of the electron beam is shown as a dashed circle. States are executed in order of their numbering (1–9). At the center of the state group (image beam shift position (0,0)), the sample location is checked for suitable ice thickness, then the auto focusing algorithm is executed to adjust the z height of the stage and the excitation of the objective lens (respectively the focus settings). After successful completion of these preparation steps, eight micrographs are recorded. (b) Example Micrograph acquired using the acquisition scheme (object pixel size 2 Å, dose 30 $e^-/Å^2$). Inset depicts the PSD; Thon rings are visible and can be used for CTF fitting. Scale bar is 150 nm. See section 3.2.1 for details.

exchange system such as the AutoLoader, one can automatically map up to 12 grids and place experiments on all grids. The sample exchange after successful acquisition will then take place automatically.

Depending on the electron microscope used, the automated acquisition setup described is able to record micrographs over days. The acquisition speed is mainly dependent on the readout speed of the detector and the time needed to stabilize the stage after navigating to a new sample position to obtain "drift-free" micrographs. Table 2.6.1 gives an overview of the acquisition speed and required user interaction at different microscopes.

Once this acquisition scheme has been defined it can be executed in a fully automated and unsupervised fashion, the only manual task that the operator has to perform is the refill of cryogens. This has to be done every 24 h in the case of a Tecnai F30 "Polara". The Titan Krios has an automated refilling system, so only the nitrogen supply needs to be exchanged after approximately seven days.

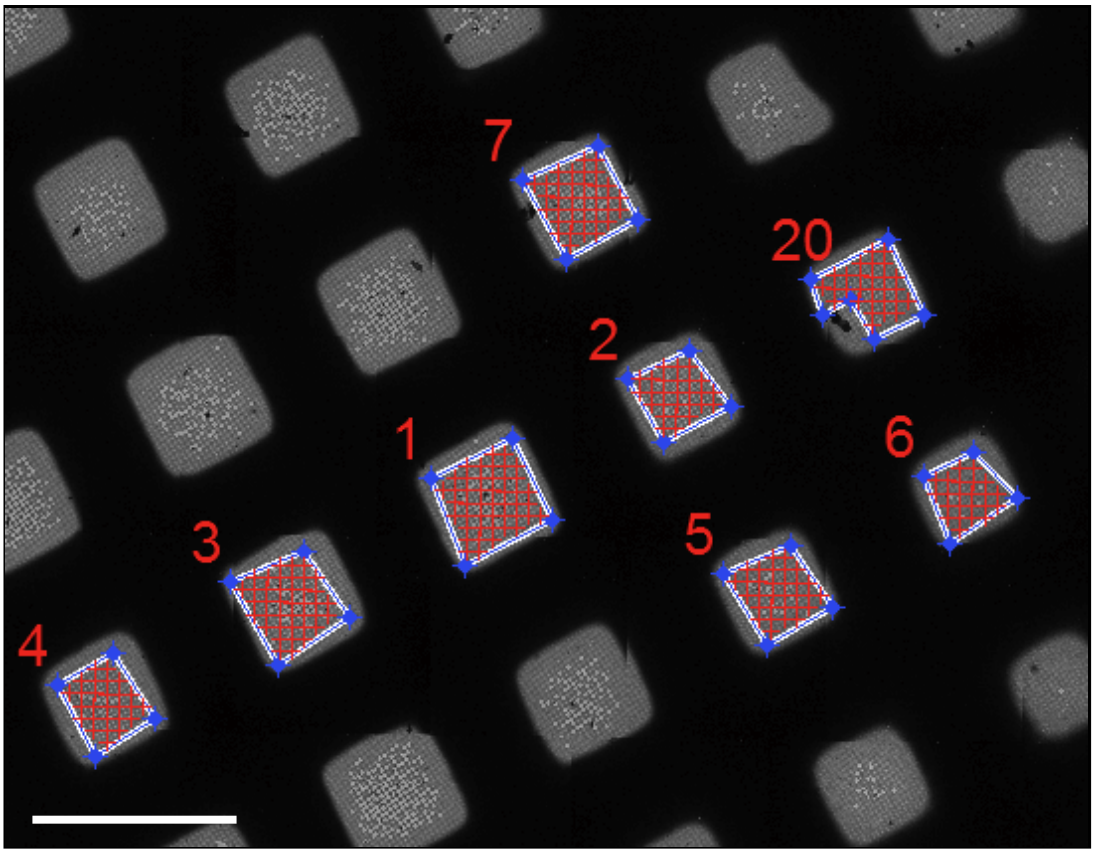

Figure 2.6.2: Selection of specimen areas suitable for single-particle acquisition. The user selects regions suitable for acquisition by placing a polygon area (blue) on the map of the specimen; the software then fills these areas with positions (red crosses) to execute state groups. A typical grid mesh of size 80 × 80 µm can contain up to 400 recording states. Positions are calculated to cover the entire user-defined area inside of the polygon by placing coordinates in a regular fashion inside of the area defined by the polygon. The distance between coordinates is defined by the size of the state group and a user-defined distance factor. All state groups of one polygon area are combined into an experiment object; all experiment objects are saved in a session file for starting the acquisition. Scale bar is 200 µm.

Table 2.6.1: Single-particle acquisition speed and required user interaction at different electron microscopes

	Tecnai F20 Eagle, side entry	Polara Gatan USC4000	Titan Krios TVIPS FC816
detector readout speed[1]	11 s	15 s	6 s
stage settling time	120 s	40 s	30 s
optics settling time[2]	10 s	10 s	5 s
nitrogen refill every	4 h	24 h	automated
micrographs per day	2000	2300	2600

2.6.2 Tomography

Design of this acquisition scheme follows similar concepts as the already introduced acquisition scheme for single particle investigations. Additionally to the optics tuning and acquisition states, there is one new tuning step: During sample tilting, the feature of interest can move out of the field of view. This phenomenon is based on the mechanical inaccuracies of the stage, which will result in an imperfect eucentric height and instabilities (drift, displacement) during tilting (see section 2.1.3). The first problem is solved by executing an auto eucentric height routine before the first start of each tilt series. The second issue is solved by defining an additional tracking state along the tilt axis adjacent to the acquisition position. This tracking state uses the image from the previous tilt angle as a template for subsequent correlation and allows the re-centering of the feature in the field of view.

Figure 2.6.3 shows a state group for the acquisition of a tilt series. The tracking and focus positions are adjacent to the acquisition position. They must be placed exactly on the tilt axis to ensure adjustments at the same specimen height during tilting. If the focus state is not located on the tilt axis, the change in z height will cause an additional focus offset. If the tracking state is not correctly aligned to the tilt axis, the tracking will succeed but the sample position will "swing" out of the field of view perpendicular to the tilt axis during acquisition. This "swinging" will move the feature of interest and

[1] 4096×4096 pixels, binning 1
[2] after changing the image beam shift position

might result in a loss of that specific feature at higher tilt angles.

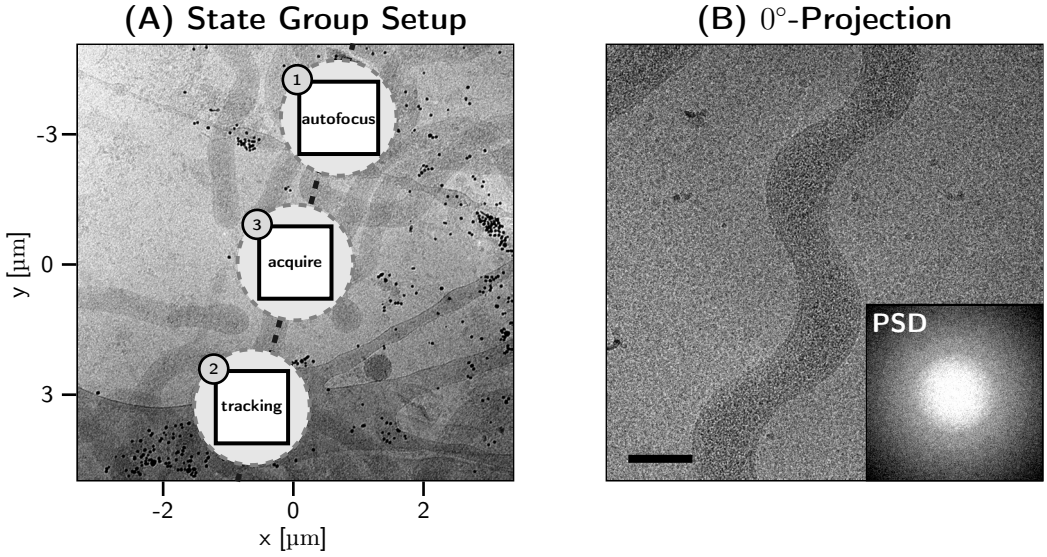

Figure 2.6.3: (A) State group for tomography. The CCD area of each state is depicted as a square, the radius of the electron beam is shown as a dashed circle. States are executed in order of their numbering (1–3). In a typical acquisition scheme, firstly the auto focusing algorithms compensates for z height changes of the sample after tilting, then the feature of interest is re-centered using the image from the previous tilt angle as a template for correlation, followed by the recording of a projection of the feature of interest. (B) 0° projection (object pixel size 4.67 Å, dose $2\,e^-/Å^2$) with PSD (inset). No Thon rings are visible in the PSD, making CTF determination and correction not applicable. Scale bar is 150 nm. See section 3.2.2 for details.

For the reconstruction of the tomogram, only areas that are present in micrographs of all projection angles are used. This described movement is thus lowering the obtainable size of the obtainable tomographic volume. Consequentially, movement should be minimized by determining the tilt axis angle with high precision. For the Tecnai F30 "Polara" microscope, a rough tilt-axis orientation angle can be obtained by measuring the direction of the holder y axis (see section 2.3.3). The resulting axis angle can be determined to approximately 1° precision. An error in tilt axis orientation of this magnitude will result in movements of the feature of interest that are larger than one quarter of the FOV at a magnification of 25 000 × (see figure 2.6.4). To determine the tilt-axis orientation with higher precision, a test tilt series should be acquired and aligned. Accurate numbers for the tilt-axis orientation (error $< 0.1°$) can minimize movements to below 5 % FOV. Experiments have shown a strong dependency of the movements to the distance of the tracking and acquisition state (see figure 2.6.4). Therefore, the distance

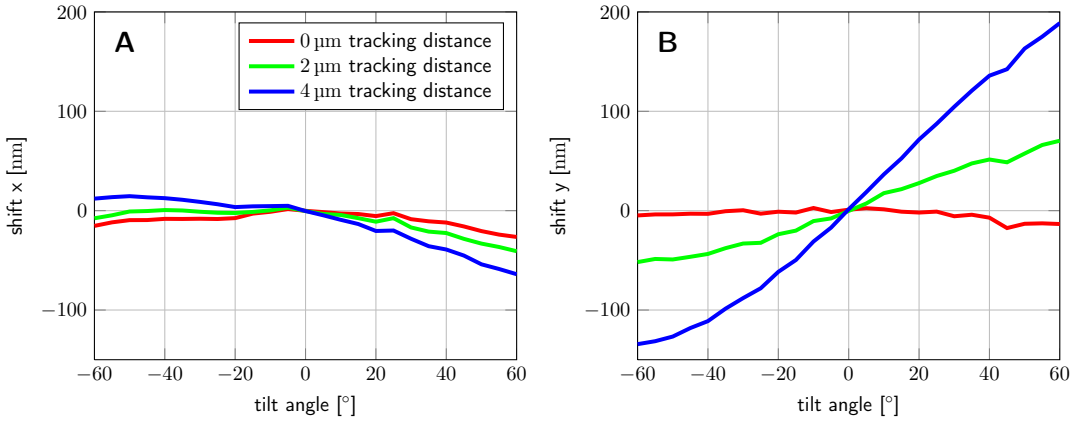

Figure 2.6.4: Measurement of the tracking error of a tilt series in relation to the distance between the tracking and acquisition state. A tilt series was acquired using the FEI Tecnai F30 "Polara" (tilt range $0° \rightarrow 60° \rightarrow 0° \rightarrow -60°$, tilt increment 5°, object pixel size 8.24 Å). The tracking and focusing was done at the image beam shift position (0 µm, 0 µm). Three acquisition states were placed on the tilt axis with distances of 0 µm, 2 µm, and 4 µm from the tracking state. 1 FOV corresponds to 845 nm. The tilt series of the three acquisition areas were aligned and reconstructed using the TOM toolbox. The tilt axis is aligned to the x-direction of the projections. The plots show the shifts of the projections of each tilt series relative to each other. (A) Note that the shift in the x-direction along the tilt axis remains almost constant. (B) With increasing distance of the acquisition to the tracking state, the shift increases significantly for the y-direction, which is perpendicular to the tilt axis.

between these states should be minimized as much as possible.

The experiment object is used to define a tilting scheme at a fixed stage x-y position, in contrast to single particle acquisition where the tilt angle is constant (typically 0°) while the x-y position changes. Since the experiment object's positioning system is fully flexible, any hybrid combination of stage lateral movement and tilting is feasible. On a Tecnai F30 "Polara" G2 equipped with a Gatan Imaging Filter (GIF) and a 2k Gatan CCD camera (pixel size 30 µm), acquisition of one tilt series (tilt range −60° to 60°, 2° increment) takes 60 min using tracking and focusing at all tilt angles ("full-tracking/full-focusing" scheme). This acquisition time can be reduced by omitting focusing and tracking steps at lower tilt angles, where deviations are rather small compared to tilt angles above 40°. However, this depends on the reproducibility of the holder movements and the hardware performance. In theory, it is possible to determine the movements of the holder in all 3 dimensions during a tilt series once and use this calibration data to completely avoid successive tracking and focusing steps ("pre-calibration" scheme). Pre-calibration is dependent on the stage position and additionally deteriorates over time, due to the

mechanical wear-down of the stage parts. The so obtained tracking vectors will show large variances, and thus it is not really advisable to pre-calibrate the stage behavior, as described in section 3.2.2.

2.6.3 Batch Tomography

The acquisition scheme described in section 2.6.2 records one tilt series at a specified sample position. After recording is complete, user interaction is required to search for the next sample position. The tilt-series acquisition is fully automated, requiring no user interaction, thus it is desirable to additionally automate this manual navigating step. Multiple tilt series experiments can be summarized into a session which incorporates different sample positions. The different sample positions are defined in the grid map analog to the setup of a single-particle acquisition (see figure 2.6.5).

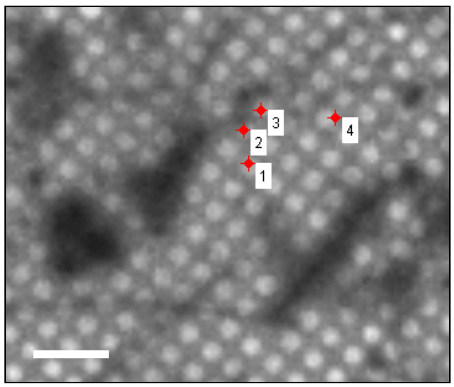

Figure 2.6.5: Placement of sample positions for batch tomography. User-defined sample positions (red crosses) are placed on the grid map, at each position a template image is recorded for later re-centering. Scale bar is 25 nm.

During setup, the user centers the features of interest and the corresponding stage coordinates are saved. However, the movement of the stage over larger distances is not reproducible, as mentioned before. This is caused by inaccuracies in the mechanics ("backlash") and leads to an off-centered feature of interest when the stage is moved to the saved coordinates after being moved elsewhere. To compensate this effect, the software needs to re-center stage position upon arrival at new stage coordinates, so that the feature of interest will be in the center of the FOV before a tilt series acquisition.

For re-centering, a reference image can be recorded at a lower intermediate magnification, which will show the selected feature. This reference image is later used to exactly center the feature using either a cross-correlation or SIFT algorithm.

After the intended feature has been re-centered, the eucentric height of the specimen is adjusted using the auto eucentric height function at a medium magnification of 3000 × to 5000 ×. After these preparation steps are completed successfully, the magnification for tilt series acquisition is set (typically 20 000 × to 100 000 ×). This magnifi-

cation change causes hysteresis effects in the lenses, thus the beam will be off-centered and needs to be re-adjusted using the automated beam centering algorithm (see section 2.3.5). Furthermore the energy-selective aperture position of the energy filter needs to be re-centered using the automated algorithm (see section 2.3.10). After completion of all these preparation steps, the tilt series acquisition is started.

Using the described acquisition scheme, it is possible to acquire up to 25 tilt series (tilt range $-60°$ to $60°$, $2°$ increment) per day on a Tecnai F30 "Polara" microscope without user supervision.

2.6.4 Correlative Microscopy

The low magnification TEM map of a vitreous sample grid shows low contrast and has low resolution, and is generally not suited for detection and identification of cells possessing a certain phenotype. Correlative cryo-fluorescence microscopy can be used to expedite the search and identification of low-copy-number features as target positions and greatly facilitate the setup of tomography sessions. TOM^2 includes the possibility to load correlative cryo-fluorescence microscopy maps in addition to the acquired TEM maps.

To generate such a light microscopic map of the specimen, the grid is imaged using a light microscope (LM) and a specially designed cryo-stage, which keeps the specimen at liquid-nitrogen temperature [Sartori *et al.*, 2007; Plitzko *et al.*, 2009; Rigort *et al.*, 2010]. Using a similar approach as described previously, the map is obtained by acquiring image tiles at different stage positions and then building a large image showing the whole grid. For each image tile, a phase-contrast image and a fluorescence-signal image are recorded. The phase-contrast image is used to determine the orientation of the map in respect to the TEM map. The fluorescence-signal map shows the signal of the labeled specimen features that are of interest for TEM imaging and will be superimposed (see following).

After acquisition of the LM map, the specimen is inserted into the TEM and another map is acquired as described in 2.4. The LM map needs to be registered with the TEM map and then transformed into the same coordinate system to enable an overlay (see figure 2.4.1 C). Maps can be scaled, rotated, shifted and mirrored with respect to each other. Furthermore, the contrast of a frozen-hydrated specimen in a light microscope is formed by a phase shift of the photons interacting with the sample (phase contrast), whereas the contrast formation mechanism of an electron microscope in LM mode (with switched-off objective lens) is based on absorption contrast. Therefore the maps will show similar but not identical features, e.g., cells in the TEM will be black, whereas in the light microscope they will be transparent and only visible by phase contrast of their

outer membrane.

Simple cross correlation approaches to register the maps are unreliable and computationally intensive, since all rotations, mirroring and scaling parameters need to be sampled in order to find the correct orientation of the map. Instead, SIFT (see section 2.3.2) is used to detect key points in both maps and subsequently match these key points into pairs so that each point pair denotes one common feature in both maps. The advantage of SIFT is that key points can be detected and matched regardless of differences between maps in SNR, scaling, shift, rotation, and contrast. To provide the algorithm with unique features that are identifiable in both maps, TEM finder-grids containing letters and numbers are used. However, the fluorescence maps have a lower point resolution due to the lower magnification, and key points cannot be identified with pixel-accuracy due to the different contrast formation mechanisms between both types of maps. Furthermore, spatial aberrations of the LM objective will cause distortions in the LM map. Therefore, the overlay can only give a direction where features of interest are located on the TEM grid. Typical errors of superposition are in the range of 1 to 2 µm. Nevertheless this technique greatly facilitates the search for tomography positions on the grid when searching for rare events in the specimen. For example, to identify cells with a certain phenotype that have been labeled with a fluorescent dye, the overlay can provide a rough orientation aid for the user to locate these cells among others which do not exhibit this phenotype.

To increase the the point resolution of the light-microscopic map, an objective with a higher magnification is required. Due to the design of the cryo-stage, the objectives used need to have a long working distance of at least 2.1 mm (numerical aperture (NA) of 0.75). To use an objective with higher magnification, the working distance would need to be reduced or an objective with a higher NA (≥ 1) would be required. However, the specimen needs to be handled at liquid-nitrogen temperature during mapping, making it impossible to reduce the working distance without redesigning the stage. Also, high-NA objectives are typically oil-immersion objectives, which cannot be used at liquid-nitrogen temperature. Another source for imprecisions of the light microscopy map is the imprecise movement of the stage of the light microscope. This leads to lateral distortions in the map, since the image tiles of the map do not fit perfectly. A more precise stage would be needed to minimize these distortions.

Specimen handling is a challenging task in cryo-fluorescence microscopy. The fragile specimen grid needs to be imaged in two different microscopes (LM and TEM), therefore, it needs to be inserted into the LM, removed, transferred and inserted into the TEM. During LM imaging, the specimen is in contact with air, causing contamination of the specimen grid due to frost particle formation on the specimen surface.

In summary, for certain investigations of samples showing rare events, correlative microscopy can be a helpful tool to detect these rare events on the grid for subsequent tilt series acquisition.

3 Results & Discussion

3.1 Benchmark of the Titan Krios Prototype

The 26S proteasome complex is a multimeric assembly with a mass of approximately 2.5 MDa that is involved in the main degradation pathway (the ubiquitin-proteasome pathway) of eukaryotic cells. Unlike constitutively active proteases, the 26S proteasome has the capacity to degrade almost every protein, yet acting with high specificity. The key stratagem is self-compartmentalization: the active sites of the proteolytic machine are sequestered from the cellular environment in the interior of the barrel-shaped 20S proteasome [Baumeister *et al.*, 1998]. Proteins destined for degradation are marked by ubiquitin, a degradation signal that is recognized by the regulatory 19S complexes that associate with the core 20S proteasome (core particle) to form the holoenzyme (26S proteasome) (see figure 3.1.1). The 20S proteasome, which is highly conserved from archaea to higher eukaryotes, was amenable to structure determination by x-ray crystallography [Löwe *et al.*, 1995; Groll *et al.*, 1997; Unno *et al.*, 2002]. In contrast, the 26S proteasome complex was to date not successfully crystallized.

The structural investigation of large macromolecular complexes such as the 26S proteasome using EM single-particle approaches are an alternative approach to crystallization. The medium resolution (10 – 20 Å) structures afforded by cryo-EM provide a base for hybrid approaches and functional studies of macromolecular assemblies [Robinson *et al.*, 2007]. The 26S proteasome is a complex enzyme assembly, it is composited of more than 30 different subunits [Voges *et al.*, 1999]. Furthermore, its composition is variable, and the protein particles are fragile and tend to disassociate, making specimen preparations difficult [Nickell *et al.*, 2009]. Reconstruction techniques, that yield a 3-D model of the complex from projections of "single-particles" recorded by cryo-EM need to take its variability into account. Instead of combining all projections into one 3-D model, multiple models representing multiple conformations of the complex need to be generated in order to obtain high-resolution structures of 10 Å or less of these individual conformations.

The resolution of a 3D model is dependent on the number of particles contributing to the average (see section 1.5) and the performance of the detector (see section 1.2). Therefore, many projections ($> 1\,000\,000$) of the protein complex are required. To obtain

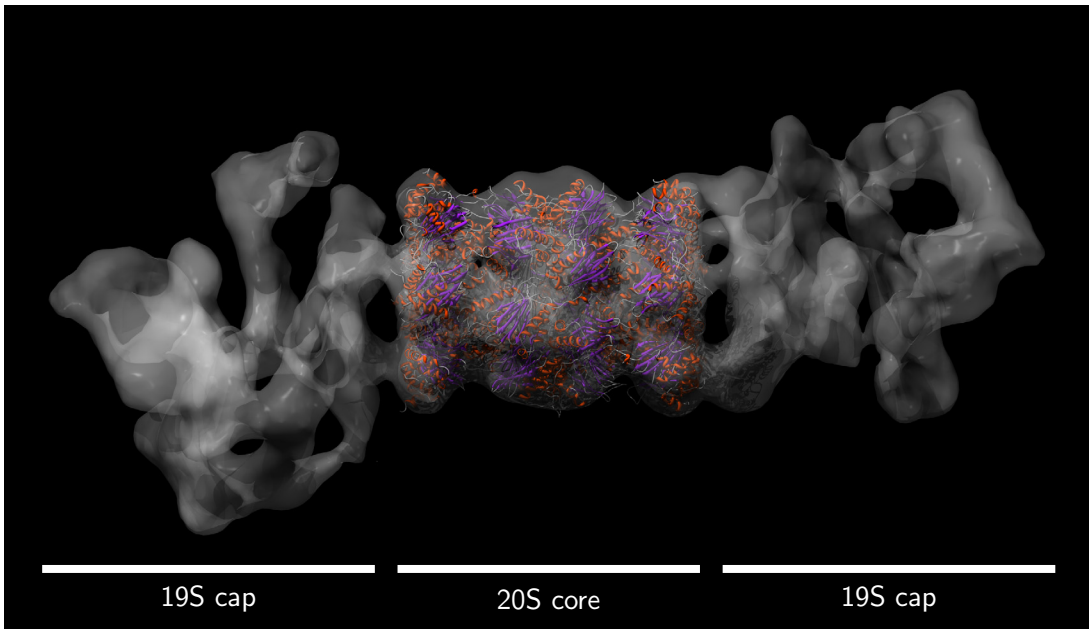

Figure 3.1.1: 3-D model of *Drosophila melanogaster* 26S proteasome. The 26S proteasome complex consists of a 20S core complex and two 19S regulatory complexes (caps). The structure of the 20S core complex has been obtained by x-ray crystallography [Löwe *et al.*, 1995] and has been fitted into the model using USCF Chimera [Pettersen *et al.*, 2004; Goddard *et al.*, 2007]. The structure of the 19S caps is still under investigation; it is not easily obtainable by crystallographic methods because of the lability of the complex. The lenght of the holocomplex is 45 nm.

this number of projections, a large number of micrographs need to be acquired (several 10 000) under controlled illumination conditions. Therefore, automated data acquisition is mandatory, and TOM^2 was developed to be utilized for this task.

The automated acquisition of a data set of this size is time consuming. To expedite this process, the electron microscope being used needs to be designed for high-throughput purposes by minimizing maintenance requirements. As shown in section 3.2.1 and [Nickell *et al.*, 2009], the Tecnai F30 "Polara" series microscopes are capable of imaging large macromolecular complexes to a resolution of 20 Å to 25 Å. To further increase the capabilities of single-particle investigations, a new microscope generation, the Titan Krios, was developed.

The Titan Krios is the direct sucessor of the Tecnai F30 "Polara" microscope which was especially designed for automated high-throughput acquisition. It features a redesigned optical system that provides a more stable electron beam during investigations than the Tecnai series microscopes (see section 2.1). It is equipped with an automated sample loading device, called the "AutoLoader", which is able to store and load up to twelve

frozen-hydrated specimens. The newly designed holder is capable of rotating the grid inside of the column for support of dual-axis tomography applications. The automated nitrogen refilling system keeps the system at liquid nitrogen temperature during days of acquisition so that no user interaction is required while an acquisition is running.

The prototype of this instrument was installed at the Max Planck Institute in September 2007. Additionally the prototype Tietz FC816 camera was installed at the microscope, this was the first camera with a 8192×8192 pixel CMOS detector with an increased sensitivity and readout speed over conventional CCD detectors (see section 1.2). The area of this detector is comparable to negative plates ($8k \times 10k$).

We tested the performance of this new microscope in comparison with the Tecnai F30 "Polara" microscope. In the following, a benchmark test is described and the results of this test are presented and compared to the Tecnai Series microscopes.

First, we tested the settling time of the stage after stage movements. A fast settling time is essential for high-throughput acquisition to acquire "drift-free" micrographs without extended delays during acquisition to maximize the number of micrographs per day.

Second, we investigated the contamination buildup during acquisition which limits the time, a specimen can be kept in the column and used for recording data. Acquisition of a large data set of tens of thousands of micrographs typically takes 10–14 days. The longer a specimen can be used for acquisition, the less specimens in total are required.

Third, we acquired a data set to assess the overal microscope performance. The 20S proteasome complex from *Thermoplasma acidophilum* [Seemüller *et al.*, 1995] was chosen to test the acquisition performance of the Titan Krios microscope. The proteasome offers several advantages for fast and reliable assessment of the performance of the microscope. Firstly, the complex is highly rigid and stable, so purification of the complex, sample preparation, and image processing routines do not need to entangle multiple conformations. Secondly, the crystal structure of the complex is known [Löwe *et al.*, 1995], so the model can be compared and validated to a high-resolution structure. Finally, the 20S proteasome from *T. acidophilum* shows a 14-fold symmetry, this fact can be exploited during model reconstruction to gain a high-resolution model of the complex without the need to acquire millions of particles because each projection can be used 14 times in the generation of the final 3-D model.

3.1.1 Auto Focusing Accuracy

The knowledge about the focus of an electron micrograph is essential to permit an accurate analysis. This is equally true for single-particle investigations as for tomography.

In both cases, variations in the focus values will decrease the resolution of the final reconstruction, or, in the worst case, will render their use for post-processing meaningless. Therefore, the accuracy of the auto focusing function is an important parameter, which directly influences the quality of the subsequent image analysis. During post-acquisition image processing the exact defocus of the micrographs is determined and used to deconvolve the effect of the CTF (see section 2.6.1). To combine micrographs with different defocus values and balance the frequency distribution in the final reconstruction, precise defocus values are needed, with variations less than 500 nm.

The deviations of the defocus values from the intended defocus in the acquired micrographs can be described using a probability density function (PDF) of a continuous random variable (in this case the defocus value). The PDF of the defocus values is a function that describes the relative likelihood for the defocus to occur in a range of possible defocus values. The integral of the PDF is set to be 1. In other words, the PDF measures the distribution of the defocus values around the intended defocus settings. The focusing error is given as the standard deviation (full width at half maximum) of this distribution. The smaller the distribution width is, the more accurate was the adjustment via the auto focusing routine.

For testing the auto focus routine, the Titan Krios TEM equipped with a FC816 CMOS camera (8192 × 8192 pixel detector) was used. The auto focus was calibrated at 300 kV using a beam tilt of 4 mrad and a negatively stained specimen of of 26S proteasome complexes at a given magnification with an object pixel size of 1.76 Å. The CTF fitting step during calibration (see section 2.3.7) was enabled to maximize calibration accuracy.

To determine the accuracy of the auto focusing routine on a negatively stained grid, 144 micrographs were recorded at different grid positions after auto focusing with an intended defocus of $\Delta f_i = -2\,\mu m$ at the acquisition position (so no image beam shift was applied). To compensate for sample z height differences, the stage was repositioned (see section 2.3.7). The defocus values Δf_e of the acquired micrographs were determined by calculating the PSD of each micrograph and fitting a CTF. The PDF of the determined defocus values was then calculated and the resulting distribution was fitted to a Gaussian function (figure 3.1.2 (A)). The PDF has a mean defocus $\Delta f_m = -1.99\,\mu m$, standard deviation $\sigma = 56\,nm$. This value can be considered the precision of the auto focusing routine under optimal conditions (high SNR, no change in sample position between focusing and acquisition), which is in good agreement with theoretical calculations [Koster and de Ruijter, 1992].

Usually, the auto focus position is located not directly at the sample position, but instead adjacent to the acquisition position to minimize exposure of the electron beam to the sample and control the dose. Due to the heterogeneity of the grid's surface struc-

ture, the auto focus position can slightly vary in z height (compared to the acquisition position). This will cause slight, but unwanted, defocus variations in the acquired micrographs. To assess this deviation, an acquisition scheme described in section 2.6.1 was used (see figure 2.6.1), the auto focus area was placed in the center of 8 acquisition positions with a distance of 2.5 µm. Maintaining the same acquisition parameters to scenario 1 (see above), 159 micrographs were recorded (figure 3.1.2 (B)). The PDF has a mean defocus $\Delta f_m = -1.97\,\mu\text{m}$, standard deviation $\sigma = 208\,\text{nm}$. This shows that using a focus position that is adjacent to the acquisition position increases the standard deviation due to the change in z height at different sample positions. However the precision of the auto focusing routine is still sufficient to use the acquired micrographs for post-processing.

For vitrified specimens, the SNR of the recorded images is substantially lower. This reduces the precision of auto focusing, because the image shift caused by the beam tilting (see section 2.3.7) cannot be determined with an accuracy of 1 pixel in the recorded micrograph due to the broadening of the correlation peak. We have used ice-embedded 26S proteasome complexes deposited on a QuantiFoil EM grid and imaged them according to the previously described protocol. 155 micrographs were recorded and analyzed (figure 3.1.2 (C)). The PDF has a mean defocus value of $\Delta f_m = -1.90\,\mu\text{m}$, standard deviation $\sigma = 201\,\text{nm}$. This shows that the auto focusing routine performs equally well on negatively stained and vitrified specimens with no significant loss of precision.

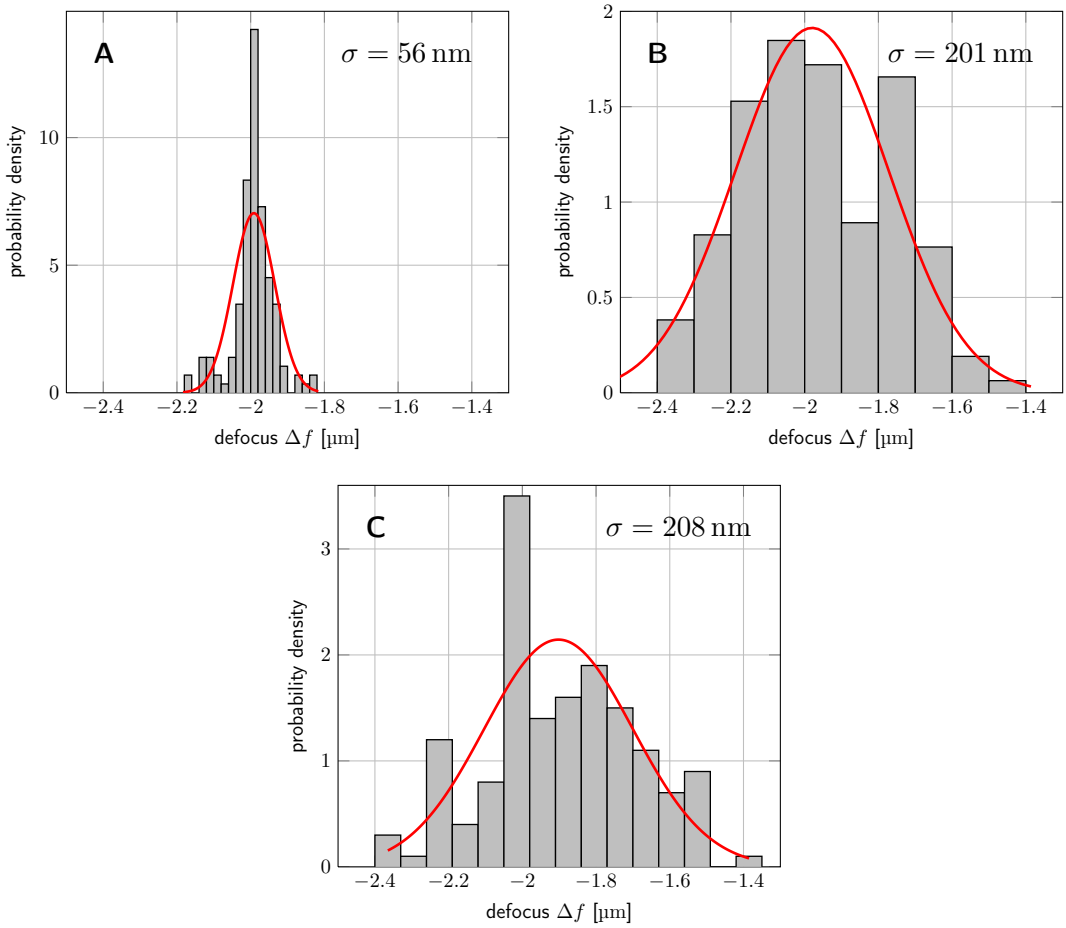

Figure 3.1.2: Auto focusing accuracy. The performance of the auto focusing routine was tested by acquiring micrographs after focusing at different specimen positions. The exact defocus of the acquired micrographs was determined using the CTF, the distribution of defocus values on different specimens and acquisition schemes is depicted. (A) PDF of micrographs recorded using a negatively stained sample, the auto focusing and acquisition were executed at the same position. (B) PDF of micrographs recorded using a negatively stained sample, the auto focusing and acquisition position are located adjacent to each other (2.5 µm distance). Note that the standard deviation of the defocus distribution increases by a factor of 3 to 5 compared to (A). (C) PDF of micrographs recorded using a vitrified ice sample, the auto focusing and acquisition position are located adjacent to each other (same setup as in (B)). No significant increase of standard deviation between negatively stained and unstained vitrified ice specimens is observed.

3.1.2 Stage Drift

In single particle acquisition, between state group executions the stage is moved to a new sample position. After such a movement, the stage drifts for a certain time and thus acquisition of micrographs should not be performed to avoid motion blur in the images. Therefore, the acquisition has to be delayed until the specimen drift has settled below a certain threshold value (typically $< 2\,\text{Å}\,\text{s}^{-1}$).

The necessary time needed to settle the stage was determined by the following algorithm: The stage was moved in x and y direction by 5 µm (which represents a typical movement between two sample positions during single-particle investigations). Then a template micrograph (object pixel size 2 Å) was acquired at time $t = 0$ followed by the acquisition of micrographs in intervals of 10 s up to 90 s. The sample drift was measured by correlating the micrograph acquired at $t = 0$ with the other micrographs and measuring the shift vector. The measurement was repeated 2 times for reproducibility.

Figure 3.1.3 shows that the drift after stage movement settles after 40 s of a lateral stage movement using the Tecnai F30 "Polara" stage, and after 30 s using the Titan Krios stage. Therefore, one can conclude, that using the Titan Krios stage provides a slight advantage. However, this waiting time can be used to perform microscope tuning operations that do not depend on sample drift such as automated beam centering.

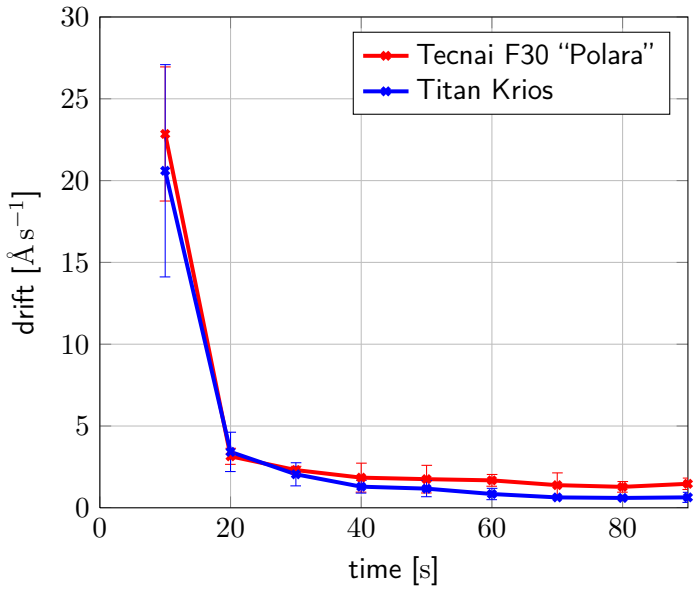

Figure 3.1.3: Comparison of stage drift rates in FEI Tecnai "Polara" and Titan Krios microscopes. To avoid drift in the acquired micrographs, acquisition needs to be paused for 20 s to 30 s after the stage has been moved in lateral direction. Error bars represent standard deviation from measured data points.

3.1.3 Contamination Buildup Rate

During acquisition, the electron beam is evaporating sample material of a frozen-hydrated specimen. This evaporated material consists of ice [Cheng *et al.*, 2006] and should be partially removed from the vacuum by the cold surface of the anti-contaminator ("cryo-box") that encloses the specimen. However, the material also condensates on the cold specimen surface leading to an increase of specimen thickness over time. The electron transparency of the specimen is dependent on its thickness d

$$I = I_0 \cdot e^{-\epsilon \cdot d} \tag{3.1.1}$$

where I is the measured beam intensity at the detector, I_0 is the initial beam intensity and ϵ is the absorption coefficient of the sample material [Lambert, 1760; Beer, 1852]. This means that the beam intensity and thus the SNR at the detector will decrease exponentially with linearly increasing sample thickness. Since ϵ is not known for the sample material, an absolute specimen thickness cannot be calculated. ϵ can be estimated by comparing changes in image contrast with the length of tilted holes in the specimen, created by a condensed beam [Cheng *et al.*, 2006], but is dependent on the magnification, defocus value and objective aperture used. Nevertheless, even without knowledge about the value of ϵ, relative increases in thickness can be calculated by comparing the intensity decrease over time during acquisition.

Since the SNR is an important influential factor on the resolution of the micrographs, the sample cannot be used after a certain amount of acquisition time. Figure 3.1.4 compares the contamination rates in FEI Tecnai and Titan Krios microscopes. When using a Tecnai F30 "Polara" microscope, the sample can be imaged over 72 h without any significant increase in specimen thickness (acquisition parameters are described in section 3.2.1). Specimens in the Titan Krios microscope however show a four-fold increase in contamination rate, the sample can be used for acquisition of 24 h only and has to be replaced after that period of time (acquisition parameters are described in section 3.1.4).

To keep the SNR in the micrographs constant over time, the exposure time of the detector can be adapted to compensate for the decrease in beam intensity. However, this method is limited because a substantial increase in exposure time will lead to an increase of dose and thus potential damage to the specimen. Thus, an increase of exposure time can only partially compensate for the effects of contamination buildup on a frozen-hydrated specimen.

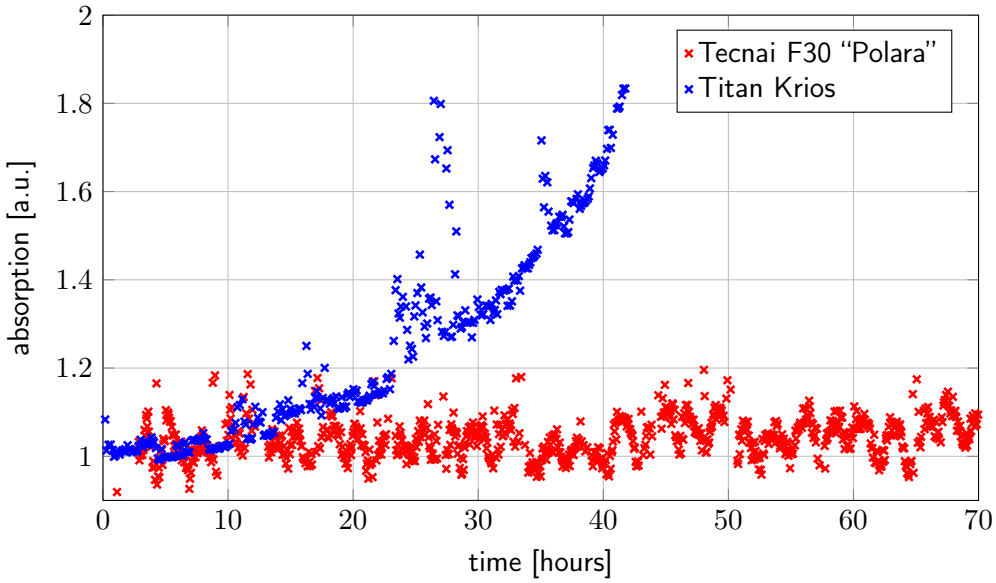

Figure 3.1.4: Comparison of contamination rates in FEI Tecnai F30 "Polara" and Titan Krios microscopes. Due to contamination buildup at the specimen surface, the relative electron transparency of the specimen material is decreasing over time. Absorption was measured by evaluating the mean counts of all micrographs acquired during a single particle acquisition run with constant exposure time. In Tecnai F30 "Polara" microscopes an increase of absorption (relative thickness) of $\approx 10\,\%$ is observed. In the Titan Krios microscope, the contamination rate shows a four-fold increase, making the sample unusable for acquisition after 24 h.

3.1.4 Data Acquisition

QuantiFoil specimen grids (hole diameter 2 µm, hole distance 1 µm) were plunge-frozen using the VitroBot (FEI Company, Eindhoven, The Netherlands). Data acquisition was performed on the Titan Krios instrument, operated at 200 kV to increase the sensitivity of the detector [Sherman *et al.*, 1996]. The DQE of the detector shows an increase by 50 % when using 200 kV instead of 300 kV (see section 1.2). An acquisition scheme similar to that described in section 2.6.1 was used. To maximize the area showing ice-embedded particles in the micrographs, QuantiFoil grids with regularly spaced holes in the carbon support film were used instead of lacey carbon which show a random distribution of carbon support film. Due to the regular structure of the carbon support film of these grids, the acquisition states can be placed in areas containing only ice with embedded particles and no carbon areas. This way, each micrograph contains a maximum amount of protein complexes, whereas in a lacey carbon support film, around 30 % of the micrographs show only carbon support film with no particles.

The state group was designed to contain a central focus position (located on the center carbon foil of four QuantiFoil holes with diameter of 2 µm, hole distance 1 µm) and four adjacent acquisition positions, each located in one QuantiFoil hole. Overall, areas covering 6 mesh grids were selected for automated acquisition. The grid was rotated using the stage's β tilt system to orient the QuantiFoil holes along the stage's x axis. The state groups were placed in a way, that one move would bring the next four holes approximately in the field of view at a magnification of 3800 ×. To place the state group exactly on the center of the next four holes, a tracking state (magnification 3800 ×) was used (see figure 3.1.5). Using this acquisition scheme, the recorded micrographs showed a FOV with only particles embedded in ice and the focus state would be always performed on carbon film to maximize contrast during focusing and thus maximizing focusing precision. The acquisition magnification was set to 47 000 × on the fluorescence screen corresponding to a pixel size in the object plane of 1.02 Å. The micrographs were acquired with a binning factor of 2 in order to reduce the amount of data that needs to be read out from the detector and saved to disk. The detector has a limited frequency response (MTF, see section 1.2). By binning the micrographs (averaging four adjacent pixels and saving the resulting value in one pixel), the size of the micrographs was reduced by a factor of four without deleting any information content (except high-frequency noise) in the image [Hartley, 1928; Shannon, 1949].

Over the range of 42 h 1768 focal pair micrographs were recorded. The defocus was set to four groups for the low-defocus micrographs (−1.4 µm, −2.0 µm, −2.3 µm, −2.6 µm), the exposure time was set to 0.2 s, resulting in a dose of of ≈ 20 electrons/Å^2. The defocus values were calculated to obtain an optimal fill-up of the frequencies in the PSD reconstruction of the 3-D model (see section 2.6.1). Since the number of projections of protein complexes required to obtain a high-resolution structure is very high (up to 1 000 000, see section 3.1), automated particle detection methods are necessary to generate an image stack containing projections of the protein complex. Since the low-defocus micrographs showed too little image contrast and a too low SNR to be searched for the complexes in an automated fashion, high-defocus micrographs (defocus −3.5 µm, dose ≈ 30 e$^-$/Å^2) were recorded after recording of a low-defocus micrograph at the respective sample position to facilitate automated particle picking.

The 3D model of the 20S proteasome was reconstructed from 50 000 particles using XMIPP [Scheres *et al.*, 2008]. 10 defocus groups were used in 40 iterations. Table 3.1.1 gives an overview of the refinement parameters used for reconstruction of the final model. The resolution of the final model depicted in figure 3.1.7 was determined to be approximately 11 Å. Figure 3.1.6 shows the plot of the Fourier shell correlation (FSC).

The 50 000 projections of the 20S proteasome (14-fold symmetry), acquired within

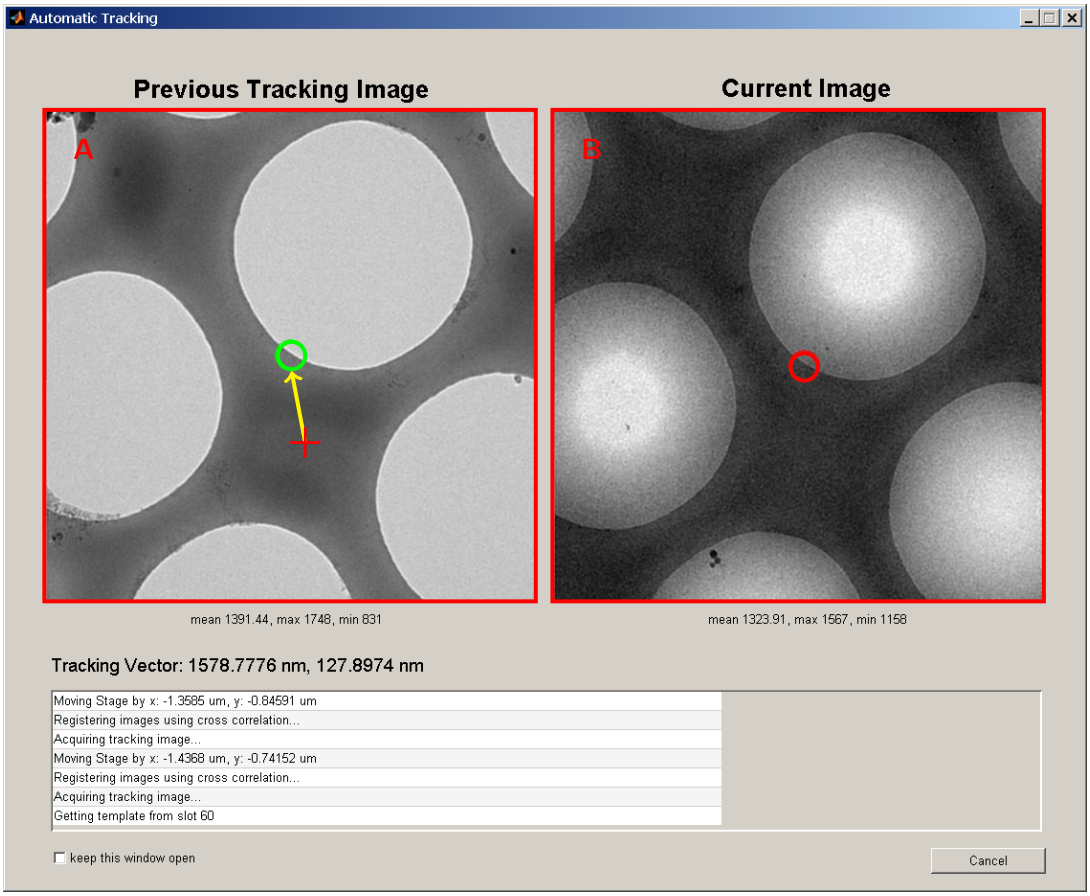

Figure 3.1.5: Using the automated tracking algorithm to center QuantiFoil holes (hole diameter 2 µm). (A) On a grid area without ice the image is centered on the carbon film between four holes (red cross) at the acquisition magnification (47 000 ×). Then the magnification is switched to the tracking magnification (3800 ×) and the template is acquired. Due to the image shift between high and low magnifications (yellow arrow), the center of the four holes is not the center of the FOV (green circle) during tracking. (B) During acquisition the template (left image) is used to center a similar feature (red circle) (right image). After switching the magnification the carbon film will be centered for performing the tuning and acquisition states.

Table 3.1.1: Refinement parameters of the 20S proteasome data set

number of iterations	binning	angular increment	symmetry
8	0	10.0°	D_7
8	0	5.0°	D_7
8	0	2.0°	D_7
8	0	1.0°	D_7
8	0	0.5°	D_7

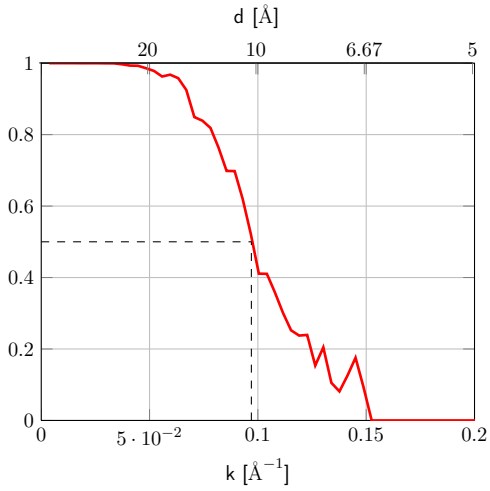

Figure 3.1.6: FSC of the final 20S proteasome model. The resolution was calculated to be 11 Å (dashed line marks the 0.5 FSC cutoff criterion).

2 days, are approximately equivalent to 700 000 projections of the 26S proteasome (no symmetry). Therefore, to acquire a data set of the 26S proteasome of the same size, approximately 30 days of acquisition are required, assuming an equivalent density of intact 26S complexes in the specimens. Since the 26S proteasome complexes are more fragile and the concentration in the ice-layer is typically less dense, we estimate that a total acquisition time of up to 60 days will be required to generate a data set that can be used to reconstruct the 26S proteasome with a resolution of 10 Å.

In summary, the performance of the Titan Krios microscope is sufficient for high-throughput single-particle acquisitions of frozen-hydrated specimens. Using the automated acquisition approach in TOM^2, it will be possible to acquire large data sets of the 26S proteasome, resulting in high-resolution 3-D models of the holocomplex. However, it is definitely desirable to increase the dwell time on one single specimen from 24 h to three or even five days. This way, samples of fragile and difficult to prepare complexes or samples which are present only in very low concentrations or volumes could be investigated exhaustively.

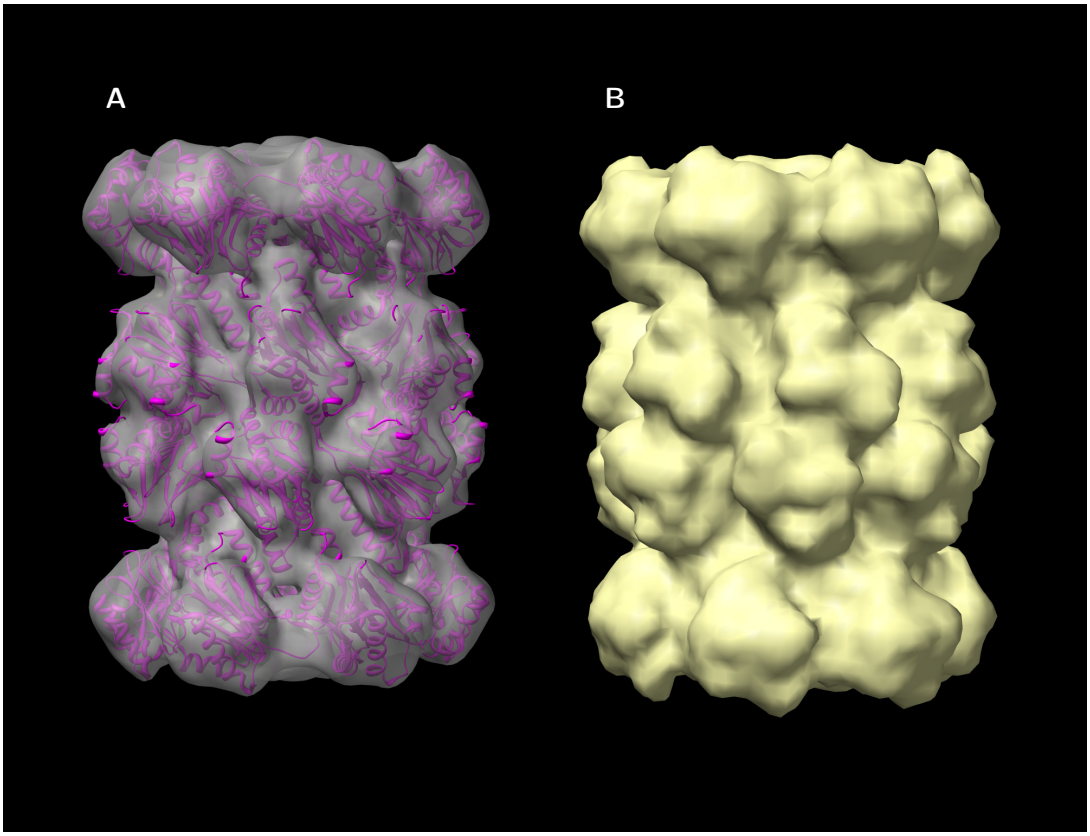

Figure 3.1.7: Isosurface representation of the 20S proteasome from *Thermoplasma acidophilum*. (A) The isosurface value was set to include a mass of 720 kDa, the length of the complex is 14.8 nm. The crystal structure was fitted into the model using USCF Chimera [Pettersen *et al.*, 2004; Goddard *et al.*, 2007]. (B) The crystal structure was used to calculate an electron density map with a resolution of 10 Å. Comparision of this density map to the EM model shows similar features and thus it can assumed that the EM model shows a similar resolution.

3.2 Use Cases for the TOM^2 Software

3.2.1 Single-Particle Acquisition of Tripeptidyl Peptidase II

The aim of this project was the determination of the 3D structure of the tripeptidyl peptidase II (TPPII) complex.[1]. The TPPII protein complex is an NEM-sensitive serine peptidase of the subtilisin family, which releases tripeptides from free N-termini of oligopeptides. It acts downstream of the proteasome in the cytosolic ubiquitin-proteasom-degradation pathway, further degrading oligopeptides and trimming epitopes for MHC class I. By cleaving the neuronal peptide cholecystokinin 8 (CCK-8), TPPII is involved in satiety control and apparently also plays a role in the regulation of fat storage. Up-regulation of TPPII in tumor cells results in less susceptibility to mitotic arrest and higher proliferation rates. Although TPPII participates in various biological processes its exact mechanism and function is not yet fully understood.

40 subunits of TPPII (138 kDa to 150 kDa, depending on the species) assemble into a unique spindle-like structure with a molecular mass of ≈ 5.7 MDa. This spindle consists of two segmented and twisted strands. The stacking of the ten interdigitated dimers per strand leads to the formation of a system of internal cavities accessible via lateral openings, which harbors the active site. The specific activity increases upon stacking thus indicating a contact-induced activation mechanism. The individual subunits can associate and dissociate from the complex. Also, the spindle structure of the complex shows flexibility.

The complex was prepared and purified as described previously [Rockel *et al.*, 2005]. A vitrified specimen of TPPII on a lacy carbon grid was imaged over 72 h with a Tecnai F30 "Polara" microscope operated at 300 kV and equipped with a Gatan UltraScan 4k $\times$ 4k pregif CCD camera. The acquisition scheme described in section 2.6.1 was used, comprising of a central focus position and eight adjacent acquisition positions in each state group (see figure 2.6.1), covering in total 13 meshes of one EM grid. Approximately 3500 focal pairs were acquired (low defocus $D_{zl} = -1.5\,\mu$m to shift the zero crossings of the CTF to high frequencies and obtain a maximum resolution in the 3-D model; high defocus $D_{zh} = -4.5\,\mu$m for added contrast in particle selection), with a determined object pixel size of 2.06 Å. The exposure time for each micrograph was set to 0.6 s resulting in a dose of ≈ 30 electrons/Å^2 per micrograph. Approximately 2400 focal pairs were selected for post-processing, since they showed areas with ice and embedded TPPII complexes. The other micrographs did not contain any complexes or only areas of carbon support film were images. Figure 3.2.1 depicts a micrograph containing TPPII complexes

[1] This project was done in collaboration with Anne-Marie Schoenegge and Beate Rockel.

in various orientations.

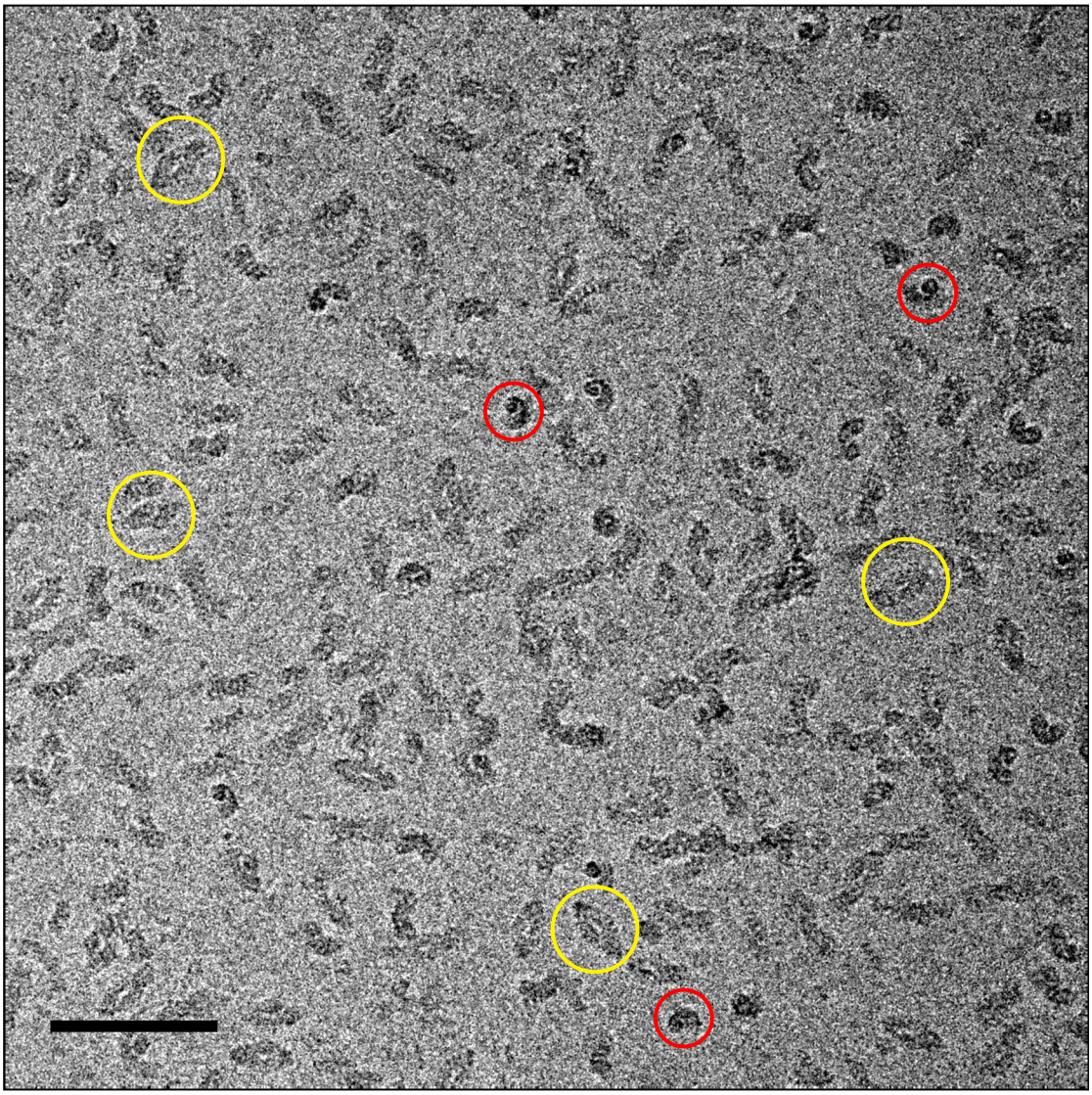

Figure 3.2.1: Example micrograph showing TPPII complexes embedded in ice an imaged at an object pixel size of 2.06 Å, defocus value is −4.5 µm. Example particles are marked, e.g., top view (red circles), or side view (yellow circles). Scale bar is 150 nm.

The micrographs of each focal pair exhibited a slight image shift due to their defocus difference. To compensate this image shift, they were aligned using a cross-correlation based method implemented in the TOM toolbox [Nickell *et al.*, 2005]. Then, the CTF of the low-defocus micrographs was determined using an algorithm implemented in the TOM toolbox (see section 2.3.7). Using the exact defocus value for each micrograph, phase-flipping of the CTF was done (see section 2.6.1).

The particle picking was performed manually, the high defocus micrographs were used to identify and select the particles. Automated particle picking would have been an alternative to manual selection, but was not carried out because manual selection provided a more complete data set. 96 700 particles were selected and boxes of 400×400 pixels, each containing one particle, were cut out of the aligned low-defocus micrographs and combined to a stack of images, each showing one particle. To normalize for contrast and brightness differences, the pixel values of each particle image in the stack were normalized to have a mean value of 0 and a standard deviation of 1.

The construction and refinement of a 3-D model of the TPPII complex was done in EMAN [Ludtke *et al.*, 1999]. A low-resolution 3-D model of the TPPII complex, obtained by previous studies, was used as a starting model for the refinement. The goal of the refinement process is the determination of the projection direction of each particle with respect to the 3-D model. To find the particle orientation, each particle was compared against a template library of projections generated from the 3-D model (see section 1.5). The refinement parameters of the 3-D structure was done as shown in table 3.2.1.

Table 3.2.1: Refinement parameters of the TPPII data set

number of iterations	binning	angular increment	symmetry
3	1	2.5°	C_2
1	1	2.0°	C_2
2	0	2.0°	D_2

To determine the resolution of the final model, two 3-D models were created, each model comprised of a random half of the data set, the resolution was calculated using FSC using the 0.5 criterion [Saxton and Baumeister, 1982]. The resolution of the final model was determined to be 27 Å. Figure 3.2.2 shows the plot of the FSC.

The resolution of the model depicted in figure 3.2.3 could be further improved by adding more particles, applying classification to the particles to account for flexibility of the complex, and running more refinement iterations. However, this project shows the capabilities of the automated data acquisition with TOM^2 to record data over an extended period of time (in this case 72 h using one specimen grid) in a completely unsupervised manner. The resulting micrographs are of constant high quality and are suited for single particle extraction and analysis. However, the resolution is limited not only by the number of particle projections, but furthermore by the utilized detecting device. To obtain a model of the TPPII complex with better resolution, the magnification would need to be further increased. Additionally, the Gatan UltraScan CCD camera is not able to record high-frequency information with sufficient sensitivity, because of the

MTF of this specific camera. Therefore, a more sensitive detecting device such as an Eagle 4k CCD camera has to be used for further studies (see section 1.2).

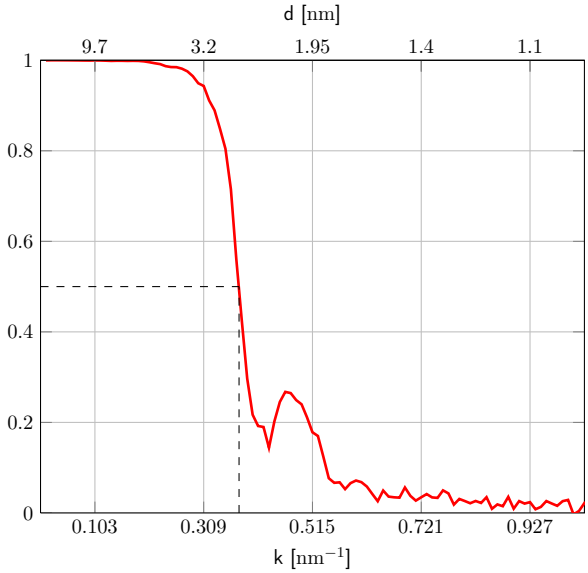

Figure 3.2.2: FSC of the final TPPII model. The resolution was calculated to be 27 Å (dashed line marks the 0.5 FSC cutoff criterion).

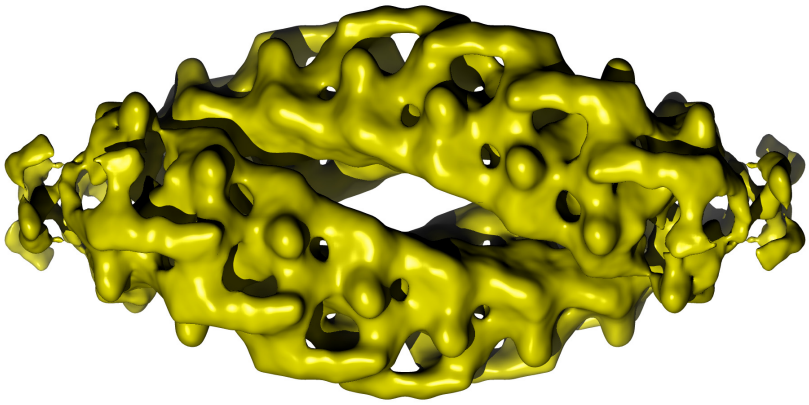

Figure 3.2.3: 3-D reconstruction of the TPPII complex at 27 Å resolution. The length of the particle is ≈ 60 nm.

3.2.2 Tomography of *Spiroplasma citri*

The aim of this project was the acquisition of tomograms of *S. citri* cells and the detection of macromolecular complexes (e.g., ribosomes) inside of the cytoplasm during different stages of the growth phase of the cells[2]. The structural variability of the macromolecular complexes in different stages of the growth phase is of interest to link cellular functions to the structure and composition of these molecular complexes. By sub-tomogram averaging and classification, this variability can be observed using many (up to thousands) individual complexes. To obtain this amount of complexes in tomograms of cells, dozens of tomograms are needed. Also, the distribution of macromolecular complexes inside of the cell ("molecular atlas") is of interest to investigate interactions between different functional types of these complexes (see section 1.4).

Spiroplasma citri is a plant pathogenic bacteria that belongs to the family of mollicutes. These are a class of microorganisms phylogenetically related to low G-C content Gram-positive bacteria [Weisburg *et al.*, 1989]. They are characterized by the lack of a cell wall, a small genome size, a small number of rRNA operons and their relatively limited metabolism [Bové, 1993]. Mollicutes are one of the smallest, most rudimentary free living and self replicating prokaryotic organisms that are only restricted by a cholesterol containing membrane [Tully, 1992].

Plant pathogenic mollicutes are associated with several hundred diseases affecting plants of great economic importance. *S. citri*, the causal agent of of citrus stubborn disease, has been cultured since 1970 [Saglio *et al.*, 1971; 1973]. Over the years it has become a model organism for studying the relationship of plant mollicutes with their host, the plant and the insect vector [Bové *et al.*, 2003; Fletcher *et al.*, 1998].

In liquid medium the cells form helical shapes with a diameter of 80 nm to 200 nm and a length of approximately 3 µm in the logarithmic growth phase up to 10 µm in stationary phase.

Tomograms of *S. citri* cells were acquired using a FEI Tecnai F30 "Polara" microscope operated at 300 kV, equipped with a Gatan post-column energy filter and 2k × 2k CCD camera. The magnification on the fluorescence screen was set to 27 500 × resulting in a pixel size in the object plane of 4.67 Å. The tomograms were acquired with a defocus of 4 µm and 8 µm using a tilt range of −60° to 60° in steps of 2°. The images were filtered around the zero-loss peak with a slit width of 20 eV. The exposure time was set using a cosine scheme to adapt to the increasing sample thickness at increasing tilt angles. The applied total dose for one tilt series was around 80 $e^-/Å^2$. Overall, 67 tomograms were acquired for further analysis.

[2]This project was done in collaboration with Carolin Fleischer.

The time needed to acquire one tomogram was 60 min using the previously described acquisition scheme (section 2.6.2). The tilting scheme was setup to start from 0° to 60° in steps of 2°. Then the acquisition and focus states are deactivated and the stage is tilted back to 0° in steps of 5° with only tracking enabled to keep the object in the FOV and return to the original specimen position at 0°. Then the second half of the tilt series is recorded from 0° to −60°. This backtracking from 60° to 0° takes less than 5 min or 10 % of the total acquisition time. It has the advantage that the magnification is not being changed during the acquisition, thus the stability of the optics is not impaired. Typical lateral displacements are in the range of 100 nm per 2° step. Focus changes per 2° step are usually below 150 nm.

Another approach to speed up the tilting from 60° to 0° is to switch to a lower magnification and record a template image before starting the tilt series. Then instead of tracking back in 5° incremental steps the stage can be set directly to 0° and using the lower magnification template, the sample position can be re-centered. This method saves the time needed for the backtracking, however the optics of the microscope are changed during switching of magnifications, this can cause hysteresis effects which will induce beam changes (e.g. beam center changes, introduction of astigmatism) which need to be compensated before acquiring the second half of the tilt series.

Further reduction of the acquisition time can only be achieved by accelerating the readout of the CCD camera or omitting tracking and focusing steps using a pre-calibration based prediction model [Mastronarde, 2005]. This predicition model states that the stage movement in x, y and z directions will be constant and thus reproducible for a specific stage and holder. In contrast, using full tracking / full focusing, one would be able to to determine x, y and z movements and then apply these shifts during the acquisition of a tomogram (see section 2.6.2). However, the lateral tracking data in figures 3.2.4 and 3.2.5 show that the stage displacements are strongly dependent on the location within a 3 mm specimen grid. The differences are severe (deviations depending on the sample position up to 1 µm), so that full tracking and focusing is still advisable to ensure high quality image recording. The time invested compensating for the stage movements during the acquisition of a tilt series is necessary to avoid the loss of the feature of interest which will eventually render the acquisition of the tomogram meaningless. Figure 3.2.6 shows typical stage displacements that have to be compensated during the acquisition of a tilt series.

The projections of the tomograms were aligned using gold beads in the specimen as fiducial markers. Then the tomographic volumes were reconstructed using the weighted backprojection algorithm implemented in the TOM toolbox [Nickell *et al.*, 2005]. In the reconstructed volumes, ribosomes in the cytoplasm of the cells were detected using the

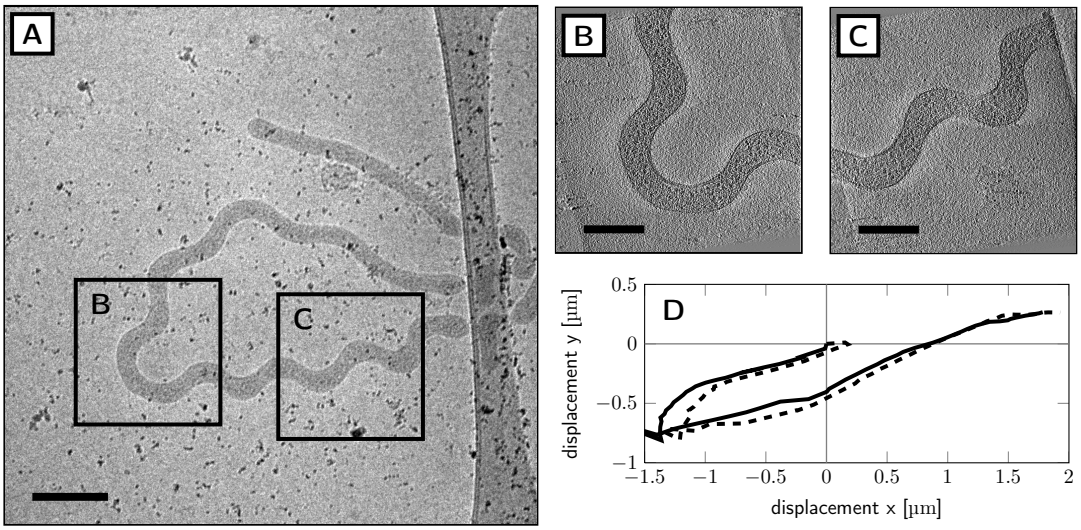

Figure 3.2.4: Overview of two tomography positions for *S. citri*. (A) Overview of *S. citri* cells embedded in vitrified ice on a lacey carbon grid. Rectangles mark the positions where a tomogram was taken. Scale bar is 500 nm. (B) and (C) Ortho slice of acquired tomogram. Scale bar is 200 nm. (D) Lateral displacement of the feature of interest during acquisition of the tomogram. The displacement was measured and compensated using the automated tracking algorithm implemented in TOM^2. Solid and dashed line is displacement of tomogram (B) and (C) respectively.

MOLMATCH template matching software [Frangakis *et al.*, 2002]. Subtomograms each containing one complex were extracted from the tomograms, the subtomograms were aligned, averaged and classified using functions of the TOM toolbox.

The distribution and orientation of the detected ribosomes were visualized as a "molecular atlas" (see figure 3.2.7). The resulting 3D models were used to analyze structural changes of the ribosome in cells that are in different growth phases in order to detect the binding of ribosomal co-factors during the different stages of the growth phase of the cells. For further details and results, see [Fleischer, 2010].

This project was successfully conducted using TOM^2 for acquisition of the tomograms. 67 tomograms were acquired, the acquisition time for one tomogram was 60 min which enables recording of 10 to 15 tomograms in one microscope session. In summary TOM^2 enables scientists to investigate macromolecular complexes inside of intact bacterial cells by providing a tool to define a specific acquisition scheme for the investigation at hand and recording the data set in a reasonable amount of time.

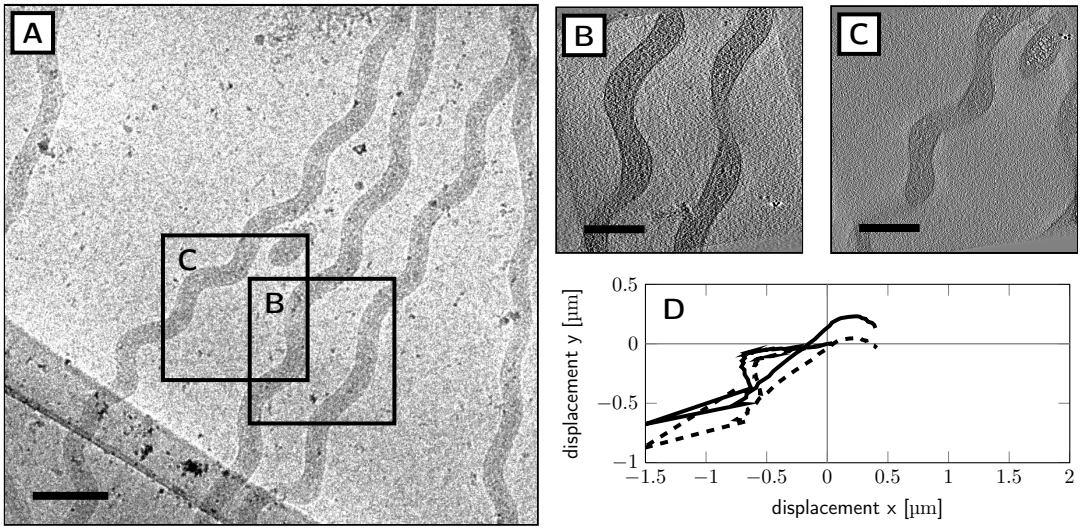

Figure 3.2.5: Overview of two tomography positions for *S. citri*. (A) Overview of *S. citri* cells embedded in vitrified ice on a lacey carbon grid. Rectangles mark the positions where a tomogram was taken. Scale bar is 500 nm. (B) and (C) Ortho slice of acquired tomogram. Scale bar is 200 nm. (D) Lateral displacement of the feature of interest during acquisition of the tomogram. Solid and dashed line is displacement of tomogram (B) and (C) respectively. Note that the dispacements of (B) and (C) are similar, but dissimilar to the displacements shown in figure 3.2.4. This illustrates the dependency of lateral displacement on the grid position, therefore pre-calibration of the stage cannot be used to omit tracking and focusing steps. Full tracking / full focusing is required to record a tilt series where the feature of interest is correctly centered in the FOV.

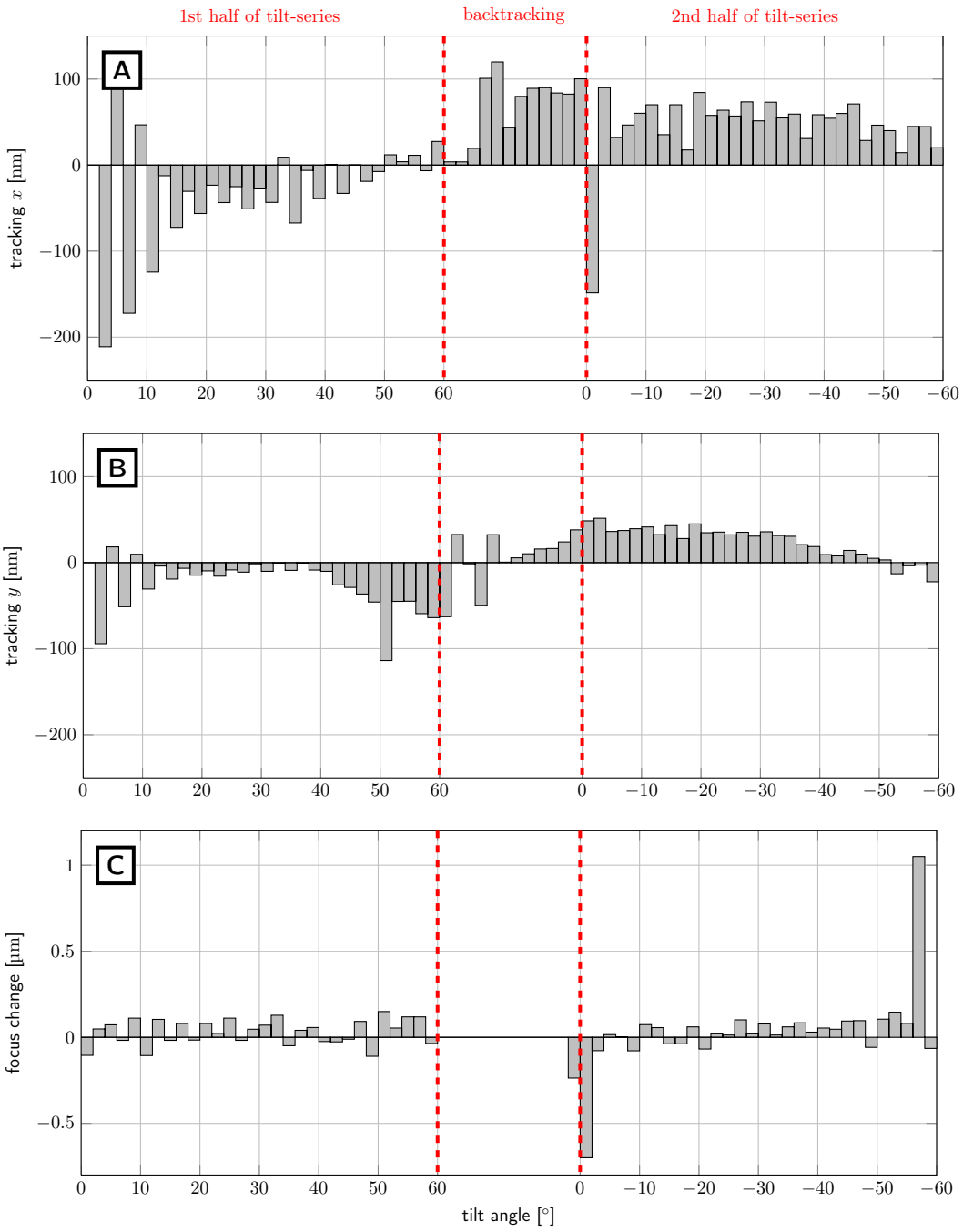

Figure 3.2.6: Stage Tracking during a tilt series. Tilting was started at 0° to 60° in steps of 2°. Then the stage was tilted back to 0° in steps of 5° without acquiring micrographs, only tracking was enabled to bring the specimen back to its original position. Afterwards the stage was tilted to −60°. Using a tracking and focus state at each tilt angle the stage displacement due to tilting is compensated. When the specimen is in eucentric height, the displacements should be minimized. (A) and (B) Typical lateral displacements are in the range of 100 nm per 2° step. (C) Focus changes per 2° step are usually below 150 nm. Note the larger focus change at the beginning of the second half of the tilt series (to compensate the entire focus change of the backtracking) and the outlier at −58°, caused by an unsuccessful auto focusing due to the high focus gradient at high tilt angles.

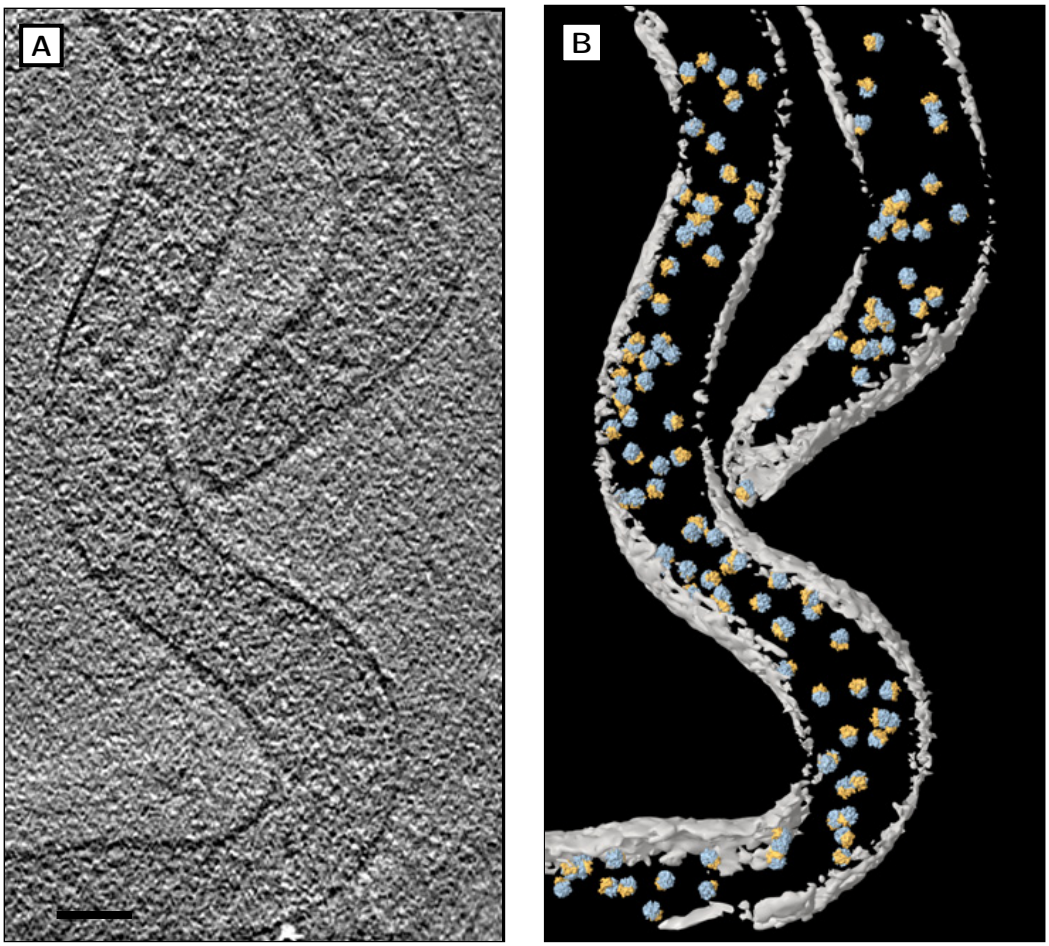

Figure 3.2.7: Distribution of ribosomes in *S. citri* cell. (A) A x-y slice of a typical tomogram of a *S. citri* cell in stationary phase. (B) Using template matching techniques, ribosomes in the cytoplasm of the cell were detected and are visualized as a "molecular atlas" inside of the cell. Scale bar is 50 nm.

3.2.3 Batch Tomography of *Escherichia coli* Mini Cells

The aim of this investigation was the acquisition of macromolecular complexes inside of cells to investigate their structure in a native environment using sub-tomogram averaging and classification, as described previously (see section 3.2.2). The complexes are expressed in *E. coli* mini cells[3].

In *Escherichia coli* cells, cell division is tightly coupled to DNA replication. Blocking of DNA synthesis leads to induction of the SOS response and cell division is rapidly arrested [Jaffé *et al.*, 1986; 1988]. In mutant strains where these division inhibitors cannot operate, division is not arrested completely. When DNA synthesis is perturbed in strains carrying the *mutB* mutant, cell division leads to the production of tiny spherical cells [Adler *et al.*, 1967], so called "mini cells". These mini cells do not contain DNA, but they show otherwise native cytoplasm with macromolecular complexes. Moreover, a large variety of molecular biological techniques are available for *E. coli*, proteins can be expressed, deleted and mutated in these cells with established biochemical methods. Although they are prokaryotes, eukaryotic proteins can also be expressed in their cytoplasm using commercially available plasmids. This makes these cells a potential candidate for studies of macromolecular complexes in their native form and environment.

Mini cells are better suited for electron tomography than full-sized cells because their small size makes them transparent for the electron beam. However, acquisition of these cells is still challenging because of their thickness of up to 500 nm. Additionally their lateral size is 500 nm to 600 nm and thus almost as large as the detector FOV (750 nm) at a magnification that is high enough to detect macromolecular complexes.

Due to the fact that many particles are needed and thus many tomograms need to be acquired, the acquisition was performed using a batch tomography approach described in section 2.6.3. A specimen of *E. coli* mini cells was plunge frozen. Acquisition was performed using a Tecnai F30 "Polara" microscope operated at 300 kV, equipped with a Gatan post-column energy filter and 2k × 2k CCD camera.

To identify positions of mini cells on the specimen grid, a map of the specimen was obtained acquiring 10 × 10 micrographs at a magnification of 280 × (object pixel size 200 nm) (see section 2.4). Sample positions were selected manually and a template image for re-centering the position during acquisition was recorded at each position at a magnification of 4500 ×.

The automated batch tomography routine was then started to acquire a tilt series of each sample position sequentially in an unsupervised fashion. As a preparation step before the acquisition of each tomogram, the position was re-centered using the respec-

[3]This project was done in collaboration with Dennis Thomas.

tive template image in an automated tracking procedure using SIFT (see section 2.3.2). Additionally, the eucentric height was adjusted using the auto eucentric height function (see section 2.3.8). Following these preparation steps, the magnification was changed to 27 500 × (object pixel size 4.67 Å), the beam was centered (see section 2.3.5) and the energy filter slit was adjusted (see section 2.3.10). Then the tomogram acquisition was started.

Each tomogram was acquired using a tilt increment of 2°, tilting range of −60° to 60°, with a magnification on the fluorescence screen of 27 500 ×, resulting in a pixel size in the object plane of 4.67 Å. The mean defocus was −6 µm. The images were filtered around the zero-loss peak with a slit width of 20 eV. The total dose was fractionated using a cosine exposure scheme, the total dose was approximately 80 $e^-/Å^2$.

To test the reliability of the batch tomography acquisition 5 tomograms were acquired completely unsupervised. The tomograms were reconstructed using a customized SPIDER script [Frank *et al.*, 1996]. Figure 3.2.8 shows slices of a typical tomogram of a *E. coli* mini cell. All 5 tomograms showed the contents of an *E. coli* mini cell and are usable for the extraction of macromolecular complexes and subsequent processing.

It could be shown that unsupervised acquisition of tomograms using the batch tomography acquisition scheme implemented in TOM^2 is feasible. The cells are centered and acquired in an automated fashion requiring no user interaction during the acquisition run. Using the microscope for one week can produce sufficient amounts of data to continue with the detection of macromolecular complexes inside of the cells.

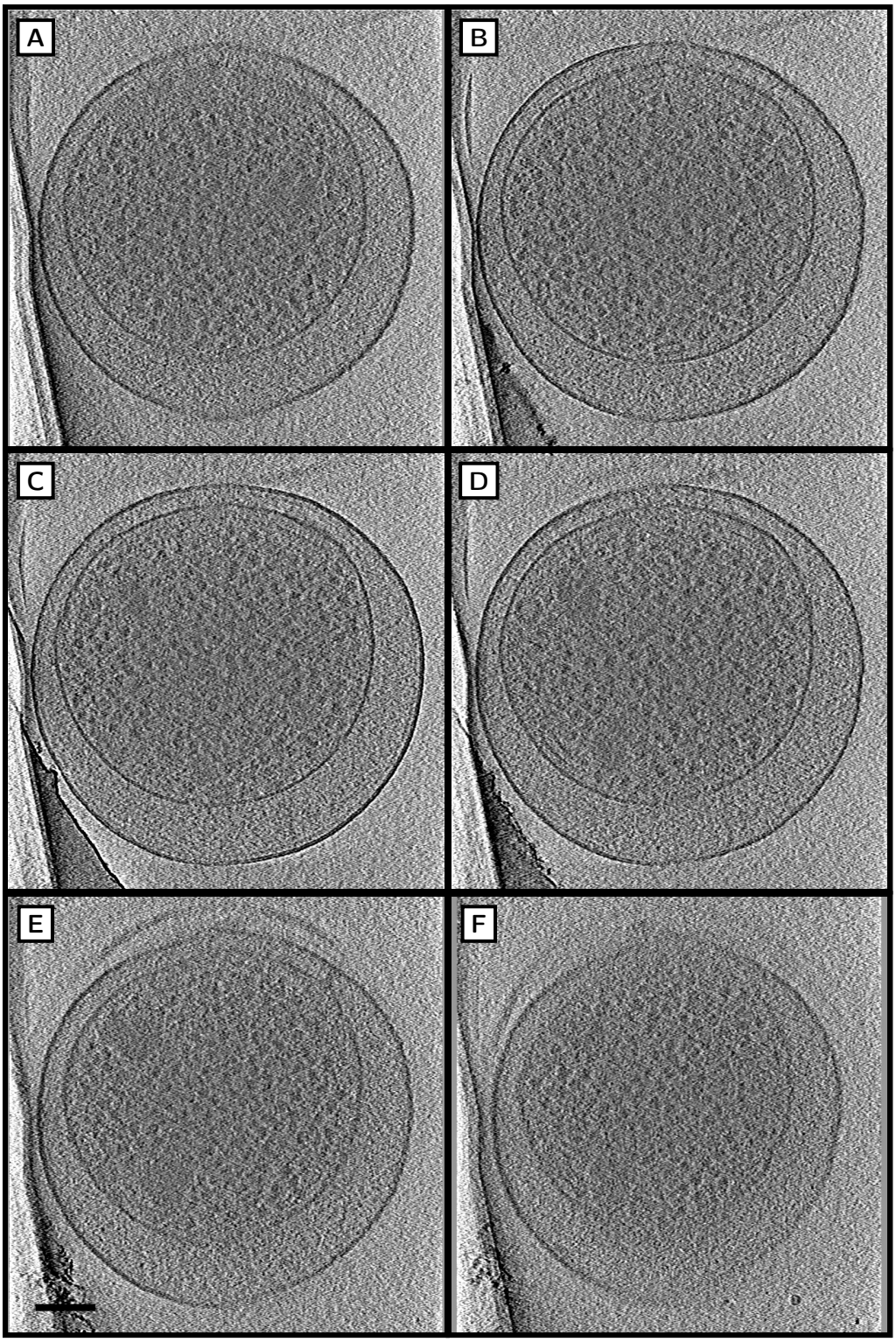

Figure 3.2.8: (A) – (F) $x - y$ slices with different z height of a typical *E. coli* mini cell tomogram showing the contents of a complete cell. Macromolecular complexes are clearly visible in the cytoplasm of the cell. Scale bar is 100 nm.

3.2.4 Batch Tomography of *Eisenia foetida* Sperm Cells

Eisenia foetida sperm cells are elongated cells (length up to 50 µm) with a thickness below 500 nm (see figure 3.2.9). They are comprised of the acrosome, and elongated nucleus containing condensed chromatin, the mid-body containing mitochondria and a flagellum consisting of a set of microtubules in 9+2 configuration [Rolando *et al.*, 2007]. These cells offer the possibility to create a stitched 3D tomographic reconstruction of a whole eukaryotic cell, if a cell can be found that is located entirely in one square mesh of the grid. Because of their elongated shape it is possible to acquire adjacent tilt series along the whole cell body. The aim of this project was the acquisition of a set of tomograms showing a large area of a sperm cell[4].

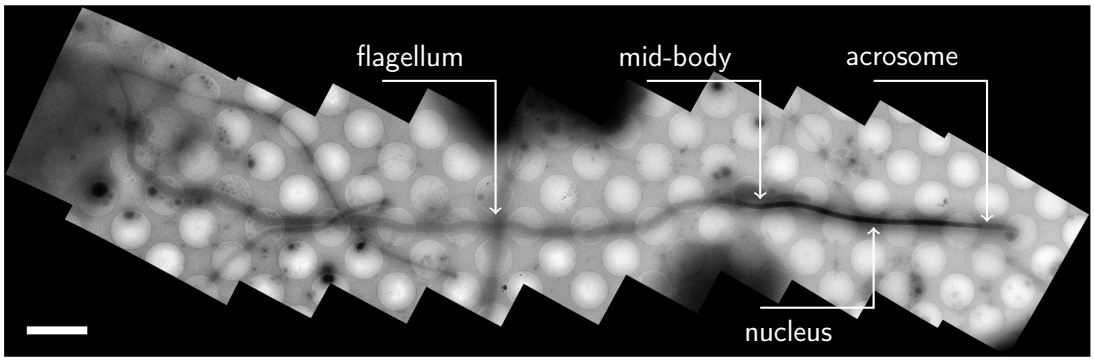

Figure 3.2.9: Overview of a *E. foetida* sperm cell. The acrosome is the organelle responsible for breaking through the egg's tough coating and allowing fertilization to occur. The nucleus contains condensated chromatin. In the mid-body six pyramid-shaped mitochondria are aligned around the long axis of the cell. At the end of the midbody, the flagellum in nucleated by a centriole. The flagellum is comprised of a 9+2 microtubule bundle structure. Sperm cell movement is achieved by shearing between microtubules caused by motor proteins. Embedded glycogen granules provide an energy storage for these motor proteins. Scale bar is 5 µm.

This project requires reliable acquisition of a set of approximately 50 tomograms that need to be placed and re-centered with a precision in the range of 100 nm in order to obtain a full view of the cell at a magnification of 34 000 × (object pixel size 6.61 Å). To allow combination of all tomograms in a large reconstruction of the entire cell, the imaging parameters (illumination conditions, defocus) should not change during acquisition. Moreover, since the acquisition time is limited to 2–3 days due to contamination buildup at the sample surface during acquisition (see section 3.1.3), one should acquire the data set as fast as possible and at best in an unsupervised fashion. Necessary tuning steps of

[4]This project was done in collaboration with Elizabeth Villa.

all microscope settings have to be repeated without user interaction periodically, compensating changes in the optical system and the energy filter settings over time. Tuning is performed using appropriate auto functions as described previously (section 2.3).

To test if the automated batch tomography acquisition scheme of TOM^2 (see section 2.6.3) is capable of recording such a data set, tomograms of a *Eisenia foetida* sperm cell were acquired. Acquisition was performed using a FEI F30 "Polara" microscope operated at 300 kV, equipped with a Gatan post-column energy filter and 2k × 2k CCD camera. Additionally a retractable Gatan UltraScan 4k × 4k pre-gif CCD camera was used to create a grid map of the specimen acquiring 10 × 10 micrographs at a magnification of 130 ×. On the map, a cell was identified and adjacent positions for tomography were marked (see figure 2.6.5). To re-center the positions of interest during acquisition in an automated fashion, a template micrograph of each position was recorded at a magnification of 4200 × on the pre-gif camera. The lateral stage inaccuracy when moving from one feature of interest to the next was measured to be ≈ 300 nm to 500 nm. Therefore, as a preparation step before the acquisition of each tomogram, the sample position was re-centered using the stage and an automated tracking procedure using SIFT. Additionally the eucentric height was adjusted using the auto eucentric height function (see section 2.3.8) at each sample position.

Following these preparation steps, the pregif camera was retracted, the magnification was changed to 34 000 ×, the beam was centered (see section 2.3.5) and the energy filter slit was adjusted (see section 2.3.10). Afterwards, the tilt-series was recorded.

Overall, four tomograms were acquired. Each tomogram was acquired using a tilt increment of 2°, tilting range of −60° to 60°, with a magnification on the fluorescence screen of 34 000 ×, corresponding to a pixel size in the object plane of 6.61 Å. The defocus was set to −12 µm. The images were zero-loss filtered with a slit width of 20 eV. The total dose was fractionated using a cosine exposure scheme, the total dose was approximately 100 $e^-/Å^2$.

Figure 3.2.10 shows three tomograms that were recorded along a sperm cell. This result illustrates the feasibility to acquire tomograms of an elongated thin cell. When dealing with a radiation sensitive sample such as a cryo-specimen, it is usually not possible to acquire overlapping tomograms. However tomograms can be recorded in close neighborhood, the missing area can be approximated from information of the two adjacent tomograms in the case of sperm cells where long microtubule bundles are the main feature of the cell.

In summary, these results show that batch acquisition of tomograms in a highly controlled manner is possible. The first set of 21 tomograms imaging a large portion of a cell has already been recorded, reconstruction of the data is in progress.

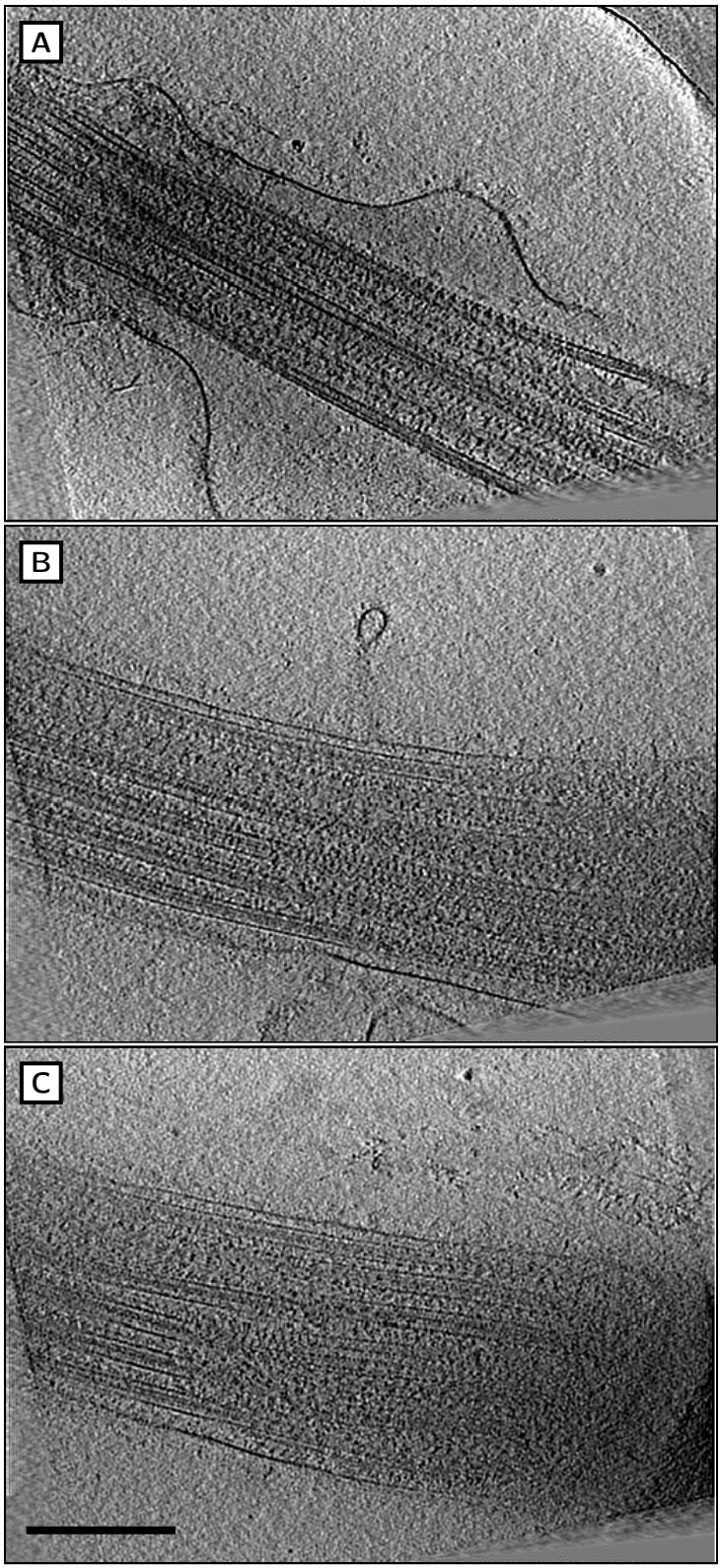

Figure 3.2.10: (A) – (C) Tomograms of a *E. foetida* sperm cell showing adjacent views of the tail of the cell. The tail consists of microtubuli, note the glycogen granules located between microtubuli. Scale bar is 300 nm.

4 Conclusions and Outlook

Structural investigations of cells and their macromolecular protein complexes are an important contribution to our understanding of their functional mechanisms. The "classical" method for structural investigations of whole cells is the use of light microscopy. Cells and their content can be labeled with fluorescent dyes to detect and identify cellular components. However, the resolution of a light microscope is limited and typically only sufficient to investigate the ultrastructure of a cell. To study the supra-molecular architecture of cells and molecules, other methods have to be utilized. On the other side, the structure of most of the smaller proteins that inhabit the contents of the cell's cytoplasm, can be studied after isolation, purification, and subsequent structural investigation using x-ray crystallography. However, larger protein assemblies are typically comprised of multiple different protein subunits. These subunits are often only weakly bound together, are fragile, and can show highly dynamic interactions with each other. These assemblies are sometimes difficult or even impossible to crystallize, thus other means of structural investigations have to be applied. Moreover, x-ray crystallography can only show the protein structures in a non-native crystalline environment, typically only with high salt concentrations.

TEM bridges the resolution gap between light microscopy and x-ray crystallography. It can be used to investigate the three-dimensional structure of pleomorphic objects such as cells by tomographic methods. It can also be utilized for the structural determination of large macromolecular complexes such as the ribosome or the proteasome in a more native environment. However, to obtain this structural information, large data sets are required, which have to be recorded under defined imaging conditions. In former times and even today, manual acquisition is used to gather the information needed. However, manual data collection is time-consuming and only possible with highly-trained specialists. Typically, it takes months or even years to conduct studies with the electron microscope. To shorten these time frames and to make these methods available even to non-specialists, automation is instrumental.

Sample preparations for TEM investigations are still hampered by the thickness of the specimens. Before a cellular specimen can be investigated using the TEM, its thickness often has to be reduced. This thinning can for example be performed using a focused

ion beam (FIB). Additionally, regions of interest in the specimen need to be identified. Typically, certain features inside cells are labeled using fluorescent dyes that need to be detected using light microscopic methods. By combining these methods and instruments, work-flows for sample preparation and investigations can be created. Since each instrument in this work-flow is an imaging device with common design principles, it is desirable to have a consistent user interface and software to facilitate its use.

TOM^2 is a novel acquisition software that enables users to operate the microscope efficiently and acquire large amounts of data in a highly automated fashion. The software was developed using the existing algorithms and functions that are implemented in various acquisition software packages. The robustness and accuracy of these automated microscope tuning procedures was enhanced using modern computer systems. By exploiting the capabilities of up-to-date computer systems running 64-bit operating systems, even large micrographs up to 8192×8192 pixels can be acquired and processed. Using parallelized algorithms, multi-core processors are used in TOM^2 to speed up the auto functions such as auto focusing.

The acquisition setup has been streamlined so that users are able to design their own acquisition scheme. This way, TOM^2 can be utilized for tomography and single particle applications, also hybrid approaches such as random conical tilt acquisition schemes can be designed.

TOM^2 works on FEI Titan and Tecnai microscopes and is being used routinely in the department. Using a HAL that separates the hardware functions from the graphical user interface, the software is also adaptable to new types of microscopes. New auto functions can also be added to TOM^2 in order to adapt the software to new acquisition procedures in crystallography and material science.

The next step in the development of a high-throughput pipeline for electron microscopy is the combination of the acquisition process with post processing steps. To optimize the acquisition of tomograms, the reconstruction algorithms can be adapted to produce a 3-D reconstruction of the tilt series on-the-fly so that the user is able to evaluate the quality of the recorded tomogram as it is being recorded. Adjustment of acquisition parameters such as dose or tilt increment could be communicated to TOM^2 during recording, leading to an optimized imaging process.

For single-particle investigations, the combination of acquisition and real-time post processing promises even greater benefits. Because particle distribution and orientation are not constant over the specimen, there are grid areas which are more “valuable” in terms of image content. When developing a feedback loop from the post-processing pipeline to the acquisition software, the microscope can be directed to these grid areas, where data that help increase model resolution can be recorded. Since the location

of these areas cannot be determined easily when setting up the acquisition scheme, the recorded micrographs need to be evaluated in terms of their particle content and the orientation of these particles. The result of the particle detection can be used to reconstruct a 3-D model of the target protein complex on-the-fly. Using this model, particle orientations can be determined that are still missing in the reconstruction. If the acquisition process records micrographs showing none or very few of particles in that orientation, the acquisition scheme can be modified to skip the adjacent area and continue recording at the next specimen area. Using this approach, less micrographs need to be recorded and a model with higher resolution can be produced in a shorter period of time.

The Titan Krios microscope is able to record over 2500 micrographs per day for single-particle investigations. This amount is equivalent to 100 GB of storage capacity, when micrographs are recorded with a binning factor of 2. If unbinned micrographs are used, the demand raises by a factor of four (400 GB per day). Post-processing of this data set will create even more demand for file storage, since during processing parts of the data sets are duplicated and normally stored separately. To date, it is possible to meet this demand merely by using file servers, however this storage method is still very expensive. Therefore, the post-processing of the data needs to be organized, sorting the data set continuously and archiving information, that is no longer needed for instant access, e.g., by using magnetic tapes. To survey the data and its post-processing history, and furthermore to allow for a better transparency, e.g., to others users or collaborators, a database system is absolutely mandatory, and additionally new ways of storing and handling data have to be developed in the near future.

With the availability of massively parallel programmable graphics processors in future computer systems and the availability of software development kits for these types of processors, even more complex image assessment algorithms will become possible. This will make assessment of the content and optical parameters of the acquired micrographs possible in real-time, increasing acquisition efficiency even further.

The combination of a high-end electron microscope such as the Titan Krios equipped with highly sensitive direct electron detection cameras with a versatile acquisition software, such as TOM^2, will make structural investigations in the field of cellular and structural biology more effective, enabling scientists to explore their specimen at higher resolution and will lead to new important discoveries.

5 Acknowledgments

I thank Wolfgang Baumeister and his department for providing an environment in which I could accomplish my studies and gain great insights into the field of electron microscopy and image processing.

Jürgen Plitzko and Stephan Nickell supervised my work and provided many useful tips and tricks regarding electron microscopy.

Florian Beck provided code and documentation for the Tecnai Scripting Interface.

Radosav Pantelic developed the original CTF and astigmatism fitting algorithms and helped implementing them in TOM^2 .

Anne-Marie Schoenegge and Beate Rockel provided me with samples of TPPII and performed the image processing of the acquired data.

Dennis Thomas helped me testing TOM^2 at the Tecnai F20 microscope and provided me with specimens of *E. coli* mini cells.

Carolin Fleischer tested and used TOM^2 in her *Spiroplasma citri* project, I thank her for giving me insight into the practical application of tomography.

Matthias Eibauer and Christian Hoffmann tested and used TOM^2 on the Titan Krios microscope to acquire high-magnification tilt series using a custom acquisition scheme.

Günther Pfeifer helped maintaining the microscopes and handled the specimens.

Elizabeth Villa tested TOM^2 for use in whole cell batch tomography.

I thank Jürgen Plitzko and Elizabeth Villa for proof-reading the thesis and giving valuable and helpful comments.

6 Abbreviations

CCD charge-coupled device 15

CCF cross-correlation function 45

CMOS complementary metal-oxide semiconductor 15

CTF contrast transfer function 14

DQE detective quantum efficiency 15

FEG field emission gun 25

FIB focused ion beam 111

FOV field of view 18

FSC Fourier shell correlation 90

GIF Gatan Imaging Filter 76

GUI graphical user interface 10

HAL hardware abstraction layer 24

LM light microscope 78

MCF mutual correlation function 46

MTF modulation transfer function 15

NA numerical aperture 79

PCA principal component analysis 47

PDF probability density function 84

PSD power spectral density 35

RANSAC random sample consensus 47

SDK software development kit 38

SIFT scale-invariant feature transform 46

SIRT simultaneous iterative reconstruction technique 16

SNR signal-to-noise ratio 13

SURF speeded up [sic] robust features 46

TEM transmission electron microscope 11

TPPII tripeptidyl peptidase II 94

Bibliography

[Adler *et al.*, 1967] H. I. Adler, W. D. Fisher, A. Cohen, and Alice A Hardigree. Miniature escherichia coli cells deficient in dna. *Proc Natl Acad Sci U S A*, 57(2):321–326, Feb 1967.

[Arfken, 1985] G. Arfken. *Mathematical Methods for Physicists*. Academic Press, Orlando, FL, 3rd edition, 1985.

[Aronova *et al.*, 2007] M. A. Aronova, Y. C. Kim, R. Harmon, A. A. Sousa, G. Zhang, and R. D. Leapman. Three-dimensional elemental mapping of phosphorus by quantitative electron spectroscopic tomography (QuEST). *J Struct Biol*, 160(1):35–48, Oct 2007.

[Arslan *et al.*, 2006] Ilke Arslan, Jenna R Tong, and Paul A Midgley. Reducing the missing wedge: High-resolution dual axis tomography of inorganic materials. *Ultramicroscopy*, 106(11-12):994–1000, 2006.

[Baumeister *et al.*, 1998] W. Baumeister, J. Walz, F. Zühl, and E. Seemüller. The proteasome: paradigm of a self-compartmentalizing protease. *Cell*, 92(3):367–380, Feb 1998.

[Baxter *et al.*, 2009] William T. Baxter, Robert A. Grassucci, Haixiao Gao, and Joachim Frank. Determination of signal-to-noise ratios and spectral snrs in cryo-em low-dose imaging of molecules. *Journal of Structural Biology*, 166(2):126–132, 2009.

[Bay *et al.*, 2008] Herbert Bay, Andreas Ess, Tinne Tuytelaars, and Luc Van Gool. SURF: Speeded Up Robust Features. *Computer Vision and Image Understanding (CVIU)*, 10(3):346–359, 2008.

[Beck *et al.*, 2004] Martin Beck, Friedrich Förster, Mary Ecke, Jürgen M Plitzko, Frauke Melchior, Günther Gerisch, Wolfgang Baumeister, and Ohad Medalia. Nuclear pore complex structure and dynamics revealed by cryoelectron tomography. *Science*, 306(5700):1387–1390, Nov 2004.

[Beckmann *et al.*, 1990] Norbert Beckmann, Hans-Peter Kriegel andRalf Schneider, and Bernhard Seeger. The R*-Tree: An Efficient and Robust Access Method for Points and Rectangles. In *SIGMOD Conference*, pages 322–331, 1990.

[Beer, 1852] A. Beer. Bestimmung der Absorption des rothen Lichts in farbigen Flüssigkeiten; von Beer in Bonn. *Annalen der Physik*, 86:78–87, 1852.

[Bové *et al.*, 2003] Joseph M Bové, Joël Renaudin, Colette Saillard, Xavier Foissac, and Monique Garnier. Spiroplasma citri, a plant pathogenic molligute: relationships with its two hosts, the plant and the leafhopper vector. *Annu Rev Phytopathol*, 41:483–500, 2003.

[Bové, 1993] J. M. Bové. Molecular features of mollicutes. *Clin Infect Dis*, 17 Suppl 1:S10–S31, Aug 1993.

[Bozzola and Russell, 1999] John J. Bozzola and Lonnie Dee Russell. *Electron microscopy: principles and techniques for biologists*. Jones and Bartlett Publishers, Inc, 2nd edition, 1999.

[Braunfeld *et al.*, 1994] M. B. Braunfeld, A. J. Koster, J. W. Sedat, and D. A. Agard. Cryo automated electron tomography: towards high-resolution reconstructions of plastic-embedded structures. *J Microsc*, 174(Pt 2):75–84, May 1994.

[Canny, 1986] John Canny. A Computational Approach to Edge Detection. *IEEE Transactions on Pattern Analysis and Machine Intelligence*, PAMI-8(6):679–698, 1986.

[Carazo *et al.*, 1989] J. M. Carazo, T. Wagenknecht, and J. Frank. Variations of the three-dimensional structure of the Escherichia coli ribosome in the range of overlap views. an application of the methods of multicone and local single-cone three-dimensional reconstruction. *Biophys J*, 55(3):465–477, Mar 1989.

[Carragher *et al.*, 2000] B. Carragher, N. Kisseberth, D. Kriegman, R. A. Milligan, C. S. Potter, J. Pulokas, and A. Reilein. Leginon: an automated system for acquisition of images from vitreous ice specimens. *J Struct Biol*, 132(1):33–45, Oct 2000.

[Cheng *et al.*, 2006] Anchi Cheng, Denis Fellmann, James Pulokas, Clinton S Potter, and Bridget Carragher. Does contamination buildup limit throughput for automated cryoEM? *J Struct Biol*, 154(3):303–311, Jun 2006.

[Cheng *et al.*, 2007] Anchi Cheng, Albert Leung, Denis Fellmann, Joel Quispe, Christian Suloway, James Pulokas, Priyanka D Abeyrathne, Joseph S Lam, Bridget Carragher, and Clinton S Potter. Towards automated screening of two-dimensional crystals. *J Struct Biol*, 160(3):324–331, Dec 2007.

[Chiu *et al.*, 1986] W. Chiu, T. W. Jeng, L. L. Degn, and B. V. Prasad. Potential for high-resolution electron crystallography at intermediate high voltage. *Ann N Y Acad Sci*, 483:149–156, 1986.

[Chiu, 1986] W. Chiu. Electron microscopy of frozen, hydrated biological specimens. *Annu Rev Biophys Biophys Chem*, 15:237–257, 1986.

[Cosslett, 1969] V.E. Cosslett. Energy loss and chromatic aberration in electron microscopy. *Zeitschrift für angewandte Physik*, 27:138–141, 1969.

[Crowther *et al.*, 1970] R. A. Crowther, L. A. Amos, J. T. Finch, D. J. De Rosier, and A. Klug. Three dimensional reconstructions of spherical viruses by fourier synthesis

from electron micrographs. *Nature*, 226(5244):421–425, May 1970.

[Dahmen, 2007] U Dahmen. A status report on the team project. *Microscopy and Microanalysis*, 13(Supplement S02):1150–1151, 2007.

[Dierksen *et al.*, 1992] K. Dierksen, D. Typke, R. Hegerl, A.J. Koster, and W. Baumeister. Towards automatic electron tomography. *Ultramicroscopy*, 40(1):71–87, 1992.

[Dubochet *et al.*, 1988] J. Dubochet, M. Adrian, J. J. Chang, J. C. Homo, J. Lepault, A. W. McDowall, and P. Schultz. Cryo-electron microscopy of vitrified specimens. *Q Rev Biophys*, 21(2):129–228, May 1988.

[Fan *et al.*, 1995] G. Y. Fan, S. J. Young, P. Miller, and M. H. Ellisman. Conditions for electron tomographic data acquisition. *J Electron Microsc (Tokyo)*, 44(1):15–21, Feb 1995.

[Faruqi and Henderson, 2007] A. R. Faruqi and R. Henderson. Electronic detectors for electron microscopy. *Curr Opin Struct Biol*, 17(5):549–555, Oct 2007.

[Feja and Aebi, 1999] B. Feja and U. Aebi. Determination of the inelastic mean free path of electrons in vitrified ice layers for on-line thickness measurements by zero-loss imaging. *J Microsc*, 193(1):15–19, Jan 1999.

[Fischer *et al.*, 2004] Hannes Fischer, Igor Polikarpov, and Aldo F Craievich. Average protein density is a molecular-weight-dependent function. *Protein Sci*, 13(10):2825–2828, Oct 2004.

[Fischler and Bolles, 1981] Martin A. Fischler and Robert C. Bolles. Random Sample Consensus: A Paradigm for Model Fitting with Applications to Image Analysis and Automated Cartography. *Comm. Of the ACM*, 24:381–395, 1981.

[Fleischer, 2010] Carolin Fleischer. *Identification and Visualization of Macromolecules in intact cells by Cryo-electron Tomography.* PhD thesis, TU München, 2010.

[Fletcher *et al.*, 1998] J. Fletcher, A. Wayadande, U. Melcher, and F. Ye. The phytopathogenic mollicute-insect vector interface: a closer look. *Phytopathology*, 88(12):1351–1358, Dec 1998.

[Frangakis *et al.*, 2002] Achilleas S Frangakis, Jochen Böhm, Friedrich Förster, Stephan Nickell, Daniela Nicastro, Dieter Typke, Reiner Hegerl, and Wolfgang Baumeister. Identification of macromolecular complexes in cryoelectron tomograms of phantom cells. *Proc Natl Acad Sci U S A*, 99(22):14153–14158, Oct 2002.

[Frank *et al.*, 1986] J. Frank, M. Radermacher, T. Wagenknecht, and A. Verschoor. A new method for three-dimensional reconstruction of single macromolecules using low-dose electron micrographs. *Ann N Y Acad Sci*, 483:77–87, 1986.

[Frank *et al.*, 1996] J. Frank, M. Radermacher, P. Penczek, J. Zhu, Y. Li, M. Ladjadj, and A. Leith. SPIDER and WEB: processing and visualization of images in 3D electron microscopy and related fields. *J Struct Biol*, 116(1):190–199, 1996.

[Frank, 1992] Joachim Frank. *Electron Tomography*. Plenum Press, New York, 1992.

[Fukushima *et al.*, 1974] K. Fukushima, H. Kawakatsu, and A. Fukami. Fresnel fringes in electron microscope images. *Journal of Physics D: Applied Physics*, 7(2):257–266, 1974.

[Gander *et al.*, 1994] Walter Gander, Gene H. Golub, and Rolf Strebel. Least-squares fitting of circles and ellipses. *BIT Numerical Mathematics*, 34:558–578, July 1994.

[Gilbert, 1972] Peter Gilbert. Iterative methods for the three-dimensional reconstruction of an object from projections. *J. theor. Biol.*, 36:105–117, 1972.

[Glaeser and Downing, 1992] R.M Glaeser and K.H. Downing. Assessment of resolution in biological electron crystallography. *Ultramicroscopy*, 47:256–65, 1992.

[Glaeser and Hobbs, 1975] R. M. Glaeser and L. W. Hobbs. Radiation damage in stained catalase at low temperature. *J Microsc*, 103(2):209–214, Mar 1975.

[Glaeser and Taylor, 1978] R. M. Glaeser and K. A. Taylor. Radiation damage relative to transmission electron microscopy of biological specimens at low temperature: a review. *J Microsc*, 112(1):127–138, Jan 1978.

[Goddard *et al.*, 2007] Thomas D Goddard, Conrad C Huang, and Thomas E Ferrin. Visualizing density maps with ucsf chimera. *J Struct Biol*, 157(1):281–287, Jan 2007.

[Goldsmith and Miller, 2009] Cynthia S. Goldsmith and Sara E. Miller. Modern uses of electron microscopy for detection of viruses. *Clin Microbiol Rev*, 22(4):552–563, Oct 2009.

[Goshtasby, 1986] Ardeshir Goshtasby. Piecewise linear mapping functions for image registration. *Pattern Recognition*, 19:459–466, 1986.

[Goshtasby, 1988] Ardeshir Goshtasby. Image registration by local approximation methods. *Image and Vision Computing*, 6:255–261, 1988.

[Grimm *et al.*, 1996a] R. Grimm, A. J. Koster, U. Ziese, D. Typke, and W. Baumeister. Zero-loss energy filtering under low-dose conditions using a post-column energy filter. *Journal of Microscopy*, 183:60–68, 1996.

[Grimm *et al.*, 1996b] R. Grimm, D. Typke, M. Bärmann, and W. Baumeister. Determination of the inelastic mean free path in ice by examination of tilted vesicles and automated most probable loss imaging. *Ultramicroscopy*, 63(3-4):169–179, Jul 1996.

[Groll *et al.*, 1997] M. Groll, L. Ditzel, J. Löwe, D. Stock, M. Bochtler, H. D. Bartunik, and R. Huber. Structure of 20S proteasome from yeast at 2.4 A resolution. *Nature*, 386(6624):463–471, Apr 1997.

[Grünewald *et al.*, 2003] Kay Grünewald, Ohad Medalia, Ariane Gross, Alasdair C Steven, and Wolfgang Baumeister. Prospects of electron cryotomography to visualize macromolecular complexes inside cellular compartments: implications of crowding.

Biophys Chem, 100(1-3):577–591, 2003.

[Gruska *et al.*, 2008] Manuela Gruska, Ohad Medalia, Wolfgang Baumeister, and Andrew Leis. Electron tomography of vitreous sections from cultured mammalian cells. *J Struct Biol*, 161(3):384–392, Mar 2008.

[Guckenberger, 1982] R. Guckenberger. Determination of a common origin in the micrographs of tilt series in three-dimensional electron microscopy. *Ultramicroscopy*, 9(1-2):167–173, 1982.

[Guttman, 1984] Toni Guttman. R-Trees: A Dynamic Index Structure for Spatial Searching. In *ACM SIGMOD International Conference on Management of Data*, pages 47–57, 1984.

[Han *et al.*, 1997] K. F. Han, J. W. Sedat, and D. A. Agard. Practical image restoration of thick biological specimens using multiple focus levels in transmission electron microscopy. *J Struct Biol*, 120(3):237–244, Dec 1997.

[Hart, 1968] R. G. Hart. Electron microscopy of unstained biological material: the polytropic montage. *Science*, 159(3822):1464–1467, Mar 1968.

[Hartley, 1928] R. V. L. Hartley. Transmission of Information. *Bell System Technical Journal*, 1928.

[Hegerl and Hoppe, 1976] R. Hegerl and W. Hoppe. Influence of electron-noise on three-dimensional image reconstruction. *Z. Naturforsch.*, 31a:1717–1721, 1976.

[Henderson *et al.*, 1990] R. Henderson, J. M. Baldwin, T. A. Ceska, F. Zemlin, E. Beckmann, and K. H. Downing. Model for the structure of bacteriorhodopsin based on high-resolution electron cryo-microscopy. *J Mol Biol*, 213(4):899–929, Jun 1990.

[Hoppe, 1969] W. Hoppe. Das Endlichkeitspostulat und das Interpolationstheorem der dreidimensionalen elektronenmikroskopischen Analyse aperiodischer Strukturen. *Optik*, 29:617–621, 1969.

[Iancu *et al.*, 2005] Cristina V Iancu, Elizabeth R Wright, Jordan Benjamin, William F Tivol, D. Prabha Dias, Gavin E Murphy, Robert C Morrison, J. Bernard Heymann, and Grant J Jensen. A "flip-flop" rotation stage for routine dual-axis electron cryotomography. *J Struct Biol*, 151(3):288–297, Sep 2005.

[Iancu *et al.*, 2006] Cristina V Iancu, William F Tivol, Jordan B Schooler, D. Prabha Dias, Gregory P Henderson, Gavin E Murphy, Elizabeth R Wright, Zhuo Li, Zhiheng Yu, Ariane Briegel, Lu Gan, Yongning He, and Grant J Jensen. Electron cryotomography sample preparation using the Vitrobot. *Nat Protoc*, 1(6):2813–2819, 2006.

[Isaacson *et al.*, 1977] M. Isaacson, J. M. Langmore, and H. Rose. Determination of nonlocalization of inelastic scattering of electrons by electron microscopy. *Optik*, 41(1):92–96, 1977.

[Ishizuka, 1993] Kazuo Ishizuka. Analysis of electron image detection efficiency of slow-

scan CCD cameras. *Ultramicroscopy*, 52(1):7–20, 1993.

[Jaffé *et al.*, 1986] A. Jaffé, R. D'Ari, and V. Norris. SOS-independent coupling between DNA replication and cell division in Escherichia coli. *J Bacteriol*, 165(1):66–71, Jan 1986.

[Jaffé *et al.*, 1988] A. Jaffé, R. D'Ari, and S. Hiraga. Minicell-forming mutants of Escherichia coli: production of minicells and anucleate rods. *J Bacteriol*, 170(7):3094–3101, Jul 1988.

[Janesick, 2001] J.R. Janesick. *Scientific Charge-Coupled Devices*. SPIE Press, Bellingham, WA, 2001.

[Jonic and Vénien-Bryan, 2009] Slavica Jonic and Catherine Vénien-Bryan. Protein structure determination by electron cryo-microscopy. *Curr Opin Pharmacol*, 9(5):636–642, Oct 2009.

[Ke and Sukthankar, 2004] Y. Ke and R. Sukthankar. PCA-SIFT: A More Distinctive Representation for Local Image Descriptors. In *Proceedings of Computer Vision and Pattern Recognition*, 2004.

[Kisseberth *et al.*, 1997] Kisseberth, Whittaker, Weber, Potter, and Carragher. emScope: A Tool Kit for Control and Automation of a Remote Electron Microscope. *J Struct Biol*, 120(3):309–319, Dec 1997.

[Konevega *et al.*, 2007] Andrey L Konevega, Niels Fischer, Yuri P Semenkov, Holger Stark, Wolfgang Wintermeyer, and Marina V Rodnina. Spontaneous reverse movement of mRNA-bound tRNA through the ribosome. *Nat Struct Mol Biol*, 14(4):318–324, Apr 2007.

[Koster and de Ruijter, 1992] A.J. Koster and W.J. de Ruijter. Practical autoalignment of transmission electron microscopes. *Ultramicroscopy*, 40:89–107, 1992.

[Koster *et al.*, 1989] A.J. Koster, W.J. de Ruijter, A. van der Bos, and K.D. van der Mast. Autotuning of a TEM using minimal electron dose. *Ultramicroscopy*, 27(3):251–272, 1989.

[Koster *et al.*, 1992] A. J. Koster, H. Chen, J. W. Sedat, and D. A. Agard. Automated microscopy for electron tomography. *Ultramicroscopy*, 46(1-4):207–227, Oct 1992.

[Krivanek and Mooney, 1993] O.L. Krivanek and P.E. Mooney. Applications of slow-scan ccd cameras in transmission electron microscopy. *Ultramicroscopy*, 49(1-4):95–108, 1993.

[Krivanek *et al.*, 1995] O. L. Krivanek, S. L. Friedman, A. J. Gubbens, and B. Kraus. An imaging filter for biological applications. *Ultramicroscopy*, 59(1-4):267–282, 1995. Proceedings of the 2nd international workshop on Electron Energy Loss Spectroscopy and Imaging.

[Lambert, 1760] J. H. Lambert. Photometria, sive de mensura et gradibus luminis col-

orum et umbrae. *Sumptibus Vidae Eberhardi Klett*, 1760.

[Lander *et al.*, 2009] Gabriel C Lander, Scott M Stagg, Neil R Voss, Anchi Cheng, Denis Fellmann, James Pulokas, Craig Yoshioka, Christopher Irving, Anke Mulder, Pick-Wei Lau, Dmitry Lyumkis, Clinton S Potter, and Bridget Carragher. Appion: an integrated, database-driven pipeline to facilitate EM image processing. *J Struct Biol*, 166(1):95–102, Apr 2009.

[Langmore and Smith, 1992] John P. Langmore and Michael F. Smith. Quantitative energy-filtered electron microscopy of biological molecules in ice. *Ultramicroscopy*, 46(1-4):349–373, 1992.

[Leapman *et al.*, 2004] R. D. Leapman, E. Kocsis, G. Zhang, T. L. Talbot, and P. Laquerriere. Three-dimensional distributions of elements in biological samples by energy-filtered electron tomography. *Ultramicroscopy*, 100(1-2):115–125, Jul 2004.

[Leis *et al.*, 2009] Andrew Leis, Beate Rockel, Lars Andrees, and Wolfgang Baumeister. Visualizing cells at the nanoscale. *Trends Biochem Sci*, 34(2):60–70, Feb 2009.

[Lowe, 2004] David G Lowe. Distinctive image features from scale-invariant keypoints. *International Journal of Computer Vision*, 60(2):91–110, 2004.

[Lucic *et al.*, 2005] Vladan Lucic, Friedrich Förster, and Wolfgang Baumeister. Structural studies by electron tomography: from cells to molecules. *Annu Rev Biochem*, 74:833–865, 2005.

[Ludtke *et al.*, 1999] S. J. Ludtke, P. R. Baldwin, and W. Chiu. Eman: semiautomated software for high-resolution single-particle reconstructions. *J Struct Biol*, 128(1):82–97, Dec 1999.

[Löwe *et al.*, 1995] J. Löwe, D. Stock, B. Jap, P. Zwickl, W. Baumeister, and R. Huber. Crystal structure of the 20s proteasome from the archaeon t. acidophilum at 3.4 a resolution. *Science*, 268(5210):533–539, Apr 1995.

[Mallick *et al.*, 2005] Satya P Mallick, Bridget Carragher, Clinton S Potter, and David J Kriegman. ACE: automated CTF estimation. *Ultramicroscopy*, 104(1):8–29, Aug 2005.

[Mastronarde, 1997] D. N. Mastronarde. Dual-axis tomography: an approach with alignment methods that preserve resolution. *J Struct Biol*, 120(3):343–352, Dec 1997.

[Mastronarde, 2005] David N Mastronarde. Automated electron microscope tomography using robust prediction of specimen movements. *J Struct Biol*, 152(1):36–51, Oct 2005.

[McEwen and Marko, 1999] B. F. McEwen and M. Marko. Three-dimensional transmission electron microscopy and its application to mitosis research. *Methods Cell Biol*, 61:81–111, 1999.

[McEwen and Marko, 2001] B. F. McEwen and M. Marko. The emergence of electron tomography as an important tool for investigating cellular ultrastructure. *J Histochem Cytochem*, 49(5):553–564, May 2001.

[McEwen *et al.*, 1995] B. F. McEwen, K. H. Downing, and R. M. Glaeser. The relevance of dose-fractionation in tomography of radiation-sensitive specimens. *Ultramicroscopy*, 60(3):357–373, Oct 1995.

[McMullan *et al.*, 2009a] G. McMullan, S. Chen, R. Henderson, and A. R. Faruqi. Detective quantum efficiency of electron area detectors in electron microscopy. *Ultramicroscopy*, 109(9):1126–1143, Aug 2009.

[McMullan *et al.*, 2009b] G. McMullan, A. R. Faruqi, R. Henderson, N. Guerrini, R. Turchetta, A. Jacobs, and G. van Hoften. Experimental observation of the improvement in MTF from backthinning a CMOS direct electron detector. *Ultramicroscopy*, 109(9):1144–1147, Aug 2009.

[Medalia *et al.*, 2002] Ohad Medalia, Igor Weber, Achilleas S Frangakis, Daniela Nicastro, Gunther Gerisch, and Wolfgang Baumeister. Macromolecular architecture in eukaryotic cells visualized by cryoelectron tomography. *Science*, 298(5596):1209–1213, Nov 2002.

[Morel and G.Yu, 2009] J.M. Morel and G.Yu. ASIFT: A New Framework for Fully Affine Invariant Image Comparison. *SIAM Journal on Imaging Sciences*, 2(2):438–469, 2009.

[Nagayama and Danev, 2009] Kuniaki Nagayama and Radostin Danev. Phase-plate electron microscopy: a novel imaging tool to reveal close-to-life nano-structures. *Biophysical Reviews*, 1(1):37–42, 2009.

[Nickell *et al.*, 2005] Stephan Nickell, Friedrich Förster, Alexandros Linaroudis, William Del Net, Florian Beck, Reiner Hegerl, Wolfgang Baumeister, and Jürgen M Plitzko. TOM software toolbox: acquisition and analysis for electron tomography. *J Struct Biol*, 149(3):227–234, Mar 2005.

[Nickell *et al.*, 2006] Stephan Nickell, Christine Kofler, Andrew P Leis, and Wolfgang Baumeister. A visual approach to proteomics. *Nat Rev Mol Cell Biol*, 7(3):225–230, Mar 2006.

[Nickell *et al.*, 2007a] Stephan Nickell, Florian Beck, Andreas Korinek, Oana Mihalache, Wolfgang Baumeister, and Jürgen M Plitzko. Automated cryoelectron microscopy of "single particles" applied to the 26S proteasome. *FEBS Lett*, 581(15):2751–2756, Jun 2007.

[Nickell *et al.*, 2007b] Stephan Nickell, Oana Mihalache, Florian Beck, Reiner Hegerl, Andreas Korinek, and Wolfgang Baumeister. Structural analysis of the 26S proteasome by cryoelectron tomography. *Biochem Biophys Res Commun*, 353(1):115–120, Feb 2007.

[Nickell *et al.*, 2009] Stephan Nickell, Florian Beck, Sjors H W Scheres, Andreas Korinek, Friedrich Förster, Keren Lasker, Oana Mihalache, Na Sun, István Nagy, Andrej Sali, Jürgen M Plitzko, Jose-Maria Carazo, Matthias Mann, and Wolfgang Baumeis-

ter. Insights into the molecular architecture of the 26S proteasome. *Proc Natl Acad Sci U S A*, 106(29):11943–11947, Jul 2009.

[Oostergetel *et al.*, 1998] G.T. Oostergetel, W. Keegstra, and A.Brisson. Automation of specimen selection and data acquisition for protein electron crystallography. *Ultramicroscopy*, 74:47–59, 1998.

[Ortiz *et al.*, 2006] Julio O Ortiz, Friedrich Förster, Julia Kürner, Alexandros A Linaroudis, and Wolfgang Baumeister. Mapping 70S ribosomes in intact cells by cryoelectron tomography and pattern recognition. *J Struct Biol*, 156(2):334–341, Nov 2006.

[Palade, 1952] G. E. Palade. A Study of Fixation for Electron Microscopy. *Journal of Expe- rimental Medicine*, 95(3):285–307, 1952.

[Pettersen *et al.*, 2004] Eric F Pettersen, Thomas D Goddard, Conrad C Huang, Gregory S Couch, Daniel M Greenblatt, Elaine C Meng, and Thomas E Ferrin. Ucsf chimera–a visualization system for exploratory research and analysis. *J Comput Chem*, 25(13):1605–1612, Oct 2004.

[Plitzko *et al.*, 2009] Jürgen M Plitzko, Alexander Rigort, and Andrew Leis. Correlative cryo-light microscopy and cryo-electron tomography: from cellular territories to molecular landscapes. *Curr Opin Biotechnol*, 20(1):83–89, Feb 2009.

[Radermacher, 1988] M. Radermacher. Three-Dimensional Reconstruction of Single Particles From Random and Nonrandom Tilt Series. *Journal of Electron Microscopy Technique*, 9:359–394, 1988.

[Radon, 1917] J. Radon. On the Determination of Functions From Their Integral Values Along Certain Manifolds. *Berichte der Sächsischen Akademie der Wissenschaft*, 69:262–277, 1917.

[Rath *et al.*, 1997] B. K. Rath, M. Marko, M. Radermacher, and J. Frank. Low-dose automated electron tomography: a recent implementation. *J Struct Biol*, 120(3):210–218, Dec 1997.

[Reimer, 1984] L. Reimer. *Transmission Electron Microscopy*, volume 36. Springer-Verlag, 1984.

[Richardson *et al.*, 1960] K. C. Richardson, L. Jarett, and E. H. Finke. Embedding in epoxy resins for ultrathin sectioning in electron microscopy. *Stain Technol*, 35:313–323, Nov 1960.

[Rigort *et al.*, 2010] Alexander Rigort, Felix J B Bäuerlein, Andrew Leis, Manuela Gruska, Christian Hoffmann, Tim Laugks, Ulrike Böhm, Matthias Eibauer, Helmut Gnaegi, Wolfgang Baumeister, and Jürgen M Plitzko. Micromachining tools and correlative approaches for cellular cryo-electron tomography. *J Struct Biol*, Feb 2010.

[Robinson *et al.*, 2007] Carol V Robinson, Andrej Sali, and Wolfgang Baumeister. The

molecular sociology of the cell. *Nature*, 450(7172):973–982, Dec 2007.

[Rockel *et al.*, 2005] Beate Rockel, Jürgen Peters, Shirley A Müller, Gönül Seyit, Philippe Ringler, Reiner Hegerl, Robert M Glaeser, and Wolfgang Baumeister. Molecular architecture and assembly mechanism of Drosophila tripeptidyl peptidase II. *Proc Natl Acad Sci U S A*, 102(29):10135–10140, Jul 2005.

[Rolando *et al.*, 2007] A. Rolando, M.C. Romanini, M.T. Mugnaini, A. Bozzo, I. Pastorino, and C.A. Sonez. Ultrastructural study of spermatogenesis in eisenia foetida. *Int. J. Morphol.*, 25(2):277–284, Jun 2007.

[Rose and Plies, 1974] H. Rose and E. Plies. Entwurf eines fehlerarmen magnetischen Energie-Analysators. *Optik*, 40:336–341, 1974.

[Rose, 1948] A. Rose. *Television Camera Tubes and the Problem of Vision.* Academic Press, New York, 1948.

[Ruijter, 1995] W. J. Ruijter. Imaging properties and applications of slow-scan charge coupled device cameras suitable for electron microscopy. *Micron*, 26(3):247–275, 1995.

[Ruprecht and Nield, 2001] J. Ruprecht and J. Nield. Determining the structure of biological macromolecules by transmission electron microscopy, single particle analysis and 3D reconstruction. *Prog Biophys Mol Biol*, 75(3):121–164, 2001.

[Ruska, 1987] E. Ruska. The development of the electronmicroscope and electron microscopy. nobel lecture 1986. *Rev. Modern Phys.*, 59(3):627–638, 1987.

[Saad *et al.*, 2001] A. Saad, S.J. Ludke, J. Jakana, F.J. Rixon, H. Tsuruta, and W. Chiu. Fourier amplitude decay of electron cryomicroscopic images of single particles and effects on structure determination. *J. Struct. Biol.*, 133(1):32–42, 2001.

[Saglio *et al.*, 1971] P. Saglio, D. Laflche, C. Bonissol, and J. M. Bov. Culture in vitro des mycoplasmes associs au stubborn des agrumes et leur observation au microscope lectronique. *C R Acad Sci Paris*, 272:1387–1390, 1971.

[Saglio *et al.*, 1973] P. Saglio, M. Lhospital, D. Laflche, G. Dupont, J. M. Bov, J. G. Tully, and E. A. Freundt. Spiroplasma citri gen. and sp. n.: a mycoplasma-like organism associated with 'stubborn' disease of citrus. *Int J Syst Bacteriol*, 23:191–204, 1973.

[Sander *et al.*, 2003] B. Sander, M. M. Golas, and H. Stark. Automatic CTF correction for single particles based upon multivariate statistical analysis of individual power spectra. *J Struct Biol*, 142(3):392–401, Jun 2003.

[Sartori *et al.*, 2007] Anna Sartori, Rudolf Gatz, Florian Beck, Alexander Rigort, Wolfgang Baumeister, and Juergen M Plitzko. Correlative microscopy: bridging the gap between fluorescence light microscopy and cryo-electron tomography. *J Struct Biol*, 160(2):135–145, Nov 2007.

[Saxton and Baumeister, 1982] W. O. Saxton and W. Baumeister. The correlation av-

eraging of a regularly arranged bacterial cell envelope protein. *J Microsc*, 127(Pt 2):127–138, Aug 1982.

[Scheres *et al.*, 2007] Sjors H W Scheres, Haixiao Gao, Mikel Valle, Gabor T Herman, Paul P B Eggermont, Joachim Frank, and Jose-Maria Carazo. Disentangling conformational states of macromolecules in 3D-EM through likelihood optimization. *Nat Methods*, 4(1):27–29, Jan 2007.

[Scheres *et al.*, 2008] Sjors H W Scheres, Rafael Núñez-Ramírez, Carlos O S Sorzano, José María Carazo, and Roberto Marabini. Image processing for electron microscopy single-particle analysis using XMIPP. *Nat Protoc*, 3(6):977–990, 2008.

[Scherzer, 1949] O. Scherzer. The theoretical resolution limit of the electron microscope. *J. Applied Physics*, 20:20–29, 1949.

[Schiske, 1968] P Schiske. In *Proceedings of the Fourth Regional Congress on Electron Microscopy*, volume 1, pages 145–146, 1968.

[Schiske, 2002] P. Schiske. Image reconstruction by means of focus series. *J Microsc*, 207(Pt 2):154, Aug 2002.

[Schröder *et al.*, 1990] R. R. Schröder, W. Hofmann, and J.-F. Menetret. Zero-loss energy filtering as improved imaging mode in cryoelectronmicroscopy of frozen-hydrated specimens. *J. Struct. Biol.*, 105:28–34, 1990.

[Seemüller *et al.*, 1995] E. Seemüller, A. Lupas, D. Stock, J. Löwe, R. Huber, and W. Baumeister. Proteasome from thermoplasma acidophilum: a threonine protease. *Science*, 268(5210):579–582, Apr 1995.

[Shannon, 1949] C. E. Shannon. Communication in the presence of noise. *Proc. Institute of Radio Engineers*, 37(1):10–21, 1949.

[Sherman *et al.*, 1996] Michael B. Sherman, Jacob Brink, and Wah Chiu. Performance of a slow-scan CCD camera for macromolecular imaging in a 400 kV electron cryomicroscope. *Micron*, 27(2):129–139, 1996.

[Shi *et al.*, 2008] Jian Shi, Dewight R Williams, and Phoebe L Stewart. A Script-Assisted Microscopy (SAM) package to improve data acquisition rates on FEI Tecnai electron microscopes equipped with Gatan CCD cameras. *J Struct Biol*, 164(1):166–169, Oct 2008.

[Stagg *et al.*, 2006] Scott M Stagg, Gabriel C Lander, James Pulokas, Denis Fellmann, Anchi Cheng, Joel D Quispe, Satya P Mallick, Radomir M Avila, Bridget Carragher, and Clinton S Potter. Automated cryoEM data acquisition and analysis of 284742 particles of GroEL. *J Struct Biol*, 155(3):470–481, Sep 2006.

[Steven and Belnap, 2005] Alasdair Steven and David Belnap. Electron microscopy and image processing: an essential tool for structural analysis of macromolecules. *Curr Protoc Protein Sci*, Chapter 17:Unit 17.2, Dec 2005.

[Studer *et al.*, 1989] D. Studer, M. Michel, and M. Müller. High pressure freezing comes of age. *Scanning Microsc Suppl*, 3:253–68; discussion 268–9, 1989.

[Suloway *et al.*, 2005] Christian Suloway, James Pulokas, Denis Fellmann, Anchi Cheng, Francisco Guerra, Joel Quispe, Scott Stagg, Clinton S Potter, and Bridget Carragher. Automated molecular microscopy: the new Leginon system. *J Struct Biol*, 151(1):41–60, Jul 2005.

[Suloway *et al.*, 2009] Christian Suloway, Jian Shi, Anchi Cheng, James Pulokas, Bridget Carragher, Clinton S Potter, Shawn Q Zheng, David A Agard, and Grant J Jensen. Fully automated, sequential tilt-series acquisition with Leginon. *J Struct Biol*, 167(1):11–18, Jul 2009.

[Thon, 1971] F. Thon. *Phase contrast electron microscopy.* Academic Press, N.Y., 1971.

[Tong *et al.*, 2006] Jenna Tong, Ilke Arslan, and Paul Midgley. A novel dual-axis iterative algorithm for electron tomography. *J Struct Biol*, 153(1):55–63, Jan 2006.

[Tsuno, 2004] K. Tsuno. Evaluation of in-column energy filters for analytical electron microscopes. *Nuclear Instruments and Methods in Physics Research Section A: Accelerators, Spectrometers, Detectors and Associated Equipment*, 519(1-2):286–296, 2004. Proceedings of the Sixth International Conference on Charged Particle Optics.

[Tully, 1992] J. G. Tully. *Enceclopedia of Microbiology.* Academic Press, New York, 1992.

[Unno *et al.*, 2002] Masaki Unno, Tsunehiro Mizushima, Yukio Morimoto, Yoshikazu Tomisugi, Keiji Tanaka, Noritake Yasuoka, and Tomitake Tsukihara. The structure of the mammalian 20S proteasome at 2.75 A resolution. *Structure*, 10(5):609–618, May 2002.

[van Heel *et al.*, 1992] Marin van Heel, Michael Schatz, and Elena Orlova. Correlation funtions revisited. *Ultramicroscopy*, 46:307–316, 1992.

[van Heel *et al.*, 2000] M. van Heel, B. Gowen, R. Matadeen, E. V. Orlova, R. Finn, T. Pape, D. Cohen, H. Stark, R. Schmidt, M. Schatz, and A. Patwardhan. Single-particle electron cryo-microscopy: towards atomic resolution. *Q Rev Biophys*, 33(4):307–369, Nov 2000.

[Vedaldi and Fulkerson, 2008] A. Vedaldi and B. Fulkerson. VLFeat: An open and portable library of computer vision algorithms. `http://www.vlfeat.org/`, 2008.

[Voges *et al.*, 1999] D. Voges, P. Zwickl, and W. Baumeister. The 26S proteasome: a molecular machine designed for controlled proteolysis. *Annu Rev Biochem*, 68:1015–1068, 1999.

[Wade, 1992] R. H. Wade. A brief look at imaging and contrast transfer. *Ultramicroscopy*, 46:145–156, 1992.

[Weickenmeier *et al.*, 1995] A.L. Weickenmeier, W. Nuechter, and J. Mayer. Quantita-

tive characterization of point spread function and detection quantum efficiency for a YAG scintillator slow-scan CCD camera. *Optik*, 99(4):147–154, 1995.

[Weisburg *et al.*, 1989] W. G. Weisburg, J. G. Tully, D. L. Rose, J. P. Petzel, H. Oyaizu, D. Yang, L. Mandelco, J. Sechrest, T. G. Lawrence, and J. Van Etten. A phylogenetic analysis of the mycoplasmas: basis for their classification. *J Bacteriol*, 171(12):6455–6467, Dec 1989.

[Yoshioka *et al.*, 2007] Craig Yoshioka, James Pulokas, Denis Fellmann, Clinton S Potter, Ronald A Milligan, and Bridget Carragher. Automation of random conical tilt and orthogonal tilt data collection using feature-based correlation. *J Struct Biol*, 159(3):335–346, Sep 2007.

[Zhang *et al.*, 2001] P. Zhang, A. Beatty, J. L. Milne, and S. Subramaniam. Automated data collection with a Tecnai 12 electron microscope: applications for molecular imaging by cryomicroscopy. *J Struct Biol*, 135(3):251–261, Sep 2001.

[Zhang *et al.*, 2009] Junjie Zhang, Natsuko Nakamura, Yuko Shimizu, Nathan Liang, Xiangan Liu, Joanita Jakana, Michael P Marsh, Christopher R Booth, Takao Shinkawa, Munetaka Nakata, and Wah Chiu. JADAS: a customizable automated data acquisition system and its application to ice-embedded single particles. *J Struct Biol*, 165(1):1–9, Jan 2009.

[Zhang, 1998] Hong Zhang. What limits the application of TEM in the semiconductor industry? *Thin Solid Films*, 320(1):77–85, 1998.

[Zheng *et al.*, 2007a] Shawn Q Zheng, Bettina Keszthelyi, Eric Branlund, John M Lyle, Michael B Braunfeld, John W Sedat, and David A Agard. UCSF tomography: an integrated software suite for real-time electron microscopic tomographic data collection, alignment, and reconstruction. *J Struct Biol*, 157(1):138–147, Jan 2007.

[Zheng *et al.*, 2007b] Shawn Q Zheng, Justin M Kollman, Michael B Braunfeld, John W Sedat, and David A Agard. Automated acquisition of electron microscopic random conical tilt sets. *J Struct Biol*, 157(1):148–155, Jan 2007.

[Zhou, 2008] Z. Hong Zhou. Towards atomic resolution structural determination by single-particle cryo-electron microscopy. *Curr Opin Struct Biol*, 18(2):218–228, Apr 2008.

[Ziese *et al.*, 2003] U. Ziese, W. J C Geerts, T. P. Van Der Krift, A. J. Verkleij, and A. J. Koster. Correction of autofocusing errors due to specimen tilt for automated electron tomography. *J Microsc*, 211(Pt 2):179–185, Aug 2003.